Site BA4[1]

Kelemen, P.B., Matter, J.M., Teagle, D.A.H., Coggon, J.A., and the Oman Drilling Project Science Team[2]

Keywords: Oman Drilling Project, Oman DP, Site BA4, Hole BA4A, Wadi Lawayni, Samail ophiolite, serpentinized dunite, mantle, hydrology, chemosynthetic biosphere

Chapter contents

Introduction

Site BA4

Site BA4 (22.88501°N, 58.69505°E) is situated in the northern end of Wadi Lawayni (Fig. F2 in the **Introduction to Science Theme 3** chapter) and hosted in partially serpentinized dunite of the mantle section of the Samail ophiolite (Fig. F1 in the **Introduction to Science Theme 1A** chapter) at the foot of a small dunite hill (Fig. F1). A 300 m diamond cored hole was sited here as a far-field site of the Wadi Lawayni multiborehole test site. The resulting data will address active weathering (hydration, oxidation, and carbonation) of mainly serpentinized dunite and will explore the subsurface hydrology and chemosynthetic biosphere fostered by weathering of mantle peridotite. In addition, the results from the core analysis will address mantle melt transport and the cooling history of the shallow mantle near a spreading ridge.

Geological setting

Hole BA4A was sited ~500 m north-northwest of Site BA1, at the southern tip of a large, shallowly south-southwest–dipping dunite body within harzburgite. The dunite body extends several kilometers to the northwest and is ~500 m wide at its southern end. The dunite is cut by minor harzburgite layers and pyroxenite and gabbronorite dikes.

Minor drill pad preparation was necessary at this site to level the alluvium and some small patches of dunite outcrop to ensure that Hole BA4A could be sited as close to the dunite outcrop as possible, minimizing the thickness of alluvium that had to be drilled. A small extension of the existing track from Site BA1 was required for access across the wadi gravels.

Operations

An overview of all holes drilled is given in Table T3 in the **Methods** chapter. Drilling operations and core curation information for this hole are reported in Table T1.

Hole BA4A drilling summary

- Spud in: 14 Feb 2018, 09:51 h
- First core on deck: 14 Feb 2018, 10:20 h
- Surface casing (HW) installed: 14 Feb 2018, 5.70 m below ground level (mbgl)
- Surface casing extended: 15 Feb 2018, 24.00 mbgl
- Surface casing extended: 17 Feb 2018, 32.70 mbgl

[1] Kelemen, P.B., Matter, J.M., Teagle, D.A.H., Coggon, J.A., and the Oman Drilling Project Science Team, 2020. Site BA4. *In* Kelemen, P.B., Matter, J.M., Teagle, D.A.H., Coggon, J.A., and the Oman Drilling Project Science Team, *Proceedings of the Oman Drilling Project*: College Station, TX (International Ocean Discovery Program). https://doi.org/10.14379/OmanDP.proc.2020
[2] OmanDP Science Team affiliations.

MS OmanDP-118
Published 12 November 2020

- NW casing installed: 17 Feb 2018, 32.70 mbgl
- Final core on deck: 28 Feb 2018, 09:41 h
- Total depth (TC) of borehole: 302.70 m

Geology summary

Mainly serpentinized dunite with minor serpentinized harzburgite and thin dikes of gabbro and pyroxenite.

Technical issues

Had to redrill a vertical borehole for HW casing from 22.99 to 35.70 mbgl because original hole started going in an oblique direction. Needed to extend casing to 32.70 mbgl due to total loss of circulation. Large-diameter core was recovered from the redrilled section that was "cored" by the casing and shoe-bit. It was not possible to scan this core with the core scanner and box it. The microbiology team took the whole core section and bagged it up. However, recovered length and tablet photos were taken.

Operations summary

- 13 Feb 2018: mobilize rig, drilling equipment, and other accessories from Hole BA1B to Site BA4. Site rehabilitation at Hole BA1B and transportation of core boxes to Muscat.
- 14 Feb 2018: started drilling with HQ drill bit assembly; drilled from ground level to 23.70 mbgl and installed HW surface casing with shoe bit from 0.30 to 5.70 mbgl.
- 15 Feb 2018: drilled with HQ drill bit assembly to 35.70 mbgl. Total loss of circulation of drilling fluid at 30.00 mbgl. Extended HW surface casing to 24.00 mbgl.
- 17 Feb 2018: needed to extend casing to ~30 m due to loss of circulation, but casing was stuck at 28.20 m. When pulled out of the hole (POOH) a long section of rock was stuck inside the casing. The rock totaled 5.21 m of ~100 mm diameter "core," curated as a Core 14M. Core 14M was crescent shaped in cross-section due redrilling of an interval already drilled, with slight deviation from vertical (probably of both holes). Almost all of the HW Core 14M was reconstructed into a single piece and matched a gabbro dike (12 cm thick) with the same feature in Section 9Z-4. Hence, we constrained the drilled depth (using the top of Core 10Z, which is 23.70 m) and by extrapolation, the top depth of Core 14M (22.99 m). J. Coggon made the decision to give this core, which the geo team cannot store or ship, to the microbiology team. It could not be whole-round scanned due to its crescent-shaped cross-section, so was curated as a single section. The microbiology team bagged up entire Core 14M after the recovered length and tablet photos were taken. Continued coring with HQ drill bit assembly to 38.70 mbgl.
- 18–19 Feb 2018: cored with HQ drill bit assembly to 113.70 mbgl.
- 20 Feb 2018: cored with HQ drill bit assembly to 152.70 mbgl; complete loss of circulation of drilling fluid.
- 21 Feb 2018: cored with HQ drill bit assembly to 176.20 mbgl; POOH to change drill bit and ran in hole (RIH).
- 22–28 Feb 2018: cored with HQ drill bit assembly to 303.70 mbgl (TD). Completed core boxes and ICDP core scanner were transported to Muscat.
- 01 Mar 2018: POOH and demobilization of rig and all equipment and accessories. Site rehabilitation work and wellhead construction completed. End of Phase 2 drilling operations.

Background description

Hole BA4A provides material from 302.17 m of shallow mantle lithosphere and 0.61 m of alluvium. Abundances of the different lithologies, their variation with depth, and their modes were measured (Figs. **F2**, **F3**, **F4**, **F5**; Table **T2**). Almost two-thirds of the rocks in terms of volume are dunites, with ~25% harzburgites. The remaining core consists of gabbro (2.0%), olivine gabbro (6.8%), clinopyroxenite (1.2%), and wehrlitic dikes (0.4%) and clinopyroxene-rich dikes. There are no systematic trends in the distribution of the units or mineral modes with depth.

Alteration is pervasive and extensive with few fresh minerals preserved. Harzburgites alter mostly to serpentine, with preservation of olivine and orthopyroxene cores in some samples. Alteration of the dikes is also pervasive and almost complete. Calcium-rich alteration products of gabbroic minerals are found inside the dikes and also in veins that emanate from the dikes. Especially intense alteration is associated with zones of brecciation and multiple intrusions of small deformed dikes. Veins are ubiquitous in all units. A complete description and frequency of veins and the structures associated with deformation zones are provided in **Veins** and **Structural geology**, respectively.

Lithologic units and subunits were defined in the context of changes in lithology, mineral assemblage, modal abundance, structural and textural variations, alteration, veining, and fracturing. A complete description of individual units and subunits is available in Supplemental Tables **ST1** (all visual data recorded by background description team) and **ST2** (lithologic unit summary). The results presented below are supported by X-ray diffraction (XRD) and chemistry analysis.

Hole BA4A is one of three holes drilled in Oman in close proximity. A comparison between the lithologies and characteristics of rocks from these holes is provided.

Lithologic sequence

Hole BA4A contains a single major lithologic sequence composed of almost 300 m of dunite with subordinate harzburgite cut by a variety of gabbroic and clinopyroxene-rich dikes. Alluvium lies at the top of the sequence and is underlain by an ~11 m thick oxidized zone that hosts abundant carbonate veins. The alluvium and oxidized zones are described below. Lithologies in the rest of the core show relatively little variation with depth and are therefore grouped for the purposes of lithologic description and described in detail in **Principal rock types**. The depths and properties of the sequences are summarized in Table T3.

The alluvium zone is 0.61 m long and consists of mafic to ultramafic pebbles of various sizes, reflecting the lithology of the landscape surrounding Hole BA4A. The dunitic sequence begins at the point from which only massive peridotitic rocks are recovered.

The dunite sequence starts at 0.61 m and ends at 302.78 m (Sections 1Z-2 through 109Z-4) and consists of dunite with harzburgite zones and gabbroic and clinopyroxene-rich dikes (Figs. F2, F3). Harzburgitic patches occur throughout the sequence. The first sequence is described at 8.2 m depth but progressively increases in frequency at the bottom of the hole (Fig. F3). Peridotite typically contains a few percent spinel minerals, and harzburgite orthopyroxene content is usually 10%–30%. Dunite can contain orthopyroxene in the vicinity of harzburgitic patches (Fig. F4B). Alteration is pervasive (70%–100%) with most rocks at the upper end of this range. Most of the dikes are extensively altered with signs of calcium mobility associated with rodingitization. All the dikes are therefore considered to be rodingitized to some extent. The composition of harzburgitic units or composition and frequency of dikes with depth in Hole BA4A show no systematic trends (Figs. F2, F3, F4, F5).

Rocks from the top of the dunite sequence to ~11 m are highly oxidized and sufficiently different from those in the rest of the hole that they are described briefly in this section. The characteristics of the rocks deeper than 11 m are summarized in **Principal rock types**.

The oxidized zone consists of red-weathered, oxidized carbonated dunites, harzburgites, and dikes from the uppermost 11 m of the sequence below the alluvium (Figs. F6, F7). The oxidation of these rocks is assumed to be an effect of surface weathering. Oxidized zones are more intense in the vicinity of fractured zones. In these uppermost rocks, no information on grain size or shape could be recovered from dunite because of their intense alteration. The grain size of harzburgite has been estimated to be coarse based on orthopyroxene pseudomorphs with a maximum grain size up to 9 mm and average grain sizes of 2–5 mm. Except for two clinopyroxenites, all dikes in the oxidized zone are gabbroic with grain sizes varying from fine to coarse grained. Although the alteration level made any precise description difficult, pseudomorphic replacement textures indicate that most of the olivine and clinopyroxene are subequant and subhedral. Carbonate veins as thick as 2 cm are common, with >25 veins >5 mm thick through the zone and many more thinner ones. Large veins are restricted to the most oxidized zone in the uppermost 8 m of the sequence.

The thin section available from this zone (Sample 5Z-2, 56–61 cm; 10.25 m) has an orange color. The inferred protolith to the rock is a harzburgite. The thin section contains partially altered olivine, orthopyroxene, and spinel. In most cases, the cores of olivines are completely altered and are an orange-brown color. Small islands of olivine (<3%) are retained plus rare pseudomorphs of orthopyroxene set in 95% serpentine matrix. The retention of olivine is consistent with XRD results (Sample 4Z-4, 64–69 cm), which suggests the presence of olivine, orthopyroxene, and clinopyroxene in the oxidized zone (Table T4). Olivine grain size, determined from the spatial extent of olivine cores with common birefringence colors and extinction angles, is as large as 6 mm. Orthopyroxene is also mostly replaced by serpentine; the inferred size of precursor grains is 4–6 mm. Magnetite is relatively uncommon and is present only as Cr magnetite after spinel; it is not present in veins. Alteration consists of pervasive mesh-textured serpentine surrounding 100–300 µm cores that are altered in some cases and consist of fresh olivine in others (Fig. F8D).

Carbonate is common in veins in the oxidized part of the core. XRD results reveal that common alteration minerals in the top part of the sequence are serpentine plus magnesite, dolomite, and calcite (Table T4). Carbonate veins are mostly confined to the oxidized zone and decrease in abundance markedly with depth but were identified as deep as 42.5 m in the core (Sample 20Z-2, 7 cm; Table T4).

Principal rock types

The principal rock types observed with percentages by integrated thickness were dunite (63.9%), harzburgite (25.7%), olivine gabbro (6.8%), gabbro (2.0%), clinopyroxenite (1.2%), and wehrlites (0.4%) (Fig. F2; Table T3). Rocks defined as werhlites included disseminations of clinopyroxene within the host dunite or harzburgite and clearly co-crystallized olivine-clinopyroxene intrusions.

Dunite

Typical unoxidized dunites are a dull black-gray, massive, and homogeneous (Fig. F7B). Olivine in dunites from Hole BA4A is pervasively altered, but some information on the primary mineralogy is provided by relict and pseudomorphed orthopyroxene grains, which are generally a paler gray than the black/brown/gray host rock, and by spinel grains, which display distinctive shiny faces in the core. Rarely, dull black olivine cores could be distinguished in the core, more often in the lower half, but the grain size of these relics was not measured because it was assumed that they did not record the original grain size. Orthopyroxene grains are subequant and subhedral to anhedral with an average grain size of 0.2–5 mm (maximum = 10 mm). Orthopyroxene modes in the dunite range 0%–10%. The percentage of alteration is always estimated as close to 100%. The distribution of oxidized zones in the peridotite was noted with distinction between completely oxidized units and locally oxidized units with oxidation along cracks, dikes, and in patches (Fig. F6). Completely oxidized portions make up 11.8% of the sequence (35.6 m), and locally oxidized portions make up 10.9% of the sequence. A total of 83.5% of oxidized zones are in dunite (57.2 m). Oxidation decreases downhole through the sequence, though pervasively oxidized zones occur as deep as 290 m (Fig. F6).

Within the dunite sequence, which is taken to begin at 11 m, dunites consist of >95% mesh-textured serpentine cut by serpentine veins plus 1%–5% spinel minerals. Details of the various vein generations that crosscut the mesh are provided in **Veins**. Olivine is preserved as relict islands 100–300 µm across in some thin sections (e.g., Sample 56Z-1, 85–90 cm; 150 m). However, in the majority of dunite thin sections, olivine is completely altered to serpentine with the formation of mesh textures cored by serpentine. These cores are either black (Fig. F8C), clear (Fig. F8D), or in rare cases intermediate with black cores and clear rims (Fig. F8E). Mineral abbreviations are after Whitney and Evans (2010) except where noted in the figure captions. Black-cored olivine is the most common type. The proximity of veins is often associated with a loss of coloration in the black cores to produce colorless cores. Clear cores occasionally display a texture consisting of concentric rings (Fig. F8E, F8F). This texture, referred to as a fingerprint texture, has been described previously only from surface samples in the Oman ophiolite from the Batin area (Noel, 2018) and in Hole BA3A (see the **Site BA3** chapter). This previous work has shown that the rings consist of alternating Fe- and Mg-rich serpentine (Noel, 2018). In the most altered samples, original olivine textures are completely obliterated by progressive overprinting serpentine veins. Brucite was not identified in thin section but is identified as a subsidiary mineral in dunites throughout the core (e.g., Sample 47Z-4, 74–79 cm; 125 m; Table T4).

Accessory minerals include Cr magnetite (Fig. F9A) and minor magnetite. Magnetite is present in veins in some samples but can be completely absent in veins, in which case it is restricted to replacement of original aluminous spinel. Sulfides are present in low abundances in most sections and generally as <30 µm grains. However, grains as large as 400 µm are observed. Principal phases are heazlewoodite and chalcopyrite. Chalcopyrite grains as large as 200 µm are also present, and these are altered at the margins to cuprite and/or bornite in some cases (Fig. F9C).

Harzburgite

Harzburgites make up ~25% of the rocks in Hole BA4A (Fig. F2). There is no apparent systematic variation in the distribution of harzburgites with depth (Fig. F7). First inspection of mineral modes suggests that there may be cyclical variation in orthopyroxene mode within harzburgite units (Fig. F3). Orthopyroxene modes appear to increase gradually with decreasing depth in the core from zero over a distance of 15–20 m and then drop sharply at the top of the unit. There are repeated cycles of this type throughout the core. Core photos were inspected after logging was complete, and this trend was found to be an artifact. It is recommended that differences in mineral mode of <5% should be treated as within uncertainty.

The harzburgites are massive and black/gray in color (Fig. F7C). In hand specimen, orthopyroxene and altered orthopyroxene in the harzburgites can be distinguished clearly from the altered olivine by its paler gray color. Grains are subequant and subhedral to anhedral, and their average size is generally 2–5 mm (maximum = 10 mm). The largest grain measured is 15 mm. Some units (Units 5e [17.5–17.7 m], 6a [19.2–21.6 m], 16a [74.8–75.2 m], 18a [80.8–82 m[, and 27b [155.5–157.1 m]) display variations in orthopyroxene content that could be related to banding. Bands are not always well defined, and variations can be from centimeter to meter scale. No foliation was described. Veins are ubiquitous and varied. A full description of the different vein types is provided in **Veins**.

Harzburgites fall into three groups:

1. Those with minimal clinopyroxene and only orthopyroxene relics preserved (e.g., Sample 52Z-4, 0–5 cm; 140 m),
2. Those with minimal clinopyroxene and relict orthopyroxene (e.g., Sample 95Z-1, 25–30 cm; 258 m), and
3. More clinopyroxene-rich samples with or without orthopyroxene relics (e.g., Sample 31Z-1, 55–57 cm; 75.3 m).

A typical inferred protolith mode is 80% olivine, 15% orthopyroxene, 2% clinopyroxene, and 2% spinel.

All groups share certain characteristics. Original olivine in the samples has been >95% serpentinized and is replaced by a green and brown serpentine mesh texture that surrounds mesh cores 100–200 µm across. The original olivine grain size, identified from areas with common extinction angles, is 2–5 mm. Serpentine mesh cores can be black, clear, or both, and all types can occur together in the same thin section (e.g., Fig. F10A). Relict olivine is more commonly preserved in the harzburgites than in the dunites, and the extent of alteration is generally less in the harzburgites.

Precursor orthopyroxene grains were 2–6 mm in size and occurred singly or occasionally as aggregates of 2–6 grains. Twinned grains are observed (Fig. F10B). Alteration of orthopyroxene to serpentine, and sometimes chlorite is extensive but usually incomplete with islands of orthopyroxene within surrounding serpentine (Fig. F10C, F10D). Talc is only rarely observed as an alteration product after orthopyroxene but when present can be seen as 100 µm needles in sheaves (e.g., Sample 109Z-4, 75–81 cm; 302.6 m; Table T4). Initial results suggest that orthopyroxene destruction is more complete in the upper part of the core, but further work is necessary to substantiate this. Deformation of serpentinized orthopyroxene is associated with veins in some places (Fig. F10E, F10F).

Clinopyroxene occurs spatially associated with orthopyroxene as lamellae of clinopyroxene within orthopyroxene, as small euhedral clinopyroxene grains 100–500 µm across, and as lobate grains in interstitial settings (e.g., Fig. F10E–F10H). In samples with higher clinopyroxene mode, clinopyroxene can occur as prismatic grains that are part of the orthopyroxene aggregates. Alteration of clinopyroxene is often associated with a black coloration of the thin section slide (Fig. F10G, F10H).

Opaque minerals are spinel and magnetite after spinel (e.g., Fig. F11A). Vein magnetite is rare or absent in most sections but present in a minority of thin sections (e.g., Fig. F11B). Chalcopyrite occurs as widely distributed grains <50 µm in size, making up <1% of the mode. Coliform cuprite and bornite rims are common on chalcopyrite (e.g., Fig. F11C). Sulfides record deformation (e.g., Fig. F11D). The modes of sulfides and magnetite are not related in an obvious way to the extent of alteration. For example, thin section Sample 95Z-1, 25–30 cm, taken at 258 m, contains 100–200 µm sulfides with relatively fresh orthopyroxene and clinopyroxene and well-preserved olivine (20% remaining) even though the sample is immediately adjacent to a large vein.

Basaltic and ultramafic dikes

Dike thickness ranges from a millimeter to >1 m. Dike compositions ranged from gabbros to clinopyroxenites, via olivine gabbros and wehrlites. There is no obvious systematic trend in dike type with depth or in dike frequency with depth (Fig. F5). Some dikes are composite with evidence of multiple intrusions in the form of symmetrical variation of grain size and/or composition through the dikes. The separate dikes that contribute to these composite dikes are not systematically different in mineralogy or texture to dikes of the type that are not composite. Composite dikes are therefore not considered separately here.

Gabbro dikes

Gabbros occur as dikes in the harzburgite and dunite with thickness from millimeters to 45 cm (e.g., Fig. F7D). The dikes often appear horizontal or close to horizontal in the plane of the half core; vertical dikes are not observed, although the probability of encountering these, if they exist, is relatively low. The gabbros do not preferentially intrude the dunite or harzburgite (Table T5). General grain size varies from fine grained to pegmatitic, and varitextured or seriate dikes are common (49%). Olivine composes as much as 5%, plagioclase varies 10%–85%, and clinopyroxene varies 13%–90%. All minerals have subequant and subhedral habits and shapes. Gabbros are a common constituent of the composite dikes (e.g., Sample 22Z-4, 79–82 cm; 50.6 m). Alteration is 70%–100%.

All of the 21 gabbros examined in thin section are comprehensively and pervasively altered with plagioclase and olivine completely destroyed and clinopyroxene mostly retained to some extent. In the less altered samples, referred to here as the pseudomorphically replaced gabbros, grain shapes are retained and the precursor mineralogy can be identified using color differences between the alteration phases. For example, in thin section Sample 40Z-1, 33–35 cm (102 m), precursor olivine grains as large as 4 mm are replaced by serpentine + chlorite mesh textures with 100–300 µm cores remaining (Fig. F12A, F12B). Talc is also identified by XRD (e.g., Sample 43Z-1, 15.0 cm; Table T4). Initial plagioclase grains are recognizable from the extent of replacement clay minerals, which suggest that plagioclase originally occupied interstitial positions in the gabbro. Clinopyroxene is the best-preserved phase, presenting primarily as prismatic 4–7 mm clinopyroxene grains that contain clay-altered plagioclase inclusions (Fig. F12C, F12D) and to a lesser extent as smaller grains on interstitial sites. Clinopyroxene grains often form multigrain clusters. Clinopyroxene in the pseudomorphically altered gabbros can be associated with tremolite on its margins (Fig. F12E, F12F), but this is

not commonly observed, consistent with the XRD results (Table T4). Hydrogrossular occurs on vein margins (Fig. F12G, F12H) and is identified frequently in the XRD data along with xonotlite (Table T4). Equant, euhedral to subhedral grains of chalcopyrite spatially associated with alteration products such as cuprite and bornite occur with a mode <1%, with grain size up to 200–300 µm.

A lithologic unit worthy of special note is the pegmatitic gabbro found in interval 11Z-4, 28–30 cm. The mineralogy and textural relationships in this gabbro are similar to those in the pseudomorphically replaced gabbros, but grains as large as 80 mm were recorded (Fig. F13A). Vein formation in these gabbros is associated with phases similar to those seen in the gabbros and olivine gabbros, such as carbonate, prehnite, hydrogrossular, and xonotlite, which occur in zoned and sometimes coliform composite veins (Fig. F13B, F13C; Table T4).

With increasing alteration and, potentially, deformation, the pseudomorphic relationship between the precursor phase and alteration phases is lost. Altered olivine continues to present as serpentine and chlorite mesh textures with 100–300 µm serpentine mesh cores up to the point of extreme alteration (e.g., Sample 84Z-4, 14–17 cm; 227.2 m), at which point the mesh textures are destroyed in favor of massive cryptocrystalline serpentine. Clinopyroxene is frequently preserved to some extent, with as much as 30% of the original grain retained even in the most altered samples (Fig. F14A, F14B). Clinopyroxene pseudomorphs are visible in many sections, with alteration focused on the cleavages and margins of the grains (Fig. F14A, F14B). In the most extreme cases of alteration, clinopyroxene alters to deformed aggregates of prehnite (e.g., Fig. F14C, F14D) or chlorite and tremolite with prehnite on the margin (Fig. F14E, F14F). In the most extreme case of alteration examined, Sample 19Z-3, 40–42 cm (40.3 m), two pseudomorphed grains have transformed to different assemblages but are <5 mm apart (Fig. F14A, F14B, F14E, F14F). In all sections, plagioclase is completely altered to clay and other isotropic phases. These soft plagioclase-derived alteration phases are often smeared out along dike contacts or faults.

Ca-bearing phases observed in the most altered examples include millimeter-sized prismatic titanite in Sample 95Z-2, 16–18 cm (258.7 m; Fig. F15A, F15B). Phlogopite is also occasionally present based on XRD results (e.g., Sample 83Z-3; 69.0 cm; Table T4). Small sulfides, forming <1% of the mode, scatter through the altered gabbroic dikes. Veins are common within and emanating from these dikes, and these can include calcic phases such as prehnite (Fig. F14C, F14D) and carbonate (Fig. F14E, F14F) in zoned, serpentine-lined veins. These veins are discussed in detail in Veins. Opaque phases are rare in the most highly altered gabbros.

The growth of calcium-bearing phases in veins, the extension of these veins out into the host rock, and the formation of serpentine in the gabbros in locations other than after olivine suggests metasomatic redistribution of calcium and magnesium on the millimeter to centimeter scale. These dikes, therefore, are referred to as rodingitized.

Olivine gabbro dikes

Olivine gabbros occur as dikes in harzburgite and dunite with thickness varying from <5 mm to 150 cm (e.g., Fig. F7E). These dikes, like the gabbro dikes, often appear horizontal or close to horizontal in the plane of the half core. Further details of the orientation of the dikes is provided in Structural geology. There is some evidence from the calculated number of dikes per meter of host lithology that the olivine gabbros preferentially intrude the harzburgite units (Table T4). Grain sizes range 0.5–40 mm. Varitextured olivine gabbros are common (49%) with the remainder equigranular. Olivine content ranges 6%–60%, plagioclase 5%–70%, and clinopyroxene 10%–85%. Olivine gabbros are a common constituent of the composite dikes (e.g., Sample 22Z-4, 79–82 cm; 50.6 m). As for gabbros, the alteration extent ranges 70%–100%.

Only one thin section was sufficiently unaltered for plagioclase to be preserved (Sample 40Z-1, 54–56 cm; 102.2 m), described in detail here. In this sample, olivine, clinopyroxene, and plagioclase form an equigranular texture of 0.5–1.5 mm, mostly equant subhedral grains separated in parts of the thin section by zones of 100–300 µm crystals (Fig. F16A, F16B). These fine-grained zones occupy 10% of the rock. Olivine occurs as 100–1500 µm anhedral subequant grains and is almost fresh. The olivine mode is 20%. Clinopyroxene grains are a similar size to olivine, with anhedral to euhedral, equant, almost unaltered grains and forms 30% of the mode. Clinopyroxene grains are mostly granular but occasionally prismatic and can be twinned. Plagioclase presents as granular equant subhedral crystals 400–1000 µm across and forms 50% of the mode. Plagioclase composition, determined from the extinction angle, is 60%–70% An. Alteration is limited to the finer grained parts of the sample (Fig. F16C, F16D). Alteration phases include 100–200 µm tremolite crystals, chlorite, and serpentine in the fine-grained zones between crystals. A small proportion (<5%) of pale brown amphibole, a few hundred micrometers across and with a platy habit, also occurs in this section (Fig. F16D, F16E). Magnetite occurs in this sample (Fig. F17A) preferentially in areas of alteration. Magnetite occurs as anhedral subequant to elongate grains up to 200 µm across or as vein magnetite (Fig. F17B). Magnetite, in

some cases, includes sulfide minerals (Fig. F17B). Native copper and copper and nickel sulfides are also present in the matrix and exhibit complex textural relationships (Fig. F17B–F17D). However, sulfides do not contribute >1% of the mode.

The rest of the olivine gabbros are more altered, and the description that follows is generic. Where the dikes are not deformed, the products of breakdown of the original phases form pseudomorphs after the original igneous phases (e.g., Sample 22Z-4, 79–82 cm; 50.6 m). Olivine, inferred to have been present as rounded subequant grains 2–7 mm across and with modes ranging 5%–30%, is replaced by a network of serpentine with or without chlorite, leaving only olivine cores 100–300 µm in size within a mesh texture. From 60% to 100% of the olivine is replaced in this way (Fig. F18A, F18B). Plagioclase, which is inferred to have occurred interstitially as 0.5–8 mm grains with a mode of 20%–60% in the protolith based on the distribution of the alteration phases, is replaced by either a brown clay phase (e.g., Fig. F17C, F17D) and/or an unidentified isotropic, high relief, opaque phase. Clinopyroxene is the mineral most resistant to alteration, and partially reacted prismatic clinopyroxene grains are common. Clinopyroxene grains are subequant, prismatic, and 0.5–8 mm across, forming 20%–60% of the mode. Clinopyroxene grains can be poikilitic and include 50–300 µm inclusions of plagioclase or olivine, which are usually altered to clays or serpentine/chlorite. Clinopyroxene breakdown products are not distinctive in the same way as those for plagioclase and olivine at this level of alteration but are inferred to be a mixture of clay, serpentine, and chlorite. Tremolite is observed in some thin sections, generally those with lesser extents of alteration. Veins in pseudomorphed olivine gabbros can be carbonate bearing; XRD analysis of veins in an oxidized dunite reveal dolomite (Sample 9Z-4, 44.0 cm; 23 m) (Table T4).

The pseudomorphic style of alteration can occur even adjacent to faults, so long as the gabbros themselves are not deformed (e.g., Fig. F18E, F18F). Accessory minerals include 20–100 µm grains of chalcopyrite (Fig. F17E) that are altered when cut by the alteration.

Identification of precursor minerals becomes considerably more difficult when deformation or other factors such as high fluid/rock ratios obliterate evidence of the igneous texture (e.g., Sample 32Z-3, 14–17 cm; 79.5 m). This type of alteration is common in olivine gabbro dikes less than a few centimeters across. Alteration phases include mats of prehnite with serpentine (e.g., Fig. F19A, F19B), hydrogrossular in and adjacent to veins (e.g., Fig. F19C, F19D), serpentine after hydrogrossular with chlorite, and tremolite after clinopyroxene (e.g., Fig. F19E, F19F). Modes of sheet silicates in the most altered rocks are as high as 70%. The high sheet silicate content facilitates deformation, and these rocks commonly show moderate to strong mineral preferred orientation locally but not consistently through the thin section (e.g., Fig. F19E, F19F). Opaque phases in the most altered gabbros include abundant copper sulfides <10 µm in size that are distributed through the matrix and can be included in hydrogrossular (e.g., Fig. F19D) plus euhedral magnetite as long as 500 µm (Fig. F17F). Rare 100 µm grains of ilmenite were found in Sample 32Z-3, 14–17 cm (79.5 m).

Clinopyroxene-dominated dikes

Clinopyroxene-dominated dikes include wehrlitic and clinopyroxenite dikes (Fig. F7F, F7G). Orthopyroxene-dominated dikes are not observed. Clinopyroxenites represent 1.1% of the total thickness of the dunitic sequence with thicknesses up to 37 cm. Wehrlite makes up 0.5% of the sequence with thicknesses up to 22 cm. In both cases, the most common dike thickness is ~2 cm. Olivine makes up to 85% of these dikes. Grain sizes vary from fine to coarse. Varitextured dikes are rather common. Olivine and clinopyroxene shape and habit mostly subhedral and subequant, respectively. Alteration is commonly pseudomorphic, and the extent of alteration ranges 50%–100%.

In thin sections, clinopyroxene, which can form >80% of the mode of these dikes, is relatively unaltered in most cases and retains prismatic to subhedral shape with grains 3–6 mm along the longest axis (e.g., Sample 71Z-2, 5–10 cm; 189.7 m). Strain bands in clinopyroxene are observed (e.g., Fig. F20A, F20B) as well as rare inclusions presumed to have once been plagioclase (e.g., Sample 51Z-1, 5–9 cm; 134.8 m) and more common inclusions as large as 1 mm that are altered to serpentine plus chlorite (e.g., Fig. F20C, F20D). These inclusions are inferred to have been plagioclase and olivine, respectively. Plagioclase inclusions are much less common as an inclusion phase in clinopyroxenes in the wehrlitic and clinopyroxenite dikes than in the gabbroic dikes described above. Magnetite inclusions are also found in the clinopyroxene (e.g., Fig. F21A). Clinopyroxene grains are separated by pervasively altered cryptocrystalline matrix serpentine. Olivine is rarely preserved but where present it forms 100–300 µm island cores surrounded by a mesh texture of serpentine with or without chlorite. Original olivine grain size, inferred from the extent of common interference colors and extinction, was 2–6 mm.

Alteration of clinopyroxene sometimes produces sparse and apparently randomly oriented tremolite needles in the matrix between the clinopyroxene grains (Sample 71X-2, 5–10 cm; 189.7 m; Fig. F20E, F20F). In some places, the serpentine alteration matrix wraps around the margins of clinopyroxene grains (Fig. F20G, F20H). Where precursor plagioclase is inferred, it is pervasively and completely

altered to isotropic phases, primarily clay minerals. The calcium-rich phases found in the altered gabbro dikes, which include hydrogrossular, prehnite, and carbonate, are not found in the clinopyroxene-dominated dikes except for a small proportion that exhibit the most extreme extent of alteration. In one highly altered clinopyroxenite dike at 21 m, green minerals were observed in hand sample and hydrogrossular and a calcic amphibole were identified by XRD (Sample 9Z-1, 41.0 cm; Table T4).

Elongate grains of copper, up to 70 µm long, are found on grain boundaries, in fractures in grains, and within hematite in one of the less altered clinopyroxenites (Sample 71Z-2, 5–10 cm; 189.7 m; Fig. F21B, F21C). Copper sulfides in this sample are rare, though an isolated 30 µm euhedral bornite grain is observed. Hematite in this dike is observed in a serpentine vein and as tabular crystals and anhedral equant grains at the margins of grains. The opaque assemblage in this less-altered dike is sulfur poor and notable for the presence of hematite rather than magnetite, which is consistent with different redox state and/or sulfur fugacity in these dikes to that in the more common lithologic units in the sequence. In the more altered clinopyroxenite dikes, copper sulfides are disseminated in the matrix. Magnetite occurs in veins and as subequant subhedral grains to 400 µm. Sulfides and magnetite together make up <1% of the mode of the rock (Fig. F21D).

Disseminated clinopyroxene dikes

Clinopyroxenite and wehrlite dikes can present as disseminations in host dunite (e.g., Sample 48Z-1, 38–42 cm; 126.1 m; Fig. F7H). In these rocks, 2–6 mm clinopyroxene grains with modes of 20%–70% occur in 2–8 cm thick bands with well-defined modal contacts. Clinopyroxene grains in these bands are subequant and subhedral to anhedral. Other minerals are not identifiable in hand specimen. These dikes were logged as wehrlites or clinopyroxenites, depending on mode, but are sufficiently distinctive that they are discussed separately here.

Microscopic characteristics are based on the study of a single thin section available for this rock type, Sample 48Z-1, 38–42 cm (126 m). In this section, altered 3–6 mm clinopyroxene grains are apparently randomly oriented in a serpentine mesh-textured matrix after olivine. Unaltered or less-altered cores to the clinopyroxene grains commonly remain with the margins and cleavage altered to a black color inferred to be due to cryptocrystalline clay phases and iron oxides with minor <100 µm chlorite and tremolite (e.g., Fig. F22A, F22B). Chlorite and tremolite are not observed in contact with each other, and indeed tremolite is relatively uncommon in the XRD results for Hole BA4A (Table T4). Clinopyroxenes in this section are the least well preserved of those in all the clinopyroxene-bearing lithologies in Hole BA4A, and completely altered clinopyroxene grains are present (Fig. F22C, F22D). Precursor olivine is completely or almost completely converted to a serpentine mesh texture surrounding 100–300 µm serpentine cores that can be dark, pale, or a bluish intermediate color (Fig. F22E, F22F). Fresh olivine and the Ca-rich phases such as hydrogrossular, prehnite, and xonotlite that are found in the altered gabbros are not observed.

Spinel as aggregates up to 200 µm were found in the olivine-rich parts of Sample 48Z-1, 38–42 cm. These aggregates consist of multiple grains, each as large as 80 µm, identified as magnetite associated with a paler gray-white and more reflective phase interpreted as hematite (Fig. F23A). Scattered small chalcopyrite grains as large as 20 µm and altered to magnetite on the margins also occur in the olivine-rich part of this rock (Fig. F23B). Spinel modes are generally around or <1%, whereas the copper sulfide mode is <<1%.

Breccias

Brecciated units occur at 78.6–80 m depth (Sections 32Z-2, 32Z-3) and 208.9–210.1 m (Sections 77Z-4, 78Z-1) in Hole BA4A (Fig. F24A, F24B). Angular to subangular dunitic clasts from millimeter to several centimeters in size are separated by zones of gabbroic melt. Clasts exhibit an alteration zone that is 1–5 mm wide at the margins. White veins oriented perpendicular to the clast/gabbro contact and penetrating 5–30 mm into the clast and the gabbroic melt are common (Fig. F24C, F24D).

In thin section, the dunite and gabbroic lithologies show similar characteristics to highly altered dunites and gabbros elsewhere and as described above (e.g., dunite Sample 19Z-3, 0–6 cm [39.9 m], and gabbro Sample 32Z-3, 14–17 cm [79.5 m]). Olivine in the dunite clasts is completely replaced by mesh-textured serpentine that surrounds 100–300 µm serpentine-mesh cores. Minerals originally present in the gabbro, where identifiable, are altered to clay for plagioclase, serpentine, and chlorite for olivine and occur as less-altered cores, partially altered to clay, oxides, and serpentine with black coloration on the cleavages and margins for clinopyroxene, as seen in the disseminated clinopyroxenites (Fig. F22A, F22B).

Although the mineralogy is complex, two distinguishable alteration zones occur, broadly speaking, at the clast/gabbro margin. Localized fracturing and possible deformation means that the distribution of these zones is chaotic. The zone closest to the gabbro is composed of, in approximate order of abundance, 100–200 µm prehnite, cryptocrystalline serpentine, up to 500 µm grains of chlorite, 30–40 µm hydrogrossular, and xonotlite in places (e.g., Fig. F24E, F24F). The mode varies with location in the slide. The presence of xonotlite is confirmed by XRD (Sample 77Z-1, 81.0 cm; Table T4).

Monomineralic patches of prehnite, serpentine, and chlorite are present at the millimeter scale in thin sections (e.g., Sample 32Z-2, 22–26 cm; 78.7 m). Chlorite-magnetite-serpentine zones, several millimeters wide, are also present on the clast side of the alteration (Fig. F24G). Chlorite is relatively pale, suggesting, as elsewhere, Mg-rich composition. Magnetite grains are 10–30 µm in size and occur preferentially associated with serpentine in this zone. Colorless phlogopite is also present based on XRD results (Sample 77Z-4, 12.0 cm; Table T4).

Scattered sulfides, generally <30 µm in size and including chalcopyrite, occur throughout all alteration zones, forming <<1% of the mode. Magnetite occurs as grains as large as 1 mm that are interpreted to have replaced spinel that was part of the precursor dunite assemblage and, to a lesser extent, in veins. Magnetite overall makes up ~1% of the mode of these rocks.

Gabbro injection with ductile deformation

Another unit worthy of note consists of dunites intruded by multiple thin gabbroic dikes that were then deformed (Fig. F25A). These units occur in Sections 95Z-3 (259.1 m) and 109Z-2 (from 300.3 m)

One thin section (95Z-3, 36–38 cm; 259.4 m) samples this lithology (Fig. F25B). The thin section is complex but can be divided broadly into two domains associated with the precursor lithologies. Both domains are zoned in places. In the domain most closely related to precursor host dunite, the principal minerals are olivine, serpentine, chlorite, and magnetite. Relatively unaltered olivine is preserved in places, in a matrix of serpentine alteration (Fig. F25C). Chlorite and magnetite increase, sometimes continuously and sometimes discontinuously, toward the edge of the zone. In contrast to the olivine, orthopyroxene in these domains is 100% altered. In the domain associated with the gabbroic intrusion, the principal minerals recognized in thin section are prehnite, talc, and amphibole (Fig. F25D, F25E). Amphiboles are pale brown to clear, prismatic, 0.5–3 mm in size, and sometimes zoned (Fig. F25E). In some parts of the thin section, amphiboles are at the margins of the calcium-rich areas but are also found inside the veins. There is no obvious systematic difference in amphibole characteristics between the two areas. Zoning in the amphiboles is inconsistently present and irregular.

Comparison with Holes BA1B and BA3A

Hole BA4A is one of three holes drilled in Oman in close proximity (see Hole BA1B in the **Site BA1** chapter and Hole BA3A in the **Site BA3** chapter). The three holes all penetrate shallow mantle lithosphere and consist of the same rock types: harzburgites, dunites, gabbroic dikes, and clinopyroxene-rich dikes. The extent of alteration is high in all three holes; generally 85%–100% of the rock is pervasively altered. Yet the proportion of the different lithologies and their distributions within the holes differs (Table T6). Hole BA1B is made up of two sequences, dunite with gabbro at the top of the hole and harzburgite with gabbro in the lower parts. In terms of thickness, the harzburgite with gabbro sequence is ~80% harzburgite with 5.1% gabbroic dikes and 3.7% clinopyroxenite and wehrlitic dikes. The dunite with gabbro sequence is ~80% dunite with 6.4% gabbroic dikes, 2.4% clinopyroxenite dikes, and no wehrlites at all. Hole BA3A is far more homogeneous, with 98% harzburgite, 0.2% gabbroic dikes, 0.1% clinopyroxenite dikes, and, like the dunite with gabbro sequence in Hole BA1B, no wehrlites. Hole BA4A is dunite dominated (64% dunite) and more dike rich than the harzburgites of Hole BA3A, with 8.8% gabbroic dikes, 1.1% clinopyroxenite dikes, and 0.5% wehrlitic dikes. No lherzolites are observed.

The fundamental variations in peridotite lithology with different proportions of dunite and harzburgite are not associated with consistent trends in the proportions and composition of the dikes. Gabbroic dikes are the most abundant in all holes, with gabbros more common in the dunite-dominated sequences of Holes BA1B and BA4A. The abundance of olivine gabbros and the ratio of olivine gabbros to gabbros in Holes BA1B and BA4A is slightly higher in the harzburgites than in the dunites, but this trend is not continued in Hole BA3A, which is mostly harzburgite (Table T6). There is no consistent trend in the abundance of clinopyroxenite dikes as a function of the host lithology. Wehrlitic dikes are the least common and are not observed at all in the dunite with gabbro sequence of Hole BA1B or the harzburgite-dominated Hole BA3A.

Increases in banding defined by orthopyroxenes and in modal sulfides and iron oxides are noted toward the lower parts of Holes BA1B and BA3A. These trends are not noted in Hole BA4A, so further work is needed to determine the significance of these trends and the extent to which they represent typical mantle processes.

Summary

Hole BA4A sampled just over 300 m of mantle material. The core is topped by alluvium, which lies above red-oxidized and carbonate-veined peridotites in the uppermost 11 m of the core. The remaining core comprises harzburgites (64%) and dunites (25%) cut by gabbroic (8.8%) and clinopyroxene-rich (1.6%) dikes. There are no systematic lithologic trends with depth in the core and no trends in mineral abundance. Fresh dunites are inferred to consist of olivine and spinel with minor orthopyroxene and clinopyroxene in some cases. Clinopyroxene, where present in these rocks, is often located at interstitial sites as

small grains. Fresh harzburgites are inferred to comprise olivine, orthopyroxene, and spinel, plus as much as 5% clinopyroxene.

Pervasive alteration is ubiquitous through the core. Dunites are always >90% altered. Alteration minerals identified in dunite include serpentine, brucite, and magnetite. Harzburgites are, on average, slightly less altered than dunites, but olivine is still completely destroyed in the majority of samples. Orthopyroxene alteration is less intense, and remnants of orthopyroxene remain in many samples. Alteration minerals include serpentine, chlorite, and rarely talc. Only one gabbroic dike with fresh plagioclase was sampled. In all the others, plagioclase is replaced by clay. Olivine is replaced by serpentine and chlorite in the gabbroic dikes. Clinopyroxene in the gabbroic dikes is the best-preserved mineral with alteration to tremolite at the margins of some grains. When clinopyroxene is completely replaced, it is usually replaced by chlorite and serpentine, but in some extreme cases calcic minerals such as prehnite are observed. Other calcium-rich minerals observed in the altered dikes and associated veins include xonotlite, carbonates, and hydrogrossular. Alteration of olivine and clinopyroxene in the wehrlitic dikes proceeds in a similar way to the gabbroic dikes except that clinopyroxene is more often heavily altered or completely replaced. Alteration in all types of dikes was, in many cases, pseudomorphic, so the original mineral distribution and textures can be inferred. In other cases, original textures were obliterated to produce fine-grained rocks. Alteration was more intense near some faults and veins, but there is not an overwhelmingly consistent trend for that relationship.

The presence of magnesium-rich alteration phases after calcium-rich minerals such as clinopyroxene and calcium-rich minerals in veins that extend beyond the dikes indicate that there was some element movement on at least the millimeter to centimeter scale.

The lithostratigraphy of Hole BA4A is summarized in Figure F26.

Veins

Veins in core from Hole BA4A were systematically logged for the same motivation and following the same procedures outlined in detail in the Hole BA1B Introduction in the **Site BA1** chapter.

In this report, we briefly reiterate the general characteristics of the different vein types recorded. We then present how different vein types and vein mineral assemblages vary as a function of subsurface depth.

As in the vein reports for the previous drill holes of the OmanDP, spreadsheets containing continuous downhole observations for veins, calculations, and downhole plots are given in supplemental Tables ST3, ST4, and ST5. Abbreviations used in the text and figures are defined in Table T5 in the **Methods** chapter.

Overviews of the overall downhole variation in vein mineralogy and area percentage of veins together with a summary of crosscutting relationships between different vein types are given in **Vein abundance, distribution, and crosscutting relations**.

The vein description team continued using the list of vein types developed during logging of the first core of Hole BA1B. The reasoning for using this list is provided in Hole BA1B Veins in the **Site BA1** chapter. Likewise, the cutoff for the type of vein recorded for the analyses of vein frequency and proportions in the core was adopted from previous reports of Leg 4. Hence, diffuse networks of veinlets on a tens of micrometer scale were considered part of the background alteration of mesh-textured serpentinite and were not logged. Likewise, dark serpentine-magnetite veins (type Sa, see below) were logged only when they were wider than 0.5 mm and stood out as a distinct feature of the core. Contrary to earlier reports, we did include Sa type veins in our vein statistics, but it should be noted that this vein type is underrepresented because the smaller and more diffuse veins were not recorded. The Sa type is the earliest and one of the most common vein types in the majority of core sections with serpentinized mantle rocks.

Observations

Macroscopic identification of vein types

The vein description team used a previously defined open-ended list of vein types for describing the veins encountered in the core (Fig. F27A). We recorded different types of veins that record variable interaction between fluids and rocks with variable, time-integrated reaction histories. We reason that in a drill core mutually crosscutting relationships between vein types are more straightforward to record than a specific sequence of veins (as in V1, V2, etc.) that could be established by field work.

In this section, we briefly describe each of the 10 vein types used in logging the core and provide examples for common appearances of vein types in the core.

Carbonate-bearing veins

Ca veins. Layered composite veins composed of green to black serpentine and carbonate minerals. They are abundant in the uppermost cores. Ca veins are divided into three subgroups based on their detailed appearance:

- Ca1: dark-colored serpentine cores with carbonate rims (Figure F27B),

- Ca2: carbonate cores with serpentine rims (Fig. F27C), and
- Ca3: waxy green serpentine and carbonate minerals (Fig. F27D).

Cb veins. White granular or porcelaneous veins of carbonate minerals (Fig. F27E) that occur in the uppermost cores together with Ca veins.

The abundance of both Ca and Cb veins decrease systematically with depth, and they are not observed in core below 76 m.

Serpentine veins

Serpentine vein types were classified based on color and texture. Whereas a distinction between the different vein types was commonly straightforward, ambiguous instances also occur. Those were logged as mixed types. Differences in color may be due to varying amounts, types, and distributions of iron oxides and oxyhydroxides and/or the presence of minor components (Al, Cr, Fe^{2+}, Fe^{3+}, and Ni) within the serpentine minerals themselves. Because serpentine colors are much less distinct in thin section, it was sometimes not evident which macroscopic vein types were present in specific thin sections.

Sa veins. Black network or branched veins of serpentine with microcrystalline magnetite (Fig. F27F). Sa veins occur throughout the core, irrespective of depth. In most cases, Sa veins are cut by other types of veins. In the lower part of Hole BA4A, Sa veins are difficult to see against the background of dark, strongly serpentinized harzburgite. Networks of Sa veins may gradually transition into a black microscopic mesh vein network that is part of the background alteration in these rocks. It is therefore difficult to discern where they rise to the level of through-going veins worthy of recording. Sa veins were logged in the core when they were obvious and continuous, commonly as conjugate sets of steeply dipping veins.

Sb veins. Sb veins are waxy green to waxy white serpentine veins (Fig. F28A). Sb veins occur throughout the core, and frequency does not decrease with increasing depth as seen in Holes BA1B and BA3A. Sb veins have variable texture, connectivity, morphology, and so forth. In most cases, Sb veins cut other types of veins and are particularly abundant in and around magmatic intrusions where they commonly cut across dike/peridotite boundaries. They also sometimes exhibit "Frankenstein" connectivity.

Sb veins are clearly distinguishable in thin section and are commonly microcrystalline to optically isotropic with "devitrification" textures such as microcrystalline cross-fiber rims growing into amorphous vein cores and spherulites with interference crosses, as discussed further in **Microscopic characterization of veins**.

Sc veins. Sc veins are thin (typically < 0.5 mm) brown to brownish white serpentine veins (Fig. F28B). They are common in the upper levels of the cores. Like the black Sa veins, the brown veins are generally crosscut by all other vein types and are gradational with mesh veins. Many Sc veins may represent oxidized Sa veins. Near the top of the core, some could be hematite veins and/or serpentine relatively rich in Fe^{3+}, which is translucent brown to yellow in thin section. It appears that Sc veins grade into thin white veins with brown halos going downsection. These veins are not always clearly distinct from the more common, relatively young white serpentine veins (Sf), so a straightforward classification was sometimes difficult.

Sd veins. Sd veins are dark green serpentine veins (Fig. F28C). Serpentine veins in shear zones are usually classified as Sd veins. Shear veins are often steeply dipping and offset magmatic dikelets and earlier veins by a few millimeters to centimeters.

Se veins. Se veins are composite serpentine veins composed of more than one distinctly different color of serpentine (Fig. F28D).

Sf veins. Sf veins are thin (typically < 0.5 mm) white serpentine veins (Fig. F28E). They typically occur in the middle to lower levels of the cores where they are among the youngest veins present. With the increase of depth, waxy veins grade from mainly light green (above) to mainly white (below) and lose some of their waxy luster. In many cases, it becomes difficult to distinguish Sb and Sf veins in the lower third of the core where thin Sf veins become abundant near magmatic dikes. They cross dike contacts just as the Sb veins commonly do higher in the section. Additional complexity in the lowermost section is due to the appearance of white veins containing xonotlite (± serpentine); these are concentrated in and around gabbroic dikes.

Sg veins. Sg veins are bluish green (horrible green) (Fig. F28F), generally >5 mm thick, and are restricted to the lowermost level of the cores where they replace and surround highly deformed blocks of magmatic rocks.

X veins

X veins contain xonotlite, which is a translucent white mineral (Fig. F28G) with and without serpentine. They often cut contacts between gabbroic dikes and peridotite and appear similar in relative age and occurrence to Sf veins and white waxy veins (Sb), but the xonotlite veins are much harder than the Sf and Sb veins.

Other veins

White veins that are not carbonate(-bearing), serpentine, or obvious fibrous xonotlite veins were defined as "other."

Microscopic characterization of veins

The appearance and crosscutting relations of veins in the dunites, harzburgites, and magmatic dikes in Hole BA4A are very similar to those in Holes BA1B and BA3A.

Upon serpentinization, olivine and orthopyroxene in dunites and harzburgites form 10 µm–scale mesh and bastite textures that pervasively penetrate the rocks. Within this mesh, textured early serpentine (+ magnetite) is developed and clear distinction between the finest vein networks and groundmass is not always possible.

Examples of representative veins are shown in Figure F29. Similar to Holes BA1B and BA3A, the pervasive mesh network in the cores drilled in Hole BA4A is made up of serpentine and minor magnetite. Anastomosing microscopic veins with variable concentrations of magnetite in the middle cut the mesh texture. In light-colored oxidized dunites and harzburgite, these veins may be detected in macroscopic observations of the core, whereas they largely remain undetected in darker domains of the dunite sequence. These veins are generally cut by other serpentine veins that are described next.

Serpentine veins that were logged as Sb type show edge-shaped aggregates of two serpentine phases (Fig. F29A). In rare cases, microcrystalline serpentine can be observed in the middle of these veins, which occur as "turtle" networks in both gabbroic and peridotite host rocks (Fig. F29B). These veins as well as serpentine veins with overlapping serpentine (mainly lizardite) veins cut through the magnetite-bearing serpentine veins in the mesh texture (Fig. F29C).

Carbonate is observed either as monomineralic vein (logged as vein type Cb) or within composite serpentine veins (Fig. F29D, F29E).

White and grayish veins crosscutting rodingitized gabbro and pyroxenite dikes show branched or network connectivity and occasionally extend a few millimeters into host peridotite. These veins are composed of a radial needle-like aggregate of xonotlite and rarely serpentine. Xonotlite-bearing veins are observed in gabbroic dikes in the lower stratigraphy of the Hole BA4A (Fig. F29F).

Opaque minerals

Based on microscopic observations in reflected light, the opaque mineral associations include magnetite, heazlewoodite, pentlandite, chalcopyrite, bornite, and cuprite (Fig. F30). Chalcopyrite is often partially altered to bornite and chalcocite. The sulfide minerals occur mainly in the serpentine groundmass and/or in serpentine veins. Heazlewoodite and pentlandite are the most abundant sulfide minerals that form veins (Fig. F30A) and are commonly rimmed by magnetite. In rare cases, chalcocite (blue-gray) and an unidentified phase with high reflectance were replaced by bornite (Fig. F30B). In some highly serpentinized peridotites, sulfides are finely dispersed in the serpentine groundmass and could not be determined microscopically.

Magnetite occurs in most samples as intergrowths with heazlewoodite and pentlandite but also as fine-grained veins cutting the mesh texture (Fig. F30C). Chromite was altered to ferritchromite in the mesh texture and/or within serpentine veins (Fig. F30D).

XRD results for vein samples

Thirty-one XRD analyses of vein material from Hole BA4A were performed using a PANalytical CubiX³ X-ray diffractometer (Table T7). A compilation of all the spectra and sample locations within the core is given in **Supplementary material** > **F3_XRD data**.

The top of the hole contains white carbonate-bearing veins. Carbonates are the most abundant phases in the veins found in the uppermost 10 m (Cb veins). The veins are mainly composed of magnesite followed by dolomite and minor serpentine (Fig. F31A, F31B). At 10–50 m depth, carbonate and serpentine phases are both associated (Ca1, Ca2, and Ca3 veins). The major carbonate phases are Ca carbonates (calcite and aragonite) and dolomite (Fig. F31C, F31D).

Serpentine veins (Sa, Sb, Sd, Sf, and Se veins) represent most of the observed veins from 40 m to the bottom of the hole. Serpentine phases are the only identified minerals in the veins crosscutting the serpentinized peridotites only (Fig. F31E, F31F). Exceptions are Sample 47Z-4, 42 cm, having sulfides, and Sample 49Z-4, 14 cm, having spinel as other phases. Serpentine veins display wide peaks in some diffractograms suggesting the presence of low-crystallinity phases, in agreement with microscopic observations (Fig. F31E).

Veins that crosscut magmatic dikes (Fig. F31G, F31H) are composed of serpentine, hydrogrossular, amphibole, garnet (identified as andradite, $Ca_3Fe_2[SiO_4]_3$; Sample 94Z-4, 18 cm), and hydrotalcite, a hydroxide ($Mg_6Al_2CO_3[OH]_{16}{\cdot}4[H_2O]$; Sample 9Z-1, 41 cm). The gabbroic dikes sometimes display intense mechanical and chemical mixing with the peridotite. In these zones, veins are difficult to distinguish from the magmatic features. XRD reveals that these domains contain chlorite, hydrogrossular, and serpentine in addition to phlogopite, wollastonite, and clinopyroxene (Fig. F31I, F31J). High phlogopite concentration imparts a reddish color to the veins (Fig. F31J).

White veins that crosscut the magmatic dikes (X type) can be unambiguously identified as xonotlite ($Ca_6Si_6O_{17}[OH]_2$) by XRD. Xonotlite veins also often contain serpentine (Fig. F31K, F31L).

Vein abundance, distribution, and crosscutting relations

In total, 2111 veins were recorded from 303 m of core (Fig. F32). Of these, 103 were veinlets of magmatic origin that were too narrow to be logged by the background description team. Thirty veins were classified "other" because the vein-forming mineral could not be identified. Of the remaining 1978 veins, 66 (3.34%) were carbonate bearing, and 27 (1.37%) were classified as xonolite veins. The largest vein group (95.3%) are serpentine veins, of which composite serpentine veins and fibrous white veins are the most common types (both roughly 25%), and waxy green veins are also abundant (19.5%). About 5% of the serpentine veins were mixed types that could not be clearly binned in one of the six categories of serpentine veins.

Obvious veins that were logged during the core descriptions make up highly variable proportions of the core from <1% to >10% of the apparent vein area. There is no systematic downhole trend, but the boxcar-filtered data show intercalations of domains (ten to tens of meters in size) of higher and lower vein abundance (Fig. F33).

Based on crosscutting relationships, most of the youngest veins are calcite bearing. Many of the carbonate-bearing veins are composite with serpentine; others are ~100% calcite or represent a mix of carbonates (see **XRD results for vein samples**). In the upper 75 m of the hole, carbonate-bearing veins make up 13% of the veins logged and ~0.8 vol% of the core in this interval.

Carbonate veins decrease in frequency and proportion downhole (Fig. F33). Like in the previous holes of Leg 4, this decrease is unrelated to changes in host lithology.

Based on crosscutting relationships of vein types (Fig. F34), carbonate-bearing Ca and Cb type veins cut all types of veins, which shows that carbonate-bearing veins are the youngest. Contrary to this, Sa type veins are cut by all types of veins except for another Sa type vein; therefore, Sa type veins are the oldest. Sb type veins are cut by carbonate-bearing veins and a younger generation of Sb type veins, but they cut all other types of veins. Therefore, Sb type veins are relatively younger among observed veins. Sd, Se, and Sf type veins cut other types of veins or are cut by other types of veins, depending on the counterparts. Se and Sf type veins plot on the upper right corner of the diagram in Figure F34, which means that these two types of veins are particularly common in crosscutting relations with other types of veins.

White and green or gray serpentine veins with a waxy appearance are concentrated near magmatic dikes where they cut dike/peridotite contacts. Their orientation is typically normal to the dikes' margins.

In the deeper sections of Hole BA4A, xonolite veins appear in notable abundance. These veins are also tied to gabbroic dikes, although they sometimes cross the contacts into peridotite. Xonotlite has also been observed in white serpentine veins, and may hence form under similar conditions as chrysotile in the Sf veins.

Comparison with vein distributions in Holes BA1B and BA3A

All three holes share the following characteristics in vein distribution:

- Abundant carbonate veining is restricted to topmost few tens of meters of basement;
- Serpentine veins are the most abundant vein types, both in terms of volume and frequency of veining;
- The general sequence of veining is similar in all holes: early serpentine-magnetite veins are cut by later serpentine veins; carbonate veins are youngest;
- Xonotlite veins are related to gabbroic intrusions and are developed chiefly in the lowermost sections of the holes; and
- Prehnite is rare, but hydrogrossular is abundant in the metagabbros of all three holes and is associated with chlorite and serpentine in veins.

The following differences could be noted:

- Carbonate is more abundant in Hole BA1B than in both Holes BA3A and BA4A;
- Magnesite was only documented in Hole BA4A; and
- Holes BA4A and BA3A show overall uniform vein abundance throughout, whereas Hole BA1B shows a marked drop in vein abundance deeper than 200 m.

Discussion

Veining in Hole BA4A occurred throughout prolonged intervals of time and under varying pressure-temperature conditions. Waxy green serpentine veins and white serpentine veins are relatively young. This young age is in part deduced from the fact that these veins are transgranular (i.e., they cut pyroxene and spinel crystals). They have hence formed when the serpentinized peridotites behaved rigidly, which is expected to occur at low temperatures. In contrast, the Sd and Sa type veins are commonly paragranular, meaning that they flow around larger unserpentinized crystals and exploit the mechanically weak serpentinized matrix.

The veins in Hole BA4A preserve a rich record of fluid-rock interactions and associated mass transfers. As expected from the compositions of the hyperalka-

line groundwater in the Oman ophiolite, Ca^{2+} is obviously mobile and is trapped in veins only in Ca carbonate veins that form close to the surface where atmospheric CO_2 can penetrate into the basement. Calcium mobility is then restricted again at greater depth, where Ca silicates such as xonotlite and wollastonite form. Silica activities of the fluids are apparently very low, which we can deduce from the observed rodingite-like assemblages such as chlorite-hydrogrossular in veins. The presence of brucite could not be confirmed in veins, however. Because XRD results on bulk rock powders of dunite samples do show brucite but all the diffractograms for the veins do not, it appears likely that brucite is indeed absent from the vein assemblages. The abundance of serpentine in veins suggests that Mg mobility was also quite limited. Although some of the veins show halos that may have more or less magnetite, Fe mobility was also generally quite low. Overall, the veins do not indicate major mass transfers by fluid-induced metasomatism. Much rather, the veins represent fracture networks that allowed water to penetrate into the basement where the chemical potential difference between different lithologies drove reactions and mass transfers that were mediated by the presence of a fluid phase.

Structural geology

Hole BA4A represents a dunite-dominated vertical section in the mantle sequence of the Wadi Tayin Massif (Samail ophiolite) that yielded 302.75 m of core. We present the results from core descriptions and thin section observations performed on board *Chikyu* and based on a structural scheme defined and detailed in **Structural geology** in the **Methods** chapter. In the following sections we report macro- and microstructural observations and measurements of magmatic structures and brittle and plastic deformation features. All dips are measured relative to the core reference frame (CRF); consequently, the measurements are reported in a reference frame that is rotated ~30° compared to the mantle reference frame of the Oman ophiolite. All the apparent dips of magmatic contacts, peridotite foliation, veins (magmatic and alteration), fractures, and faults have been measured when possible and plotted.

Lithologic contacts

Hole BA4A is dominated by extensively serpentinized dunite crosscut by numerous dikes or magmatic veins of pyroxenite, gabbro, wehrlite, and partially to completely rodingitized gabbroic rocks (Fig. **F35**). We measured 390 primary magmatic contacts between gabbro dikes and host peridotite, 64 contacts between dunite and harzburgite, 84 contacts between pyroxenite dikes and dunite, and 25 contacts between wehrlite and dunite. The magmatic boundaries vary from sharp to transitional and from straight to irregular; the true dip angle of the contacts, including the dunite/harzburgite boundary, is mostly discordant to the granoblastic fabric of the peridotite. Magmatic contacts are often characterized by alteration halos and are crosscut by veins or reworked as tectonic contacts. Throughout the core, dikes and veins are typically partially to completely serpentinized or rodingitized.

Harzburgite/dunite contacts

Contacts between dunite and harzburgite layers are dispersed throughout the section. Harzburgite is the dominant lithology deeper than ~245 m. Contacts between harzburgite and dunite sections are often irregular and gradational with the gradation occurring over ~1–4 cm. Gradational contacts are often curved and difficult to measure. Some patches and lenses also occur with curved contacts. Most measured contacts between dunite and harzburgite show dips of 20°–60° (mean = 43.5°), which is similar to the dips for the same contacts in core from Hole BA1B (39°) and slightly higher for the corresponding dips in core from Hole BA3A (34.5°) (Figs. **F36**, **F37**).

Gabbro dikes and contacts with host peridotite

In Hole BA4A, 390 gabbro and metagabbro dikes were identified and measured by the structure description team. The intrusive contacts of gabbro dikes and dikelets (including rodingitized gabbro and olivine gabbro) are mostly sharp and planar. Figures **F36** and **F37** show the calculated dip angles and true thickness of the dikes. The dip angle ranges 10°–40°; the mean dip angle of 29.7° is significantly less than the dip for the dunite/harzburgite contacts and close to the same dips for gabbro dikes in Holes BA1B (34.6°) and BA3A (36.0°). The number of gabbro dikes in the dunite-dominated cores (Holes BA1B and BA3A) is, however, much larger (273 and 390, respectively) than in the harzburgite-dominated core (82). The thickness of the gabbro dikes in Hole BA3A ranges from millimeters to a 1.1 m thick gabbro pegmatite occurring at ~30 m depth (Fig. **F35**) with a mean value of ~6 cm. It is likely that numerous dikes thinner than a few millimeters were ignored during core logging. There is no apparent variation in thickness with depth in the core. The uppermost gabbroic dike occurs at 4.4 m depth (Section 2Z-2), and the last one occurs at 302.7 m (Section 109Z-4).

For dikes thicker than ~1 cm, the thickness distribution appears to follow an approximate power-law scaling relation (Fig. **F37**). Similar scaling behavior is observed for Hole BA1B, but in that core the distribution follows a steeper slope (higher power-law exponent). The cumulative thickness of all measured gabbro dikes in Hole BA4A is ~20 m, or ~7% of the overall core thickness.

Pyroxenite dikes

Pyroxenite dikes or dikelets (including ortho- and clinopyroxenite) occur throughout Hole BA4A and seem to be relatively evenly distributed in the dunites but are less frequent than in harzburgite-dominated Hole BA3A. The maximum thickness of the pyroxenite dikes is ~40 cm (Section 97Z-4), but the majority are <5 cm. The dip angle of most pyroxenite dikes ranges 10°–50° (mean = ~30°), similar to the dip for the gabbro dikes but significantly less steep than for the dunite/harzburgite contacts and the peridotite foliation in this core (38.5°, see below) (Figs. F36, F39).

The uppermost recovered pyroxenite dike is located at 15.9 m depth (Section 1Z-4) and is completely altered, and the deepest pyroxenite dike occurs at 295.4 m (Section 108Z-4).

Wehrlitic dikes

The orientation and thickness of 25 wehrlitic dikes were measured. Their thicknesses range 1–40 cm, and their downhole distribution is homogeneous. Dip angles vary widely and are not significantly different from the dip of the dunite/harzburgite boundaries (Fig. F36). The uppermost recovered dike is at 2.2 m depth, and the deepest occurs at 299.0 m (Section 107Z-2).

Deformation features

Peridotite fabric

In Hole BA4A the relatively high degree of alteration present in the dunite makes the recognition of crystal-plastic deformation difficult at the macroscopic scale. The deformation recorded in the harzburgite units is easier to characterize than in the dunite, using the elongation of orthopyroxene and the preferred orientation of spinel grains. Crystal-plastic fabric is defined by the geometry of pyroxene porphyroblasts, and the harzburgites commonly exhibit strongly foliated to protomylonitic texture (Fig. F38). In some intervals, orthopyroxene pseudomorphs show subrounded shape or form aggregates affected by the intense serpentinization, making it difficult to discern their original fabric. The dip of 208 measured peridotite foliations ranges 10°–50° (average = 31.2°), slightly less steep than the dip of the dunite/harzburgite contacts (43.5°). This is similar to the dip of the peridotite foliation in Hole BA3A (31.1°) but significantly steeper than the harzburgite-dominated Hole BA3A (12.6°) (Fig. F39). The dips do not show any significant variation with depth.

Crystal-plastic deformation in harzburgites

The relatively high degree of alteration present in the harzburgites makes the recognition of crystal-plastic deformation difficult. In Hole BA4A, a crystal-plastic fabric is defined by elongation of pyroxenes. Harzburgites in Hole BA4A show protogranular to porphyroclastic texture at shallower depths (e.g., Sections 21Z-4 through 23Z-3; 46.9–52.8 m) and strongly foliated to protomylonitic texture deeper (e.g., Sections 97Z-1 through 97Z-4; 263.8–266.9 m). Most dip angles of elongated pyroxenes are within 30°–40°. The harzburgite-dominated interval at 8.2–21.8 m (Sections 4Z-3 through 9Z-2) shows porphyroclastic texture defined by rounded and slightly elongated pyroxenes and often strongly foliated texture exhibited by moderately elongated and aligned pyroxenes, especially in the shallower part (e.g., Sections 4Z-3 through 5Z-1; 8.2–9.6 m). The harzburgite interval at 40.1–82.1 m (Sections 19Z-3 through 33Z-2) shows protogranular to porphyroclastic texture and partly strongly foliated texture (e.g., Section 31Z-1; 74.7–75.2 m). In the interval 85.2–126.4 m (Sections 34Z-2 through 48Z-1), harzburgites are weakly foliated and exhibit mainly prophyroclastic texture by slightly elongated pyroxene (Fig. F38; Sample 38Z-4, 69–71 cm). Harzburgites in the interval 129.7–172.0 m (Sections 49Z-2 through 63Z-2) exhibit porphyroclastic to strongly foliated texture due to slightly to moderately elongated pyroxenes. Figure F38 (Sample 53Z-1, 14–16 cm) shows strongly foliated harzburgite. In the interval 176.7–202.1 m (Sections 65Z-1 through 75Z-2), the harzburgites show porphyroclastic to strongly foliated texture defined by slightly to moderately elongated pyroxene. Harzburgites in the interval 221.9–263.5 m (Sections 83Z-1 through 96Z-4) show porphyrpclastic to strongly foliated texture by alignment of slightly to moderately elongated pyroxene. In the interval 263.8–302.8 m (Sections 97Z-1 through 109Z-4), harzburgites show porphyroclastic to protomylonitic texture with slightly to strongly elongated pyroxenes.

A spectacular example of the transition from crystal-plastic to brittle deformation can locally be observed where a partly chloritized clinopyroxene has been indented by a relatively fresh clinopyroxene. The unaltered indentor grain bends the chlorite-filled cleavage planes of the partly chloritized one until crystal-plastic deformation, reflected by undulatory extinction, yields to a fault-like zone of highly localized deformation. The indentor grain itself appears to have developed some subgrain formation and rotation near the interface at which the grains converge (Fig. F40).

Brittle deformation

Hole BA4A shows extensive brittle deformation and vein formation throughout the length of the core. Apart from a reduction in fracture density from the upper few meters of physical weathering, there is no systematic variation in fracture-vein density with depth (Fig. F41). Nearly all gabbro dikes are exten-

sively fractured and crosscut by a variety of veins (Fig. F42), as are the immediate wall rocks. Thick gabbro dikes, however, including the 1.1 m thick gabbro pegmatite at ~30 m depth and the 5 m thick layer of magmatic impregnation breccia near 210 m depth, seem to protect the underlying 10 m or so of peridotite from fracturing and vein formation. The dunite-dominated core from Hole BA4A is significantly more fractured and veined than the harzburgite-dominated Hole BA3A (see **Structural geology** in the **Site BA3** chapter). This is also reflected in a generally lower density and higher porosity (see **Physical properties**). In the following, we report data from different categories of brittle deformation features.

Cataclastic veins

The first stage of brittle deformation recognizable in the peridotite cores is dark veins often filled with angular clasts set in a very fine grained "pseudotachylite-like" matrix. These veins are easier to observe in the harzburgites than in the dunites, possibly due to the uniformly dark color of the serpentinized dunites. In Section 54Z-1, one of these veins runs through the entire 90 cm long section while cutting through and faulting four gabbro/pyroxenite veins on its way (Fig. F43). The maximum apparent displacement is ~5 cm, and the vein occasionally branches into a small number of "subveins." These veins are usually no more than 1 or 2 mm in width but when branching into subvein networks can produce damage zones several centimeters wide. Further examples of these early, high intensity brittle deformation features occur at 216.5 and 272.8 m. However, it is believed that such structures are probably far more common throughout the core but are very difficult to distinguish when they do not displace dikes or other structures.

Fault zones

Fault zones occur throughout Hole BA4A with the exception of the interval 68–129 m where only one is recorded, but they vary extensively in thickness, intensity, and structure. Fault zones range from 1 mm wide individual fractures with observable apparent offset to decimeter-scale zones of intense fracturing and cataclasis (Fig. F42). They were differentiated from cataclastic zones, which were ostensibly very similar, by the presence of some evidence for slip or displacement such as facoids, slickensides, or a strong planar fabric. Figure F41 displays the locations of fault zones alongside a lithologic log of Hole BA4A and shows an apparent correlation between the positions of fault zones and the occurrence of harzburgitic sections in the sequence. It is possible that brittle deformation may have become concentrated at these localities due to increased heterogeneity at multiple scales from intercalated lithologic units to varying degrees of serpentinization and greater quantities of pyroxene among the serpentinized olivine mesh of the peridotites. There is a slight increase in the dip angle of fault zones with depth in Hole BA4A, dipping on average more steeply than most other recorded types of deformation structure throughout the core (Fig. F44).

Unlike in Hole BA1B, no major meter-scale fault zone was recovered in Hole BA4A, which is informative because the Hole BA1B and BA4A drill sites are located <500 m apart. The 3 m wide fault zone described in Hole BA1B is at 160 m depth, dips at 53°, and marks the boundary between a dominantly dunitic sequence above and a mostly harzburgitic sequence below. The fact that Hole BA4A is mainly dunitic in composition and that this major fault is not encountered may suggest that Hole BA4A correlates with the upper part of Hole BA1B and that the fault dips roughly northwest, underlying the entire sequence of Hole BA4A. This is highly speculative, however, and thorough orientation of the cores is required before cross-core correlation and the true orientation of the major fault zone can be determined.

Shear veins

Shear veins were recovered throughout Hole BA4A and, with 204 recorded and measured, are the most commonly observed type of deformation feature. The morphology of shear veins varies considerably with several different forms and types; the attribute common to all is a mineralized fracture along which some degree of displacement or shear has been accommodated. In this way they were distinguished from nonshear veins along which displacement had not occurred, and such veins were handled separately as alteration veins (see **Orientations of alteration veins**). Some shear veins exhibit displacement of several centimeters along a very narrow (1–2 mm) slip plane and are likely to have formed as brittle fractures subsequently filled with serpentine to form a vein. In other cases, complex composite veins exhibit Riedell type fractures and/or subordinate sheared veins and are more likely to have formed as veins first and been subsequently sheared (Fig. F42) (see **Structural geology** in the **Site BA3** chapter). In many cases, dikes or other features are offset by shear veins and the apparent displacement and shear sense was recorded. The amount of shear accommodated on these structures appears to be relatively small (mean = 1.5 cm), although it should be noted that large displacements are rarely observed in the drill core and so are absent from the data set. Despite their small offsets and relatively low intensity of deformation, the abundance of shear veins throughout the core positions them as an important mechanism by which strain is accommodated, especially in somewhat homogeneous zones where larger features such as fault zones or a high density of dikes are ab-

sent. Indeed, the only part of Hole BA4A in which shear veins become relatively rare is at ~205–220 m where the sequence is dominated by magmatic impregnation breccias.

The shear veins observed are typically steeply dipping features (mean dip angle = 55.9°) (Fig. F45) and host deformation within very narrow regions (mean width = 3.4 mm). The width of brittle damage zones around such veins is also very small or nonexistent, suggesting short-lived or incipient slip on these structures rather than prolonged activity and reactivity like with fault zones. There is little apparent trend in the dip angle of shear veins with depth.

Where open fractures occur along shear veins, their surfaces often display preferential lineations in the growth of serpentine or other vein filling minerals, which were measured when possible. The plunges of these features are mostly <40° with a small cluster of steeper plunges >50° at ~184–205 m depth (Fig. F46). Lineation plunges, when plotted against the dip angle of the plane on which they are hosted, can give an indication of the shear sense on that structure. In Hole BA4A, there appears to be slightly more shear veins exhibiting dip-slip behavior than strike-slip (Fig. F46).

Shear zones

Although not always strictly brittle in nature, shear zones were logged at the same time as purely brittle features because they are similarly discrete finite deformation structures usually with a measurable orientation. In addition, this methodology was used because of the difficulties associated with differentiating true crystal-plastic deformation from semibrittle processes or granular flow during macroscopic core observation. As a result, shear zones were logged where macroscopically ductile shear fabrics were observed, and these features may relate to semibrittle or true crystal-plastic deformation. Shear zones in Hole BA4A are strongly associated with dikes, particularly gabbros, and often are observed to follow one contact or another or to run directly through the center. Narrow shear zones at the edges of dikes suggest localization of strain along the rheological interface. However, this does not account for shear zones in the center of dikes, which may be more indicative of the relative weakness of highly altered gabbros in comparison to the peridotite host rock. Indeed, microstructural studies on thin sections of dike-hosted shear zones in Hole BA4A were often hampered by the near total alteration of the original minerals, whereas the less altered dikes are rarely observed to host shear zones. The association of shear zones with dikes is likely to be a significant factor in their typically shallow dip angles, which have a mean of 35.4° (Fig. F44). Most recovered shear zones are very narrow with a median thickness of 0.75 cm, but there are occasional notable examples of much wider shear zones. The best example is a 28 cm wide mylonite at 287 m depth (Fig. F42). This was entirely contained within altered leucocratic material, probably originally a dike of gabbroic or similar composition, and displays a fine-grained highly foliated fabric with rounded porphyroclasts increasing in abundance toward the margins. Shear zones are distributed throughout the core but with peaks in their frequency at ~140 m and deeper than 280 m.

Cataclastic zones and magmatic impregnation breccias

Cataclastic zones were logged in Hole BA4A where regions of brittle damage or brecciation were observed but displacement or faulting could not be confirmed. The distinction between cataclastic zones and fault zones was sometimes not clear, but the term cataclastic zone was used where slip or displacement in the form of fault motion could not be confirmed. Cataclastic zones are therefore applicable to in situ fracturing or cataclasis where classifying a fault zone may be inappropriate. Cataclastic zones were uncommon in Hole BA4A, with only 17 occurrences, and were recorded far less frequently than fault zones. This reflects the fact that in many cases, sharply defined planar boundaries, mineral slickenfibers, or apparent offsets of dikes or other features are evident and can be used to classify the fractured region as a fault zone. Cataclastic zones are most common in the upper 40 m of the core, and none were described deeper than 225 m. The abundance at the top of the core may be in part a result of the influence of surface-related deformation. Cataclastic zones in Hole BA4A vary in thickness (0.4–43 cm, mean = 9 cm), and their dip angle decreases slightly downhole (Fig. F44).

Magmatic impregnation breccias (MIBs) are a type of in situ cataclastic zone that may have been induced by the intrusion of magma in a somewhat distributed and chaotic manner. They were differentiated from other cataclastic zones and logged separately because of their abundance in Hole BA4A and for the clear differences in characteristics between them and regular, unintruded in situ breccias and cataclasites. MIBs typically consist of zones or bands of leucocratic and highly altered material that display flow-like structures (this may be a magmatic texture or evidence of subsolidus crystal-plastic deformation) surrounding “clasts” of peridotite host rock that are rounded to subangular and display alteration gradients inward from the “matrix” (Fig. F42). The exact mechanism of formation for these complex regions is ambiguous, but they were recorded among the brittle deformation features because the morphology of the clasts suggests some degree of stress-induced breakup of the host rock. In many cases the clasts had a weak preferred orientation that concurred with the flow fabrics of the matrix and when measured usually yielded relatively steep dip angles (Fig.

F45). A very large sequence of steeply dipping MIBs was recovered at 206–212 m depth and represents the largest and most significant deformational feature throughout the core (Fig. F41). Interestingly, immediately below this is a section of almost pristine core with very few deformation features and the lowest fracture and vein density of the entire sequence.

Joints and hydrothermal breccia veins

Joints were logged throughout the sequence of Hole BA4A, where open fractures were observed with no apparent mineral vein fill and no apparent displacement. Open fractures were not logged as joints if they were believed to have been derived from the drilling process or from fracturing during core processing. Such fractures are often normal to the core axis or form along existing planes of weakness such as dikes or veins that were measured as such by the structure description team rather than as joints. Recorded joints decrease in abundance downhole because deeper cores are often more intact or, where fractures did exist, they commonly related directly to veins, fault zones, or other structures. The dip angle of joints increases downhole and has a mean of 50.9° (Fig. F44). Hydrothermal breccia veins were recorded where a vein contained angular lithic fragments forming a mineralized breccia of the wall rock. Hydrothermal breccia veins were only recorded in the upper 20 m of the borehole and were typically shallow-dipping features.

Orientations of alteration veins

In Hole BA4A, we measured 57 carbonate or carbonate-bearing veins, 1119 serpentine veins, 88 magmatic veins (<5 mm apparent thickness), and 29 other, not well identified veins, among which we identified 11 xonotlite veins. Individual veins, vein sets, and vein networks were defined and grouped into carbonate-serpentine veins (type Ca), carbonate veins (Cb), xonotlite veins (X), and different serpentine vein generations based on their color and texture (types Sa, Sb, Sc, Sd, Se, and Sf) by the vein alteration description team during macroscopic visual core description (see **Macroscopic identification of vein types**). The vein type classification is the same as for Holes BA1B and BA3A, but more veins seem to have been defined as composite veins (Se) than in the previous holes. Crosscutting relationships are similar to those in Holes BA1B and BA3A with high ambiguity in apparent age relations between different vein generations apart from a clear distinction between the earliest black serpentine veins (Sa) and the youngest waxy green serpentine (Sb) and carbonate(-bearing) vein generations. Composite vein generations (Se) often show reopening or exploitation of previous serpentine vein generations by younger serpentine and carbonate veins. Orientation measurements are given in the same data set as used by the vein alteration description team as true dip and apparent dip azimuth in the CRF. Dip azimuths and true dips of vertical and subvertical veins could rarely be measured accurately but were included for statistical analysis of dip angles using generic dip azimuth/dip values (0°/89.9° and 0°/85°). In intervals with high vein densities, measurements were limited to orientations of single veins and representative orientations in systematic vein sets. For conjugate vein sets of the same vein type, we measured two or three predominant orientations, where well defined, and identified them as conjugate in the data set. Chaotic, strongly branching, or anastomosing vein networks, polygonal networks (e.g "tortoise"-textured; see **Structural geology** in the **Methods** chapter), and veins that do not crosscut the core surfaces (e.g., small ladder crack/Frankenstein vein sets of type Sb; see **Structural geology** in the **Methods** chapter) were not measured.

Variations in dip angles of carbonate(-bearing) veins and different serpentine vein types with depth are shown in Figure F47, together with overall rose diagrams of their dip distributions. Carbonate (Cb) and carbonate-serpentine (Ca) veins are relatively common in the uppermost 60 m of Hole BA4A. Special care has been taken to document the orientations of all identified carbonate(-bearing) veins and vein sets, where measurable. More than half of the measured carbonate veins (Cb) in the levels close to the surface (0–10 m) have dip angles <30° (Fig. F47); on average this vein type dips 34°. This reflects their formation close to the current erosion surface. Hence, these represent the youngest vein generation. Carbonate-serpentine veins (type Ca) are substantially steeper on average (mean dip = 54°), similar to the orientations of most serpentine vein types. Deeper than 10 m depth, there are no carbonate(-bearing) veins with dips <30°. With depth, dip angles of carbonate-serpentine veins become similar to those of serpentine veins, suggesting that carbonate precipitation may have occurred along previously existing and reactivated serpentine veins. All serpentine vein types show a high variability in dip angles, mostly scattering between 30° and 90° (Fig. F47). No major differences in dip angles are apparent between measured Sa, Sb, Sd, Se, and Sf serpentine veins. Black Sa and white Sf veins show a somewhat higher abundance of veins with dips of 20°–40° than the other serpentine vein types. In case of white Sf veins (Fig. F47), this is likely due to the common occurrence of conjugate sets where one set is dipping relatively shallowly. Clear conjugate sets of Sf serpentine veins were observed in 60 occurrences throughout Hole BA4A; similar observations were much rarer for the other serpentine vein types. In the interval 80–40 m, measured alteration veins with dips <45° are significantly less abundant than in the intervals above and below (Fig. F47). This interval corresponds to a do-

main where only few fault zones have been observed as opposed to higher deformation intensities above and below. The orientations of alteration veins in Holes BA1B and BA3A show a similar correlation, suggesting that there may be a link between relatively shallow serpentine vein orientations and deformation intensity.

Geochemistry

Whole-rock geochemistry was determined on 72 samples from Hole BA4A: 30 sampled on site at regular intervals of 10 m and 42 sampled aboard *Chikyu* during core logging (Table T9). Sample lithologies encompass 32 harzburgites, 23 dunites, and 17 gabbros. On site samples were powdered at the University of Southampton. Shipboard samples were crushed and powdered on board. Both sets of powders were analyzed on board for major, trace, and volatile elements and for mineralogy by XRD (see **Geochemistry** in the **Methods** chapter for full analytical procedures).

Hole BA4A consists of harzburgites, dunites, and gabbros with rare pyroxenite dikes and veins. Compared to the thick dunite and harzburgite sequences in Hole BA1B and the predominance of harzburgite in Hole BA3A, it shows a more finely interlayered lithostratigraphy. Dikes of dunite and gabbro are ubiquitous throughout the hole. Key questions include the petrogenesis of these gabbros, their relationship to crustal gabbro sequences sampled elsewhere, and the timing of their emplacement relative to hydration of the surrounding peridotite. A summary of key geochemical parameters for each of the lithologies, together with comparative data from Holes BA1B and BA3A, is presented in Table T8.

LOI and volatile contents

There is little variation in loss on ignition (LOI) with depth downhole (Fig. F48A). The first-order variation is between lithologies, with gabbros having lowest values (mean = 8.1%), harzburgites intermediate (mean = 12.5%), and dunites showing the highest values (mean = 14.8%). A very similar trend with lithology is seen in Holes BA1B and BA3A (see Table T8).

Comparison of LOI contents with H_2O content determined by elemental analyzer (EA) shows a close 1:1 relationship (Fig. F49A) indicating that water content is the primary control on LOI in all three holes. By contrast, CO_2 contents are low in all samples (0–0.8 wt%) and uncorrelated with LOI (Fig. F49B). There is a slight but consistent offset of the data to higher H_2O values for a given LOI, indicating either that LOI is underestimated or that H_2O is overestimated. LOI underestimation can result from the weight gain associated with oxidation of Fe(II) to Fe(III) during ignition of powders. Assuming all Fe is present as Fe(II), a correction can be calculated as

$$Fe(III)_{LOI} = Fe(II)O - Fe(II)O/1.11, \quad (1)$$

representing the greatest possible magnitude of this effect. Adding this $Fe(III)_{LOI}$ to measured LOI and including the small contribution from CO_2 gives a better fit to the 1:1 line (Fig. F49C). The only exception is a small deviation in the dunites from Hole BA1B (mostly from shallow depths) at high LOI, suggesting these may have slightly higher initial Fe(III) contents.

Given this strong relationship, the variation in LOI between lithologies can be linked to variation in the degree of hydration. This interpretation is consistent with the petrology of the samples. Harzburgite commonly shows relict olivine cores and orthopyroxenes in the serpentine mesh texture, whereas dunites are almost always completely serpentinized. Most harzburgites have LOI as high as 13%, corresponding to the water content of pure serpentine. The extension of dunites (and a few harzburgites) to higher values requires the presence of a more water-rich mineral. Brucite ($Mg[OH]_2$, H_2O = 30.89 wt%) is commonly formed during serpentinization at low silica activity and was detected by XRD in 27 samples across the 3 holes (see **Supplementary material** > **F3_XRD data**). The majority (21) of these are dunites with high LOI (mean = 15.2%), suggesting brucite is the main contributor to their elevated LOI. The remaining samples are harzburgites that show LOI only slightly higher than the overall mean for harzburgites (12.9%, cf. 12.5%).

CO_2, though low, is nevertheless elevated with respect to normal mantle peridotites (~300 pm, 0.03%) indicating minor carbonation has affected the rocks (Fig. F48). CO_2 greater than ~0.4% is restricted to the upper 100 m and decreases downhole in all cores, suggesting some CO_2 is derived from surface processes. This mirrors the pattern seen in the distribution of carbonate veins downhole (see **Veins**, e.g., Fig. F33). With the exception of these higher CO_2 samples, the majority of the data in all holes cluster around CO_2 ~0.2% with little variation downhole.

Filtering the data for CO_2 <0.4% to exclude samples likely affected by carbonate veining gives a mean CO_2 content of 0.21%, suggesting minor carbonation of the background rock has also taken place. It might be expected that carbonation would be promoted by higher CaO contents due to the more favorable kinetics of calcite crystallization (cf. magnesite, dolomite); however, there is no relationship between CO_2 and CaO, and neither is carbonation more pronounced in harzburgite compared to dunite.

Total carbon (TC) vs. inorganic carbon (IC) shows a strong 1:1 relationship giving an independent check on the validity of the CO_2 data (Fig. F49D). There is a slight but systematic offset (~0.01 wt%) to lower IC for a given TC. This may be caused by the presence of small (<0.2 wt%) amounts of magnesite ($MgCO_3$), which can resist acid digestion during IC analysis. Magnesite was detected in 5 samples from Hole BA4A and corresponds to 2 samples with low IC where there are volatile data available. Alternatively, the data may reflect a slight bias between the two analytical methods. Nonetheless, the good agreement of the two data sets indicates that the slight CO_2 enrichments seen in the peridotites is robust and not an analytical artifact. For comparison, calculated mean CO_2 contents from TC and IC (filtered for CO_2 <0.4%) are 0.21% and 0.23%, respectively.

Whole-rock major and minor elements

Major element chemistry largely reflects the sample lithologies in Hole BA4A, with gabbros, dunites and harzburgites all geochemically distinguishable (Table T9). Within each lithology there is little in the way of downhole variation and peridotites (harzburgites and dunites) plot in a tight array within the range of typical Oman mantle for Mg#, TiO_2 and Ni. Cr contents are more variable and likely reflect variation in chrome spinel content from sample to sample. In detail, dunites have slightly lower Mg# than harzburgites (~89.6 cf. 90.7) and have lower Cr contents. Gabbros are much more variable in their composition but also lack any trend with depth in the core. They have lower Mg# and Ni (reflecting differentiation and lower olivine content), higher TiO_2, and variable Cr, which overlaps the range of peridotite compositions. In the following summary and discussion of the major element geochemistry the samples are addressed on the basis of lithology.

Peridotites

Figure F50 shows key elements plotted against Al_2O_3, a proxy for peridotite fertility. Classic peridotite differentiation and depletion trends are shown by literature data for uninfiltrated Oman peridotites that progress from high-Al, fertile lherzolites through harzburgites to low-Al dunites.

Harzburgites

Harzburgites from Hole BA4A plot on these trends and largely cluster in the range 0.5%–1.0% Al_2O_3, toward the more depleted end of the harzburgite array. Ni is toward the upper end of the range of Oman mantle compositions, consistent with the relatively refractory composition of the harzburgites. A few samples (e.g., 89Z-4, 40.0–46.0 cm, 95Z-1, 25.0–30.0 cm, and 19Z-4, 66–71 cm) show more enriched signatures, with Al_2O_3 of 1.2–1.5, elevated SiO_2, CaO, and TiO_2, and modal clinopyroxene (<4%) identified in thin section. This might be a result of lower degrees of melt depletion or more likely is due to infiltration by small volumes of melt. One sample (95Z-3, 38.0–43.0 cm) contained numerous small inclusions of gabbro and is the most enriched, causing it to plot as an outlier from the bulk of the harzburgite data.

Dunites

Dunites show some overlap with the array defined by the peridotites, but most plot in a distinct cluster at lower Al_2O_3, CaO, SiO_2, Cr, and higher Fe_2O_3, reflecting their lower modal orthopyroxene, clinopyroxene, and chromite compared to harzburgites. Three samples show elevated Al_2O_3 for their Fe_2O_3 and CaO contents (Fig. F50C, F50D) and plot toward the field of infiltrated Oman peridotites (e.g., Maqsad diapir), suggestive of minor melt infiltration. Dunite Ni contents show a slight decrease with decreasing Mg#, which could be indicative of formation by melt-rock interaction (Fig. F51). Two dunite samples (19Z-4, 66.0–71.0 cm, and 66Z-4, 34.0–39.0 cm) show clear petrological and geochemical evidence of melt refertilization with high Fe_2O_3 contents and low Ni, Mg#, and Al_2O_3 together with modal orthopyroxene and clinopyroxene.

Gabbros

By any geochemical criteria, the gabbros are the lithology that shows the greatest variability in Hole BA4A (and across all 3 BA cored holes). Data from lower crustal gabbros recovered from Holes GT1 and GT2 (Oman Drilling Project Leg 2), and Holes CM1 and CM2 (Leg 3) are presented in the accompanying figures for comparison. A very general feature of these plots is that the gabbros in Hole BA4A have markedly different chemistry from the crustal gabbros and often plot to compositions intermediate between these and the Hole BA4A host peridotites (Fig. F52). The gabbros are quite primitive, with Mg# 80.6–91.6 and SiO_2 generally <45%. They show marked variability, with ranges of MgO, CaO, Al_2O_3, and TiO_2 larger than those of the entire GT and CM data sets. With the exception of a weak negative correlation between Al_2O_3 and SO_2 (likely controlled by feldspar crystallization), they exhibit none of the major element correlations typical of fractional crystallization. Overall it is difficult to explain the geochemical variability observed by magmatic differentiation processes.

Alternative explanations include alteration and metasomatism or melt rock interaction. The gabbros are in general quite altered and in some cases rodingitised. This has likely contributed to some of the variability seen. However, gabbros from Hole GT1 and GT2 do not show the same degree of variability

despite being pervasively altered. Rodingitisation, which does not affect the GT cores, may contribute to the signatures seen in BA4A. The growth of calcium-bearing phases in veins, the extension of these veins out into the host rock, and the formation of serpentine within the gabbros in locations other than after olivine suggests metasomatic redistribution of calcium and magnesium on the mm to cm scale. LOI shows a weak negative correlation with SiO_2, CaO, and Fe_2O_3 and positive correlation with MgO. However this is best explained by variations in the modal content of olivine prior to hydration rather than degree of alteration controlling the major element chemistry. In particular, there is no increase in chemical variability with degree of alteration (i.e., LOI) suggesting the major element variation is likely to be a primary magmatic feature.

A possible explanation for the signatures observed is interaction of the gabbro parental melts with their host peridotites during their passage through the mantle. This is supported by their intermediate compositions between peridotites and more typical gabbros (e.g., Fig. **F53**). The constant Ca# of the gabbros over a range of Mg# lends weight to this (Fig. **F54**). This is very distinct from the correlated Mg#–Ca# differentiation trend defined by lower crustal gabbros suggesting either that Ca is externally buffered during differentiation (e.g., by scavenging of clinopyroxene), or that variation in Mg# is the result of interaction between wall rock peridotites and very primitive melts with initial Mg# of ~90.

Further on-shore investigations are necessary to identify the origin of the distinct compositions of the gabbros sampled at Holes BA1B, BA3A, and BA4A.

Comparison to Holes BA1B and BA3A

In general the three holes show very consistent geochemical signatures with the three broad lithological groups defining the same arrays or clusters on most plots.

The peridotites from Hole BA4A are the most restricted in their compositional range. There appears to be a greater proportion of "fertile" peridotites in Hole BA1B which has 12 samples with Al_2O_3 >1%, compared to 4 from each of Hole BA3A and BA4A. With these exceptions however, the combined data set suggests that broadly the same trends (and likely processes) apply to all three holes.

Dunites from Hole BA1B in particular are more variable and show the strongest indications of melt-rock interaction. They show a correlation between Ni and Mg# indicating coupled Fe enrichment and incompatible behavior of Ni in olivine during reaction with relatively Mg-poor, Fe-rich basaltic melts (Fig. **F51** inset). This trend is extended by the gabbros from Holes BA4A and BA1B, which plot intermediate between peridotites and lower crustal gabbros. Markedly similar trends have previously been described in olivine-rich troctolites from the Atlantis Massif and ascribed to melt-rock interaction (Godard et al. 2009). Similarly, gabbros from all three BA holes fill a compositional gap in MgO-FeO space and show enrichment of FeO unrelated to MgO depletion, consistent with variable equilibration between peridotites and basaltic melts parental to the gabbros.

The gabbros from Hole BA1B and BA4A are very similar, spanning the same wide ranges in all elements. Whereas Hole BA3A consisted almost entirely of harzburgites, the two gabbros sampled are consistent with these. Rather than reinforcing any sense of covariation as in the peridotites, comparing the three holes instead emphasizes the discoordination of the data. The consistency of this inconsistency implies, again, that similar processes are responsible for the genesis of the signatures in all three holes.

Trace elements

Six gabbros and five peridotites from across the 3 holes were selected and analyzed for whole-rock trace elements by laser ablation–inductively coupled plasma–mass spectrometry (LA-ICP-MS) on pressed powder pellets (Table **T10**). See **Geochemistry** in the **Methods** chapter for the full analytical procedure.

Normalized rare earth element (REE) patterns (Fig. **F55**) show low REE abundance and relative depletion of the light REE (LREE) in the gabbros resulting in a concave down profile typical of melting a depleted source. All but one show positive Eu anomalies, consistent with accumulation of plagioclase. One gabbro sample (112Z-3, 90.0–95.0 cm) is slightly more enriched and shows REE and trace element profiles more typical of basaltic melts. As in their major element chemistry, the trace element patterns of BA gabbros resemble the olivine-rich troctolites of Godard et al. (2009), see above. The flat pattern in one sample, a hybrid harzburgite cut by a gabbro dike, is interesting, suggesting interaction between the two lithologies may have resulted in slight LREE refertilization.

The analytical challenges posed by the low abundance of REE in peridotites results in much less well defined profiles. However, it is possible to discern a clear depletion in LREE in these too with a broad upwards sloping profile from La to Lu. This, together with their low overall trace element abundance, is quite consistent with their depleted major element composition (e.g., Fig. **F50**). Taken together, the peridotite profiles appear to perhaps flatten toward the LREE and even define a slight convex up profile; however, the scatter of the data is such that no firm observation can be made.

The normalized trace element profiles (Fig. **F55**) are fairly consistent within each lithology. Positive U

and Pb anomalies seen in the harzburgites are common features in abyssal peridotites and likely relate to mobile behavior in aqueous fluids. It is intriguing that these anomalies are mirrored in the gabbros, though the reasons for this are unclear at present.

Summary

Geochemical analyses of major, trace, and volatile elements were conducted on 70 samples taken from Hole BA4A, drilled as part of the Oman Drilling Project and analyzed aboard *Chikyu*. These consist of 36 harzburgites, 20 dunites, and 14 gabbros. LOI was relatively consistent within each lithology but varied between dunites (mean = ~14%), harzburgites (~12.5%), and gabbros (~8%). H_2O contents show a strong 1:1 correlation with LOI, indicating it is degree of hydration that controls this. CO_2 contents were low but significantly above normal mantle concentrations. Some samples in the upper 100 m of the hole show values <1% that decrease steadily downhole and are likely the result of shallow carbonated veins. Even with these samples excluded, CO_2 is consistently elevated downhole and averages 0.21%, suggesting that minor carbonation of the groundmass has taken place. Harzburgites show a restricted range in major and trace element composition toward the depleted end of the array of Oman peridotites. Dunite compositions are also consistent with existing data and show minor evidence for melt rock interaction with correlated Ni and Mg#. Gabbros are primitive (Mg# 81–92) and show compositions intermediate between peridotites and Oman lower crustal gabbros. There is pronounced variation in all major element abundances and a complete lack of differentiation trends with varying SiO_2 (37–49 wt%). Together these features are interpreted as most likely due to the result of interaction with wall-rock peridotites during emplacement of the dikes though the influence of alteration processes cannot be ruled out. Data from Hole BA4A are very consistent with those from Holes BA1B and BA3A with similar signatures and variations seen in each lithologic group from all three holes. This suggests that the underlying processes controlling the geochemistry are common to all three locations.

Microbiology

Phase 2 microbiology results are reported in **Microbiology** in the **Site BA1** chapter.

Paleomagnetism

Remanent magnetizations

Magnetic remanence measurements were made at the University of Iceland in 2019 on discrete sample cubes taken from the working half cores from Hole BA4A. A total of 95 discrete samples were measured, of which approximately one-third (31 samples) were thermally demagnetized and all others were subjected to stepwise alternating field (AF) demagnetization in tumbling mode to isolate the characteristic remanent magnetization (ChRM) direction. Some irregularly shaped and broken samples were omitted from measurements.

Natural remanent magnetization (NRM) intensity values range 0.024–4.4 A/m (geometric mean = 0.22 A/m) (Table **T11**; Fig. **F56**). NRM magnitudes vary throughout the hole, although higher-than-average values are slightly more common in the upper half of the hole. NRM orientations have predominantly low-angle negative inclinations that trend toward slightly more shallow angles with depth (Fig. **F57**). Principal component analysis of demagnetization data was used to identify remanence vector components.

A stable ChRM that trends to the origin at the highest field and temperature steps was identified in nearly all samples. ChRM orientations are generally very similar to those of the NRM. ChRM orientations have a mean inclination of –28.9° (k = 28, $\alpha 95$ = 2.9°, n = 89) calculated using the Arason and Levi (2010) maximum likelihood method (Table **T12**). The direction of the ChRM vectors determined by thermal demagnetization and AF demagnetization are very similar, indicating that both demagnetization methods isolated the same remanence component.

An additional component with lower coercivity or unblocking temperatures and a distinct orientation from the ChRM was isolated in 69 samples, here termed the "soft" component (Figs. **F58**, **F59**). The soft component magnitudes generally make up a small proportion of the NRM. The soft components have positive inclinations in nearly all samples (mean inclination = 49.1°). A small proportion of samples contained only a single remanence component. Occasionally, the soft component orientation is antiparallel to that of the ChRM (Fig. **F59A**).

AF demagnetization was effective in Hole BA4A samples (Fig. **F58A**), with more than 90% of remanence removed by 60 mT in nearly all samples (Fig. **F58B**). Median destructive field (MDF) values range 12–32.1 mT (mean = 19.9 mT) (Table **T11**). There is no trend in MDF values with depth (Fig. **F60**). The soft components isolated by AF demagnetization have a mean inclination of 53°.

Thermal demagnetization was complete in nearly all samples by a temperature of 675°C (Fig. **F59A**). Distinct drops in remanence intensity occurred at 500°–550°C and 625°–675°C in various samples (Fig. **F59B**). Changes in magnetic susceptibility were observed after selected thermal demagnetization steps. Bulk susceptibilities increased significantly with pro-

gressive heating in all but one sample, reflecting the growth of secondary minerals during thermal alteration of the rocks. A few samples became fractured during heating due to thermal decomposition of vein material and could not be fully demagnetized. Median destructive temperatures (MDT) range 376°–661°C (mean = 599°C) and lack any trend with depth (Fig. F60). The soft components isolated by thermal demagnetization have a mean inclination of 38°, which is slightly lower than those determined by AF demagnetization. As in Hole BA3A, most MDT values are too high for the remanence to be carried by stoichiometric magnetite, but the low fields needed for AF demagnetization indicate that the coercivities are too low for hematite to be the dominant remanence-carrying phase.

Magnetic susceptibility

Bulk magnetic susceptibility

Volume susceptibility values range between 1.28 and 32.6 × 10^{-3} SI (geometric mean = 4.58 × 10^{-3} SI) (Fig. F56; Table T11). Samples from the uppermost 50 m of the hole are characterized by higher bulk susceptibilities than those from greater depths, with an average around 8.2 × 10^{-3} SI. Koenigsberger ratios, Q, range 0.051–27 (average = 3.1). The wide spread in Q values (Fig. F56; Table T11) suggests that remanence stability is highly variable throughout the hole. Further work should investigate whether this variation arises from differences in magnetic mineral abundance, composition, grain size, or other properties.

Anisotropy of magnetic susceptibility

Anisotropy of magnetic susceptibility (AMS) determinations were performed on all discrete samples prior to stepwise demagnetization to characterize the shape-preferred orientations of magnetic minerals. Magnetic fabric shapes vary from strongly oblate (T = 0.96) to strongly prolate (T = –0.91), although magnetic foliations are more prevalent (Fig. F61A). Many samples are triaxial with moderate T values, indicating a well-defined magnetic lineation (K_{max} axis) (Fig. F61C; Table T12). Fabric intensities vary from moderate to strong, with P' values as high as 1.37 (average = 1.10). The degree of anisotropy is not correlated with bulk susceptibility (K_{mean}) (Fig. F61B).

K_{max} axes have consistently low inclinations (average = 28°) (Fig. F61A). These axes exhibit a weak clustering near the ± X direction in the CRF (Fig. F62). K_{min} axes are also weakly concentrated along a plane normal to the K_{max} maxima (Fig. F62), approximately parallel to the ± Y-direction of the CRF. Magnetic fabric orientations do not vary systematically with depth. The magnetic anisotropy characteristics of Hole BA4A samples is overall very similar to those from Hole BA3A.

Physical properties

Physical properties of ultramafic rocks and gabbroic dikes in Hole BA4A were characterized through a series of measurements on whole-round sections, section halves, section-half pieces, and discrete samples (see **Physical properties** in the **Methods** chapter). All whole-round sections were run through the X-ray computed tomography (XCT) scanner and measured for gamma ray attenuation (GRA) density, magnetic susceptibility (MS), noncontact electrical resistivity (NCR), and natural gamma radiation (NGR) with the whole-round multisensor core logger (MSCL-W). Whole-round P-wave velocity was not measured because of a mechanical issue with the transmitter. We also measured point magnetic susceptibility (MSP) and reflectance spectroscopy and colorimetry (RSC) with the color spectroscopy logger (MSCL-C) and line-scan color image with the photo image logger (MSCL-I) on the split surface of archive halves. Thermal conductivity was measured on section-half pieces. Compressional wave (P-wave) velocity (V_P), electrical resistivity (IMP), and density and porosity (MAD) were measured on discrete minicube samples (20 mm × 20 mm × 20 mm). MAD measurements were also conducted on some irregularly shaped discrete samples. The rock names reported in data tables correspond to the primary lithologies described in **Background description**.

Whole-round and section-half measurements

A total of 413 whole-round and archive-half sections in Hole BA4A were measured from Cores 1Z–109Z. The downhole data plot is shown in Figure F63 for whole-round measurements. All data are shown in supplemental Tables ST6 and ST7.

X-ray computed tomography

XCT was continuously logged for all 413 whole-round core sections recovered from Hole BA4A. The XCT number of minerals is essentially a function of the density and chemical composition of the sample. Hence, XCT numbers in the core sections result from a combination of their mineral composition and pore structure in a voxel (0.625 mm × 0.175 mm × 0.175 mm). Figure F64 shows examples of XCT images from Sections 49Z-4 and 92Z-1. The veins and fractures are visible in these images, and the dip angle can be analyzed through the whole-round image.

An XCT image of the archive-half split surface with the XCT number represented on a color scale was generated for every section. The average and mode of XCT numbers for every scan slice (0.625 mm thick) were also computed and plotted (Fig. F63). Average XCT number is susceptible to the effect of cracks in

the core section because the XCT number of the air is significantly lower than that of minerals (XCT number of air is approximately –1000; see **Physical properties** in the **Methods** chapter). On the other hand, the mode of XCT numbers tends to reflect a representative lithology in a scan slice, although it overlooks some minor but dense minerals (e.g., Cr-spinel).

In Hole BA4A, ultramafic rocks have average XCT numbers of ~2800. The shallow portions show lower XCT numbers, reflecting extensive weathering and high porosity. Harzburgite shows relatively high XCT numbers compared with dunite. This reflects either the higher abundance of orthopyroxene or a lower degree of serpentinization in harzburgite compared to dunite.

Because XCT numbers of a core section depend on mineral composition and porosity, the trends of the average and mode of XCT numbers clearly follow that of the GRA density in the downhole plot (Fig. **F63**). All lithologies show a relation between XCT number and GRA density. These correlations can be controlled by several factors, such as modal abundances of low-density minerals (e.g., serpentine), abundance of high atomic number elements in minerals (e.g., calcium in diopside, iron in magnetite, and chromium in Cr-spinel), and pore structure. Overall, variability in the XCT number downhole trends reflect the lithologic and structural variations observed in Hole BA4A.

Colorimetry

RSC data were obtained for 413 sections of archive halves from Cores 1Z–109Z. The specular component included (SCI) setting was used for measuring Hole BA4A cores, and this setting provides data that are closer to the actual color than that of the specular component excluded (SCE) setting (see **Physical properties** in the **Methods** chapter). Color data acquired from reflectance spectroscopy and high-resolution images can provide insights into the variability of different lithologic units recovered from Hole BA4A. Lightness (L*) and chromaticity (a* and b*) variables were generated from the reflected light collected through the spectrophotometer every 2 cm. High L* value indicates lighter colors; 0 represents black and 100 represents white. Directions toward more +a* denote a shift toward red from green, whereas +b* depicts a shift toward yellow from blue. High-resolution (100 pixels/cm) section-half images produced by the MSCL-I provide an alternative source of 2-D color data. Although a* and b* are nearly constant or gradually change with depth, harzburgites show a markedly higher L* compared with dunites. This is most likely due to less alteration and relatively low porosity in harzburgite.

Gamma ray attenuation density

GRA density measurements were conducted for the 413 sections at a spacing of 4 cm. Data are summarized in Figure **F63**. The GRA density values for shallow depths are significantly lower than the deeper sequence because of weathering and high porosity. The depth profile of bulk density values obtained from discrete sample measurements seems to follow the upper boundary of the GRA density depth profile. Figure **F65** shows correlation between GRA densities and XCT values. GRA density is correlated to XCT value with density >2.5 g/cm^3, whereas it is highly scattered with low density, possibly due to relatively high porosity in the samples.

Electrical resistivity

NCR data indicate that the cores from Hole BA4A are relatively resistive (Fig. **F63**). Most readings in this sequence are saturated and equal to the maximum measurable value (~85 Ωm); therefore, actual averages of NCR for these sections could be higher than shown in Figure **F63**. Although variation of resistivity is large even in a same lithology, resistivity tends to increase with depth. The resistivity of ultramafic rocks is generally related to hydration (serpentinization) due to the formation and connection of magnetite, suggesting less hydration in the deeper portion relative to the shallow portion, similar to that observed in Hole BA1B. We note that NCR is systematically ~20× lower than the electrical resistivity measured from discrete samples (Figs. **F63**, **F66**). This can be due to the low accuracy of NCR measurements of high-resistivity samples because the instrument is designed for measuring the resistivity of porous and conductive ocean-wet sediments, whereas overall characteristics of NCR in a depth profile are quite similar to that of the discrete sample data.

Whole-round magnetic susceptibility

The MS of whole-round core sections before splitting was measured using the MSCL-W with a 125 mm loop sensor. Whole-round MS values are shown in Figure **F63**. MS is ~1000 × 10^{-5} SI for ultramafic rocks in Hole BA4A. Figure **F65** shows a correlation between MS and the inverse of NCR (i.e., the electrical conductivity measured in same depth). MS and inverse NCR show a linear correlation.

Natural gamma radiation

NGR in Hole BA4A is generally low (Fig. **F63**). There seems to be no or few correlations with other physical property data and structural observations.

Discrete sample measurements

P-wave velocity

P-wave velocity was measured for Hole BA4A on 104 cube samples along the 3 principal directions, *x*, *y*, and *z*, in the CRF (Tables **T13**, **T14**; Fig. **F66**). *P*-wave velocity averages 5.13 ± 0.42 km/s for dunites and

5.47 ± 0.13 km/s for harzburgites. Gabbroic layers exhibit higher velocities, with a maximum velocity of 6.60 km/s. *P*-wave velocity at shallow depths is relatively scattered because of weathering and relatively large variation of porosity. Dunite and harzburgite samples show a slight increase of velocity with depth, suggesting less serpentinization in the deeper portion (Fig. F66). Similar trends are observed in Holes BA1B and BA3A. *P*-wave velocity of dunites is slightly slower than the surrounding harzburgites.

Azimuthal anisotropy (A_V) of *P*-wave velocity is calculated from

$$A_V = (V_{max} - V_{min})/V_{mean}, \quad (2)$$

where V_{max} and V_{min} are the maximum and minimum velocities, and V_{mean} is the average velocity of the three orthogonal directions (Birch, 1961). The azimuthal anisotropy mostly ranges 1%–6% (Fig. F67). *P*-wave velocity along the *z*-axis tends to be slower than the other directions, consistent with Holes BA1B and BA3A, whereas anisotropy is relatively small compared to the previous holes.

Density and porosity

Bulk density, grain density, and porosity were calculated from measurements on 104 cube samples (20 mm × 20 mm × 20 mm) taken from the working-half sections from Hole BA4A, ~1 sample per core and reflecting lithologic and alteration variation (Tables T13, T14; Fig. F66). Average bulk density values from Hole BA4A are 2.53 ± 0.06 g/cm³ for dunite and 2.63 ± 0.05 g/cm³ for harzburgite. Like in the previous holes, the cube samples were mostly taken from relatively homogeneous intervals with fewer or no visible cracks or veins. Note that some samples exhibit an extremely high porosity (>10%) that might be due to chip-off during MAD measurements. The highly altered or deformed samples have high porosities (up to 16%) and lower bulk densities (as low as 2.39 g/cm³) and grain densities (2.49 g/cm³). Figure F66 shows that bulk density of the discrete samples increases slightly with depth, which agrees with the velocity data. The low grain densities of dunites (~2.55 g/cm³) at shallow depths suggest that olivine (~3.3 g/cm³) in these rocks is nearly 100% serpentinized (density of lizardite serpentine = ~2.58 g/cm³; Mellini and Zanazzi, 1987). Grain density tends to increase slightly with depth, up to ~2.70 g/cm³ and as low as ~80% serpentinization, which is nearly consistent with Hole BA3A but slightly higher than in Hole BA1B.

The porosities of discrete cube samples range 0.8%–15.6% (dunite mean = 2.87%; harzburgite mean = 1.35%). Gabbro samples show porosities ranging 0.5%–8.5%, in which the rodingitized gabbros are characterized by a relatively high porosity. The shallow sequence shows scattered and relatively high porosity up to 15.6%, reflecting weathering near the surface, whereas ultramafic rocks in deeper portions show a nearly constant porosity (Fig. F66).

Relationships between density, *P*-wave velocity, and porosity in Hole BA4A are shown in Figures F68 and F69 and compared to data from Hole BA3A. *P*-wave velocity tends to increase with increasing bulk and grain density, where ultrasonic velocity depends on porosity and alteration of ultramafic rocks (Christensen, 2004). Similar features are seen in ultramafic rocks from Holes BA1B and BA3A (see **Physical properties** in the **Site BA1** chapter and **Physical properties** in the **Site BA3** chapter).

The relationship between porosity and the average XCT value for the discrete cube samples is shown in Figure F70. The data follow the trend from Holes BA1B and BA3A using separate line fits for dunites and harzburgites for XCT numbers <2980 and <3000, respectively. Figure F71 shows the standard deviation of XCT numbers plotted with grain density. The data are scattered, but samples with large deviation tend to show high grain density. Figure F72 shows a downhole porosity plot inferred from the XCT data using the linear fitting curve. The major peaks in the 122 cm moving mean (blue) are related to deformation zones, whereas peaks in the 6.1 cm moving mean (red) are caused by open cracks. Notice that the porosity of discrete cube samples (green) tends to correlate with local minimum values in porosity estimated based on XCT numbers, suggesting that the overall porosity of the core is higher than indicated by the discrete samples.

Electrical resistivity

Electrical resistivity was measured in 104 cube samples from Hole BA4A (Tables T13, T14; Fig. F66). Resistivity ranges 49–15,031 Ωm. Resistivity data are relatively scattered in Hole BA4A compared to previous Holes BA1B and BA3A. There is no systematic variation with depth, but resistivity is weakly correlated with porosity. We measured both dry and wet resistivity; wet resistivity is lower than dry resistivity. The difference in dry and wet resistivity is likely related to crack density and the connectivity in samples. The relatively large difference in dry and wet resistivity can be related to permeable zones related to fracturing.

Electrical resistivity has a weak correlation with bulk MS in the same cube samples (Fig. F73),

$$R = 1389 \times B^{-0.076} \qquad (R^2 = 0.056), \quad (3)$$

where *R* is dry resistivity of the cube sample, and *B* is bulk MS of the cube sample. Similar features are found in previous holes, including Holes BA1B and BA3A, but the correlation is relatively weak in Hole BA4A.

Magnetic susceptibility

MS was measured in 104 cube samples from Hole BA4A (Tables T13, T14; Fig. F66). MS ranges from 0.0003 × 10^{-5} to 0.0309 × 10^{-5} SI (dunite average = 0.0072 × 10^{-5} SI for dunite; harzburgite average = 0.0046 × 10^{-5} SI), nearly consistent with measurements for Holes BA1B and BA3A. Gabbros show a relatively lower MS than ultramafic rocks (see Table T10 in the **Site BA3** chapter). Bulk MS shows no systematic variation with depth but is correlated to porosity and resistivity, in which samples with high porosity and low resistivity show relatively high MS. MS measured in 3 orthogonal directions displays contrasting patterns between bulk susceptibility and angular deviation of *x*-, *y*-, and *z*- axes. The directional deviation pattern of axial susceptibility is distinct for each *x*-, *y*-, and *z*-axis, in which measurements along the *x*-axis indicate a continuous increase in angular value, whereas no systematic deviation is evident along the *y*- and *z*-axes. It is notable that the depths of the anomaly points are near the depths where bulk MS anomalies are observed.

Thermal conductivity

A total of 83 measurements were taken on core pieces of the working halves from Hole BA4A (Tables T13, T15; Fig. F66). Thermal conductivity ranges 1.89–2.26 W/m·K. Thermal conductivity is nearly constant or increases slightly with depth, in which the variation is relatively small compared to values from Holes BA1B and BA3A. Thermal conductivities are similar to those reported in the harzburgites from Ocean Drilling Program Leg 209 Hole 1274A (Mid-Atlantic Ridge; 1520'N Fracture Zone; Kelemen et al., 2004). Thermal conductivity is weakly correlated to XCT number (Fig. F74).

Imaging spectroscopy

All sections of Hole BA4A were imaged onboard the *Chikyu* during Leg 3. The exception were the sections and portions of sections removed during drilling for microbiology analyses; these were not available to scan. The ~300 m of Hole BA4A was imaged in six 12 h shifts over 3 days. A total of 404 sets of images (visible near infrared [VNIR] and short-wave infrared [SWIR]) were acquired of core sections. An initial check of data quality was good, and the images will be processed and analyzed at Caltech. This core was similar to Hole BA3A; for an example of the dataset, see Imaging spectroscopy in the **Site BA3** chapter.

Downhole logging and hydrogeological testing

Downhole logging and hydrogeological testing operations and acquisition parameters for each borehole are available in Tables T2 and T3 in Downhole logging and hydrogeological testing in the **Methods** and explanatory notes chapter. Raw and processed data from all downhole logs are available in Supplementary material > **L_Wireline logging** and in the ICDP Oman Drilling Project online data repository (http://oman.icdp-online.org).

References

Arason, P., and Levi, S., 2010. Maximum likelihood solution for inclination-only data in paleomagnetism. Geophysical Journal International, 182:753-771. https://doi.org/10.1111/j.1365-246X.2010.04671.x

Barrat, J.A., Zanda, B., Moynier, F., Bollinger, C., Liorzou, C., and Bayon, G., 2012. Geochemistry of CI chondrites: Major and trace elements, and Cu and Zn isotopes. Geochimica et Cosmochimica Acta, 83:79-92. https://doi.org/10.1016/j.gca.2011.12.011

Birch, F., 1961. The velocity of compressional waves in rocks to 10 kilobars, Part 2. Journal of Geophysical Research, 66:2199–2224.

Cardozo, N., and Allmendinger, R.W., 2013. Spherical projections with OSXStereonet. Computers & Geosciences, 51:193–205. https://doi.org/10.1016/j.cageo.2012.07.021

Christensen, N.I., 2004. Serpentinites, peridotites, and seismology. International Geology Review, 46:795–816.

Godard, M., Jousselin, D., and Bodinier, J.L., 2000. Relationships between geochemistry and structure beneath a paleo-spreading center: a study of the mantle section in the Oman ophiolite. Earth and Planetary Science Letters, 180(1-2):133-148. http://dx.doi.org/10.1016/S0012-821X(00)00149-7

Godard, M., Awaji, S., Hansen, H., Hellebrand, E., Brunelli, D., Johnson, K., Yamasaki, T., Maeda, J., Abratis, M., Christie, D., Kato, Y., Mariet, C., and Rosner, M., 2009. Geochemistry of a long in situ section of intrusive slow-spread oceanic lithosphere: Results from IODP Site U1309 (Atlantis Massif, 30°N Mid-Atlantic-Ridge). Earth and Planetary Science Letters, 279:110-122. https://doi.org/10.1016/j.epsl.2008.12.034

Hanghøj, K., Kelemen, P.B., Hassler, D., and Godard, M., 2010. Composition and genesis of depleted mantle peridotites from the Wadi Tayin Massif, Oman Ophiolite; major and trace element geochemistry, and Os isotope and PGE systematics. Journal of Petrology, 51(1-2):201-227. https://doi.org/10.1093/petrology/egp077

Kelemen, P.B., Kikawa, E., Miller, D.J., et al., 2004. Proceedings of the Ocean Drilling Program, Initial Reports, 209: College Station, TX (Ocean Drilling Program). https://doi.org/10.2973/odp.proc.ir.209.2004

Khedr, M.Z., Arai, S., Python, M., and Tamura, A., 2014. Chemical variations of abyssal peridotites in the central Oman ophiolite: Evidence of oceanic mantle heterogeneity. Gondwana Research, 25(3):1242-1262. https://doi.org/10.1016/j.gr.2013.05.010

Lippard, S.J., Shelton, A.W., and Gass, I.G., 1986. The ophiolite of northern Oman. In The Geological Society Memoirs, 11: Malden, Mass. (Blackwell Sci.)

McDonough, W.F., and Sun, S.S., 1995. The composition of the Earth. Chemical Geology, 120(3-4):223-253. https://doi.org/10.1016/0009-2541(94)00140-4

Mellini, M., and Zanazzi, P.F., 1987. Crystal structures of lizardite-1T and lizardite-2H1 from Coli, Italy. American Mineralogist, 72:943–948.

Monnier, C., Girardeau, J., Le Mée, L., and Polvé, M., 2006. Along-ridge petrological segmentation of the mantle in the Oman ophiolite. Geochemistry, Geophysics, Geosystems, 7(11). https://doi.org/10.1029/2006GC001320

Noel, J., 2018. Etude pétro-structurale et géochimique des processus de serpentinisation et carbonatation des péridotites d'Oman [Ph.D. Thesis]. University of Montpellier, France.

Rospabe, M., Benoit, M., Ceulenner, G., Hodel, F., and Kaczmarek, M.A., 2018. Extreme geochemical variability through the dunitic transition zone of the Oman ophiolite: implications for melt/fluid-rock reactions at Moho level beneath oceanic spreading centers. Geochimica Cosmochmica Acta, 234:1-23. https://doi.org/10.1016/j.gca.2018.05.012

Sun, S.-S., and McDonough, W.F., 1989. Chemical and isotopic systematics of oceanic basalts: implications for mantle composition and processes. Magmatism in the Ocean Basins. Geological Society Special Publication, London, 313–345.

Takazawa, E., Okayasu, T., and Satoh, K., 2003. Geochemistry and origin of the basal lherzolites from the northern Oman ophiolite (northern Fizh block). Geochemistry, Geophysics, Geosystems, 4(1021). https://doi.org/10.1029/2001GC000232

Whitney, D.L., and Evans, B.W., 2010. Abbreviations for names of rock-forming minerals. American Mineralogist, 95:185–187.

Figure F1. BA4 drill site during coring operations, looking north.

Figure F2. Lithology thicknesses and units, Hole BA4A.

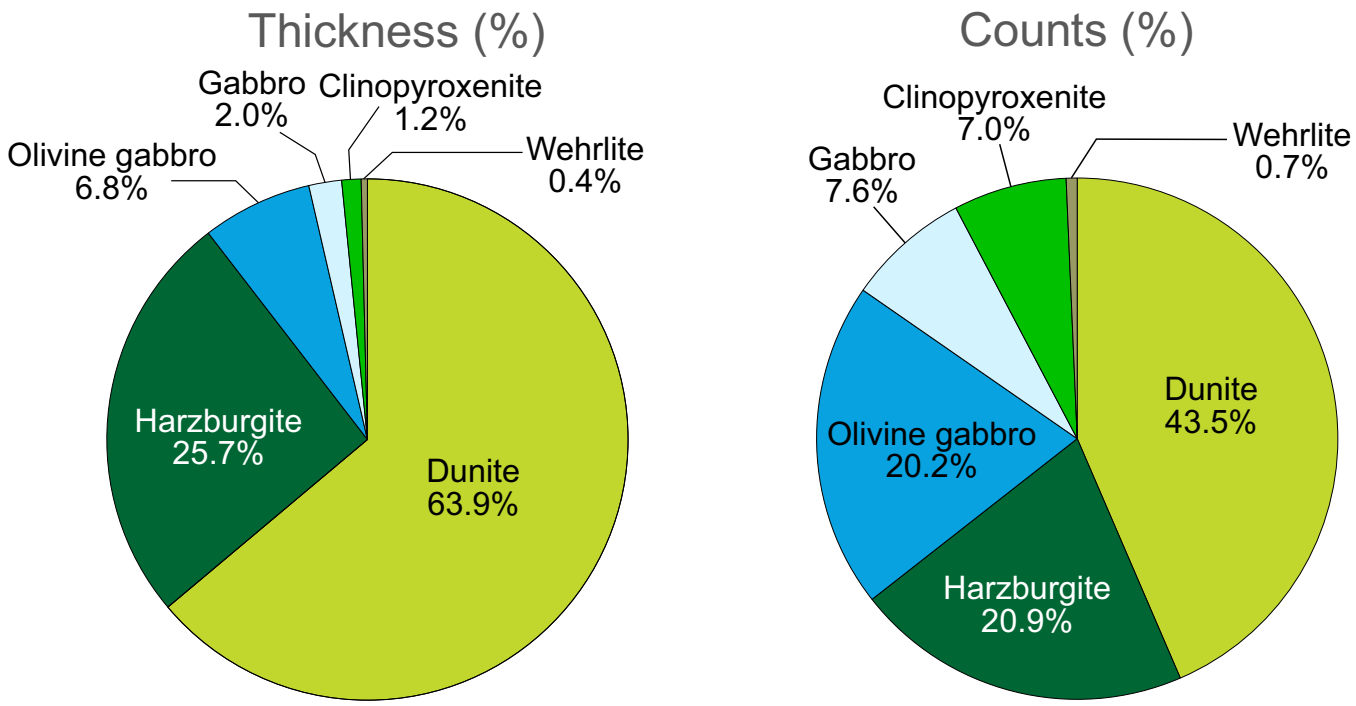

Figure F3. Borehole summary, Hole BA4A.

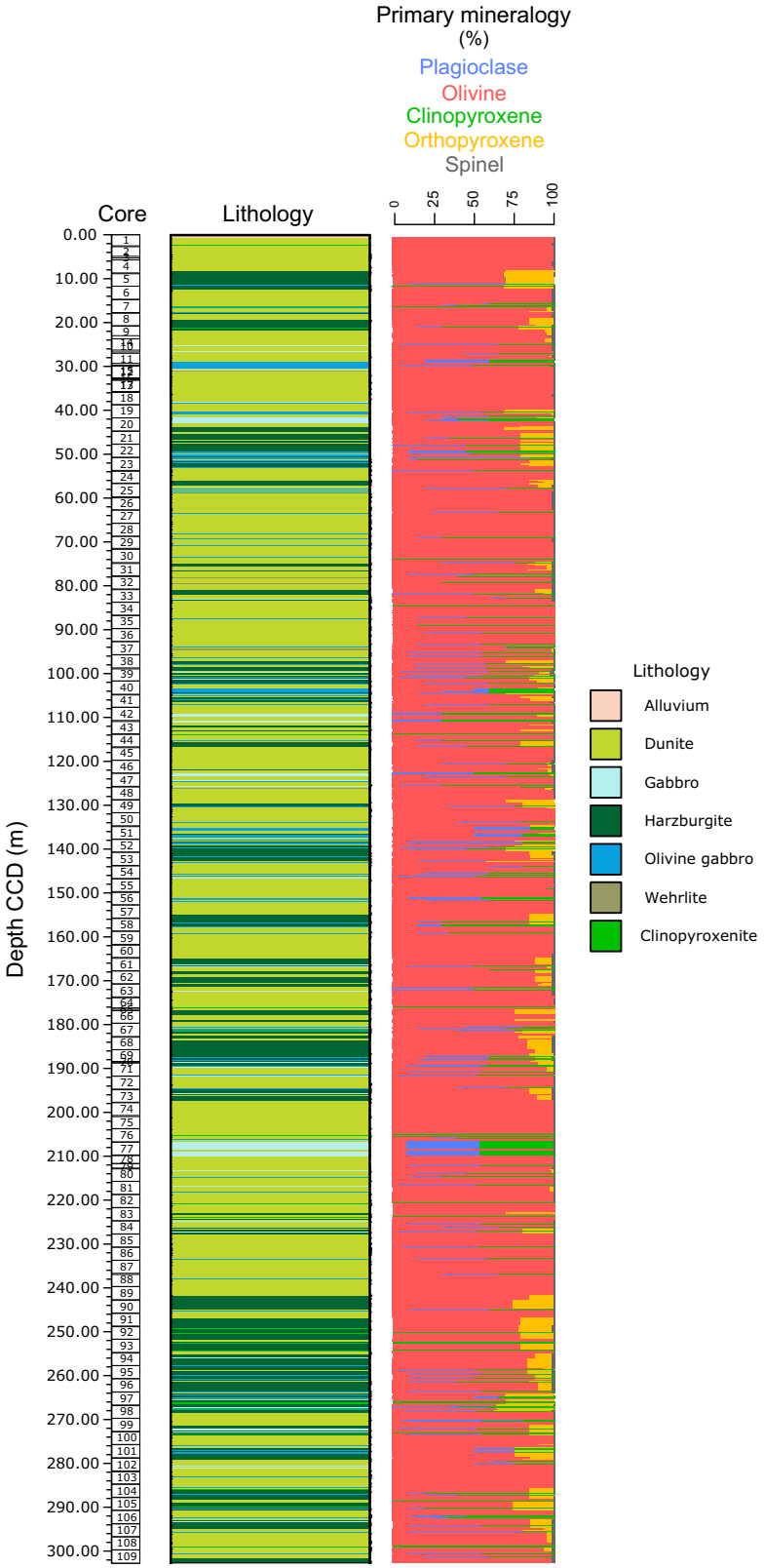

Figure F4. Distribution of (**A**) harzburgites and dunites and (**B**) mineral modes in harzburgites and dunites, Hole BA4A. Ol = olivine, Opx = orthopyroxene, Sp = spinel.

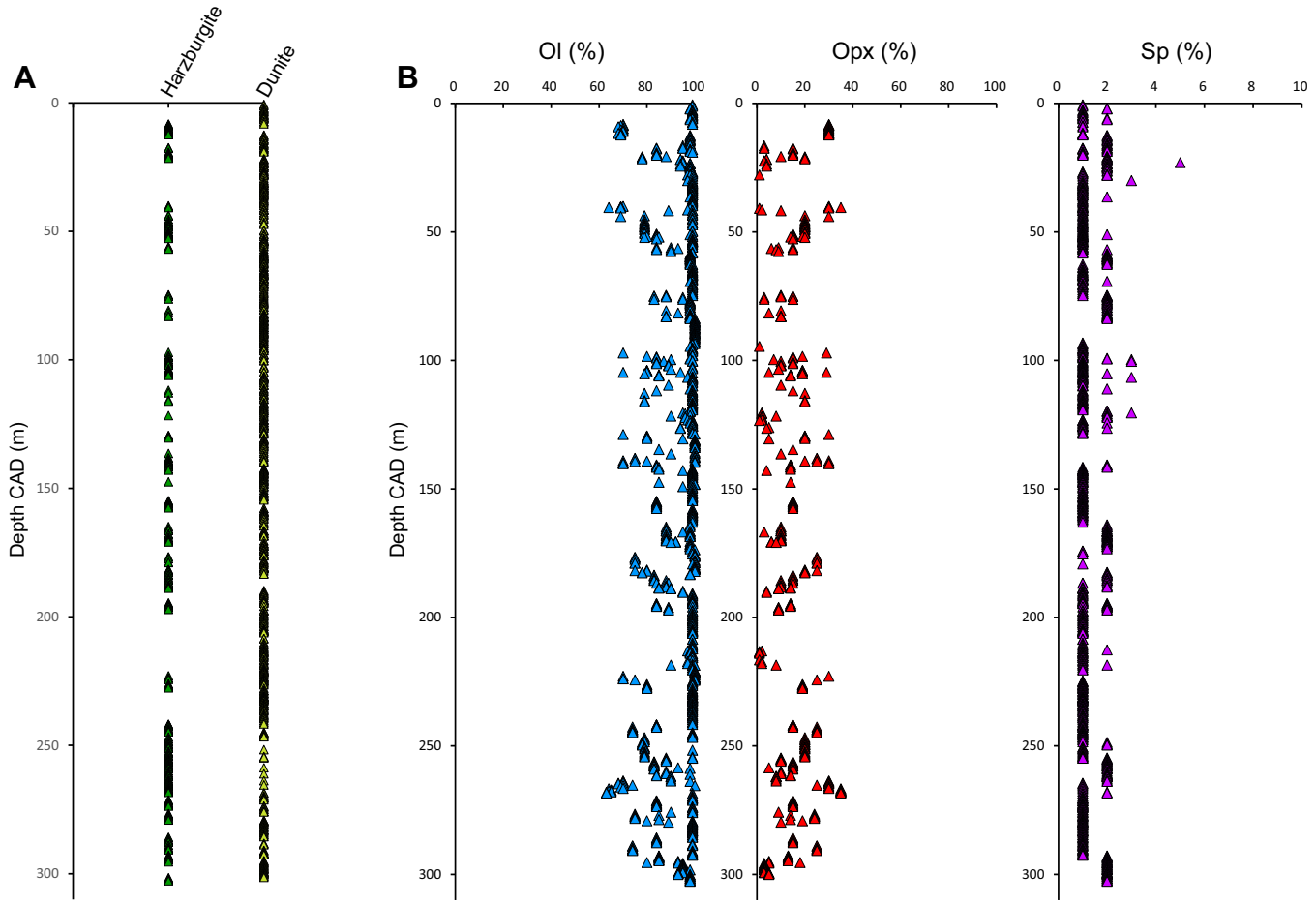

Figure F5. Distribution of (**A**) dike types and (**B**) mineral modes in the dikes, Hole BA4A. Ol = olivine, Plag = plagioclase, Cpx = clinopyroxene.

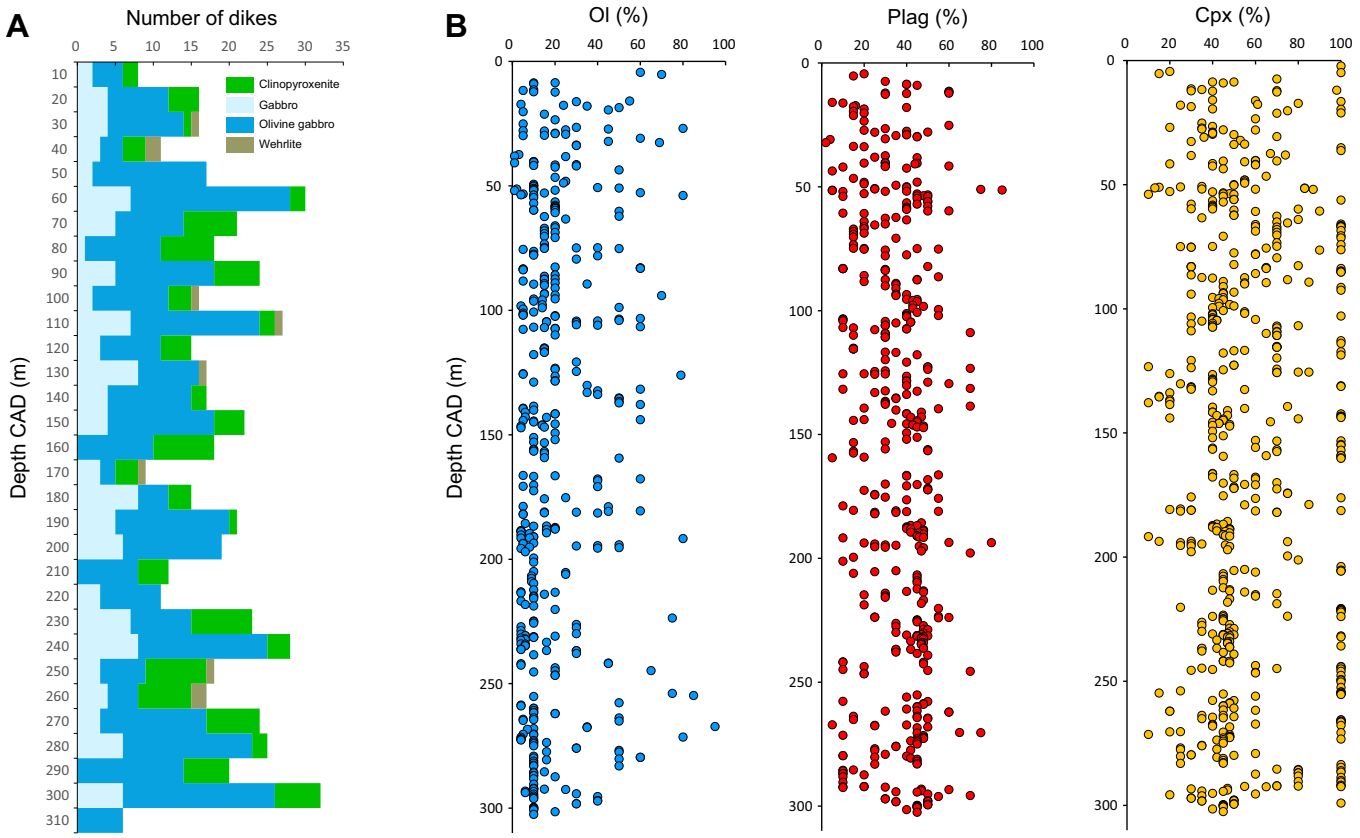

Figure F6. Distribution of oxidized zones and thickness of oxidized material for each 10 m interval, Hole BA4A.

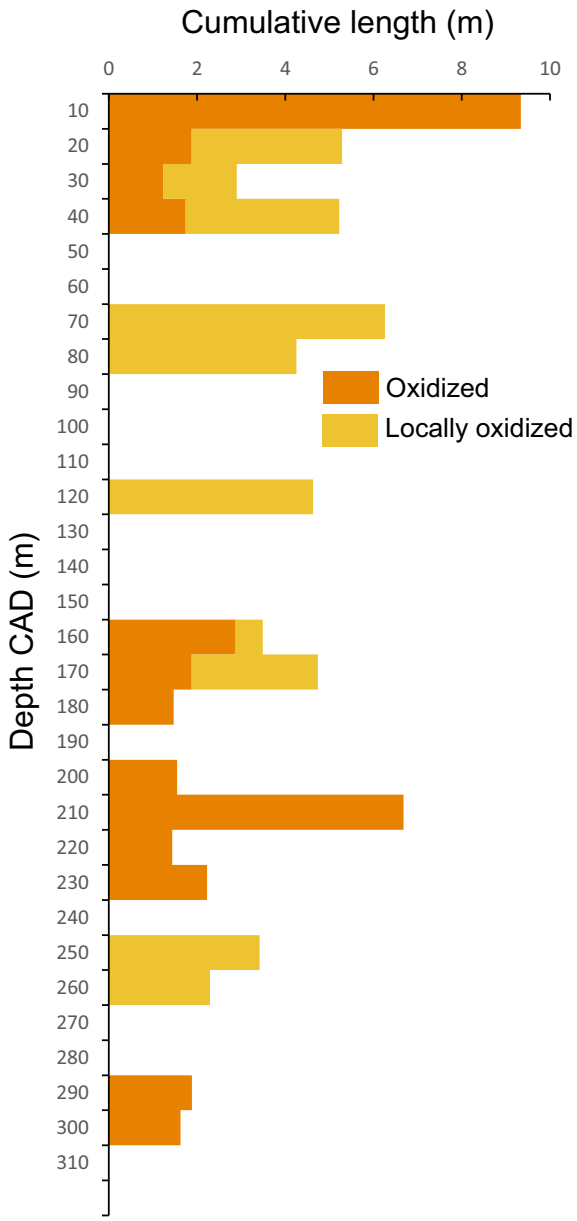

Figure F7. Representative rock types, Hole BA4A. **A.** Oxidized dunite with carbonate veins (Section 4Z-1). **B.** Dunite (82Z-1). **C.** Harzburgite (52Z-4). **D.** Gabbro dike with pseudomorphic alteration and vein (40Z-1). **E.** Olivine gabbro (51Z-1). **F.** Altered clinoproxenite dike with hydrogrossular-bearing alteration (see XRD Sample 9Z-1, 41.0 cm; Table T4). **G.** Altered wehrlitic dike with pseudomorphic texture around 35 cm (76Z-4). **H.** Disseminated clinopyroxene (48Z-1).

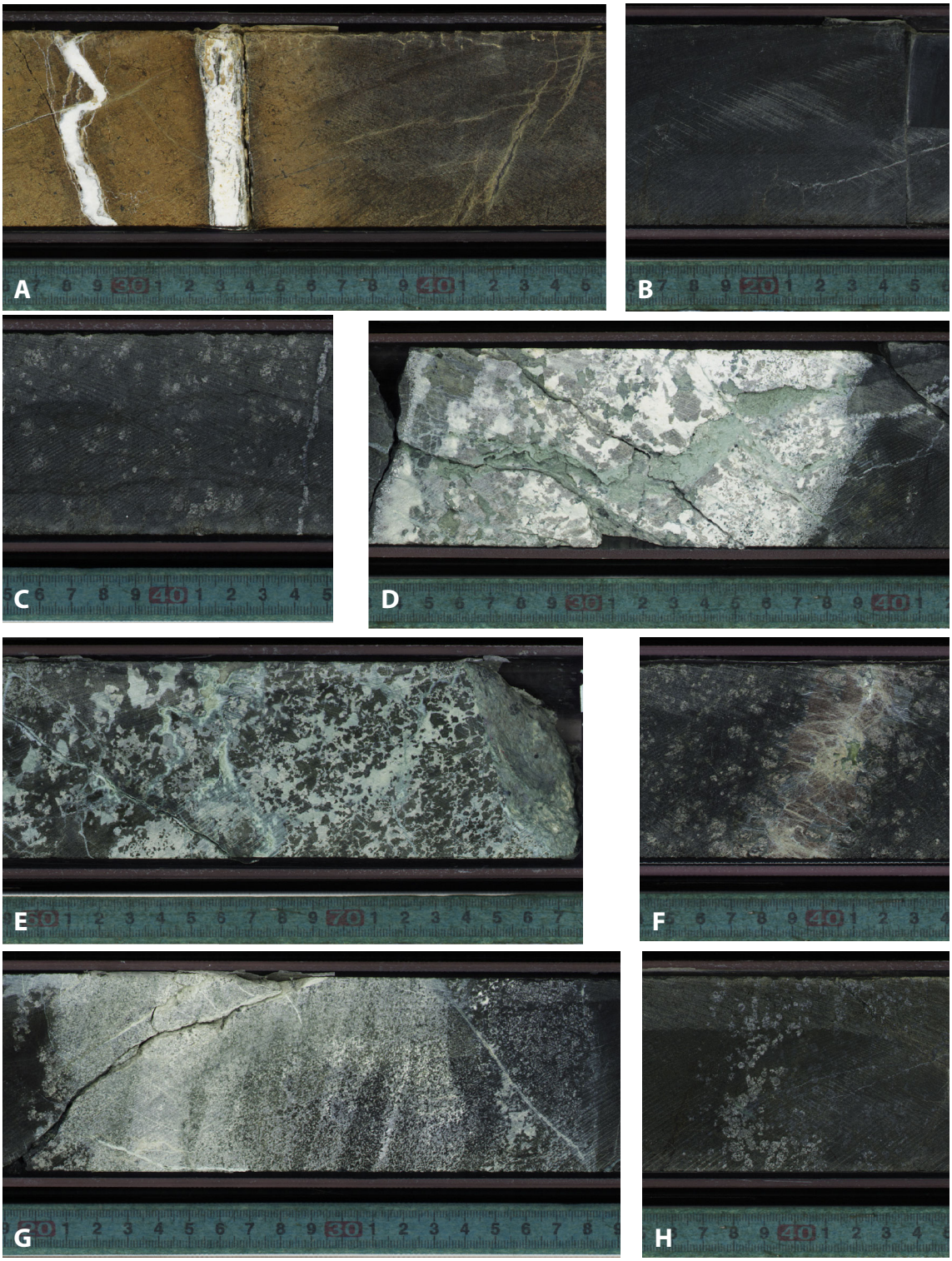

Figure F8. Oxidized zone rocks and dunites, Hole BA4A. **A, B.** Harzburgite from oxidized zone with orthopyroxene (Opx) and altered olivine (Sample 5Z-2, 56–61 cm; 10.25 m depth;, ×2.5; A: plane-polarized light [PPL], B: cross-polarized light [XPL]). **C.** Black-cored altered olivine mesh (19Z-3, 0–6 cm; 39.9 m; ×2.5; PPL). Srp = serpentine. **D.** Clear-cored altered olivine mesh (82Z-1, 25–30 cm; 219 m; ×2.5; PPL). **E.** Black/clear-cored olivine mesh (102Z-3; ×5; PPL). **F, G.** Fingerprint olivines (82Z-1, 25–30 cm; ×20; F: PPL, G: XPL).

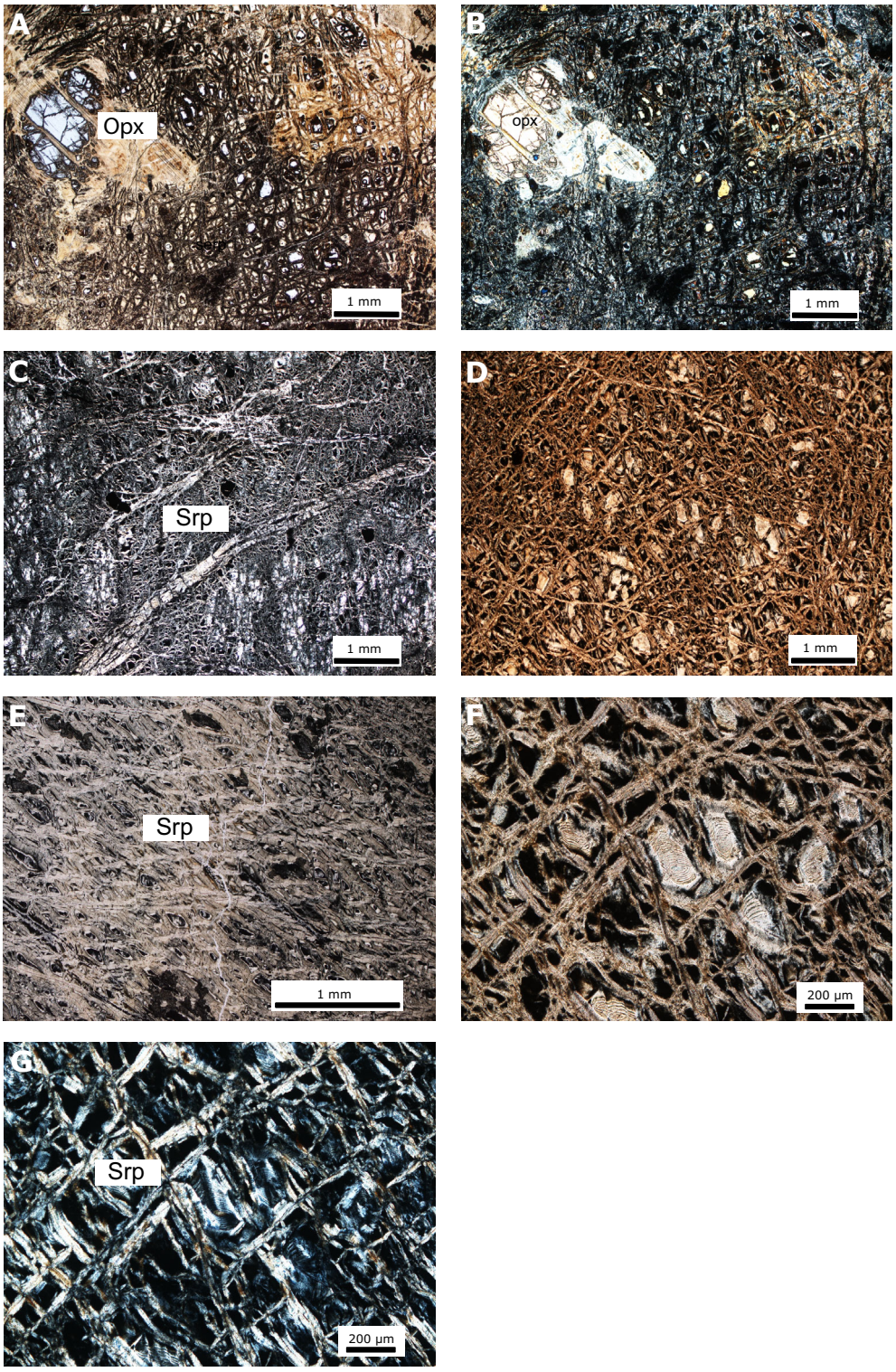

Figure F9. Dunites, Hole BA4A (reflected light [RL]). **A.** Magnetite (Mag) after spinel with chalcopyrite (Cp) and associated oxidation products (Sample 102Z-3, 37–42 cm; 280.4 m; ×20) Cup = cuprite. **B.** Deformed sulfide in a vein with associated oxidation products (19Z-3, 0–6 cm; 39.9 m; ×20). Hz = heazlewoodite. **C.** Sulfide (Sulf) in a vein with magnetite rim (82Z-1, 25–30 cm; 219 m; ×5).

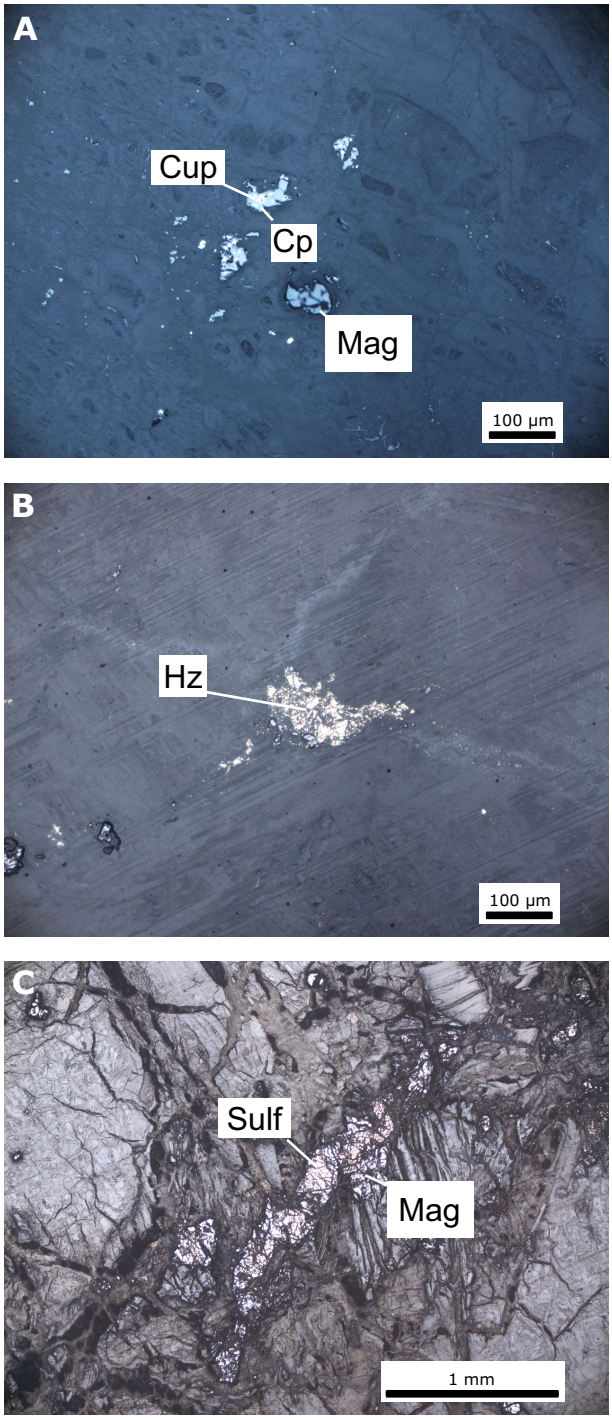

Figure F10. Harzburgite observations, Hole BA4A (52Z-4, 0–5 cm; 140 m). **A.** Clear, black, and intermediate cores of altered olivine mesh (×10; PPL). Srp = serpentine. **B.** Deformation of orthopyroxene associated with veins in places (×2.5; PPL). **C, D.** Orthopyroxene (Opx) altered to serpentine plus chlorite in places (×2.5; C: PPL, D: XPL). **E, F.** Clinopyroxene (Cpx) lamellae in deformed olivine (×5; E: PPL, F: XPL). **G, H.** Black alteration on clinopyroxene grain (×5; G: PPL, H: XPL). Ol = olivine.

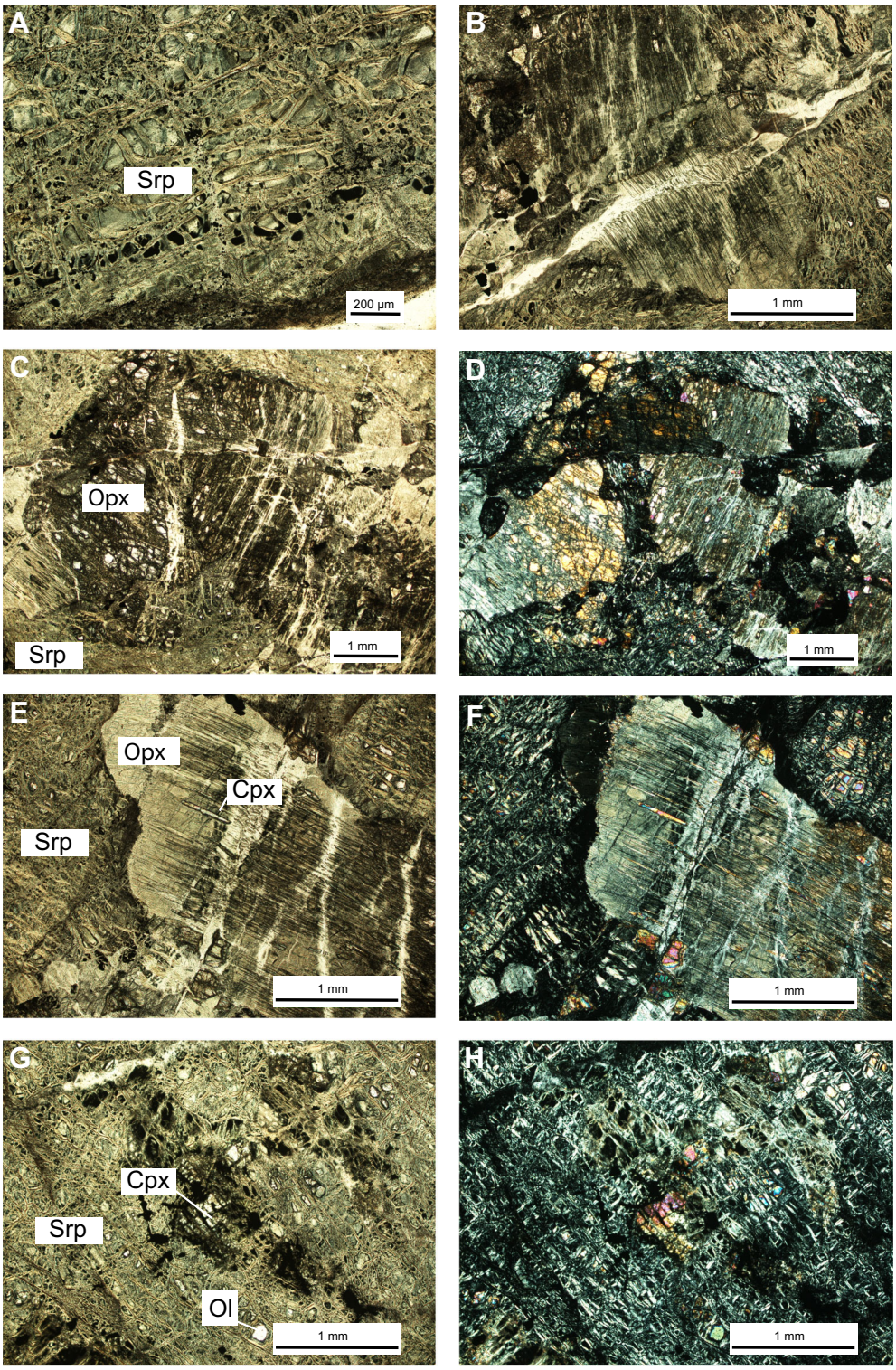

Figure F11. Harzburgites, Hole BA4A (A, B, D: 31Z-1, 32–34 cm; 75 m; RL). **A.** Magnetite (Mag) intergrown with olivine (Ol) relics (×5). **B.** Vein magnetite and chalcopyrite (Cp) with cuprite (Cup) rims (×10). **C.** Colliform cuprite rims on chalcopyrite adjacent to heazlewoodite (Hz) (52Z-4, 0–5 cm; 140 m; ×40). **D.** Deformed sulfide (Sulf; undifferentiated) (×20).

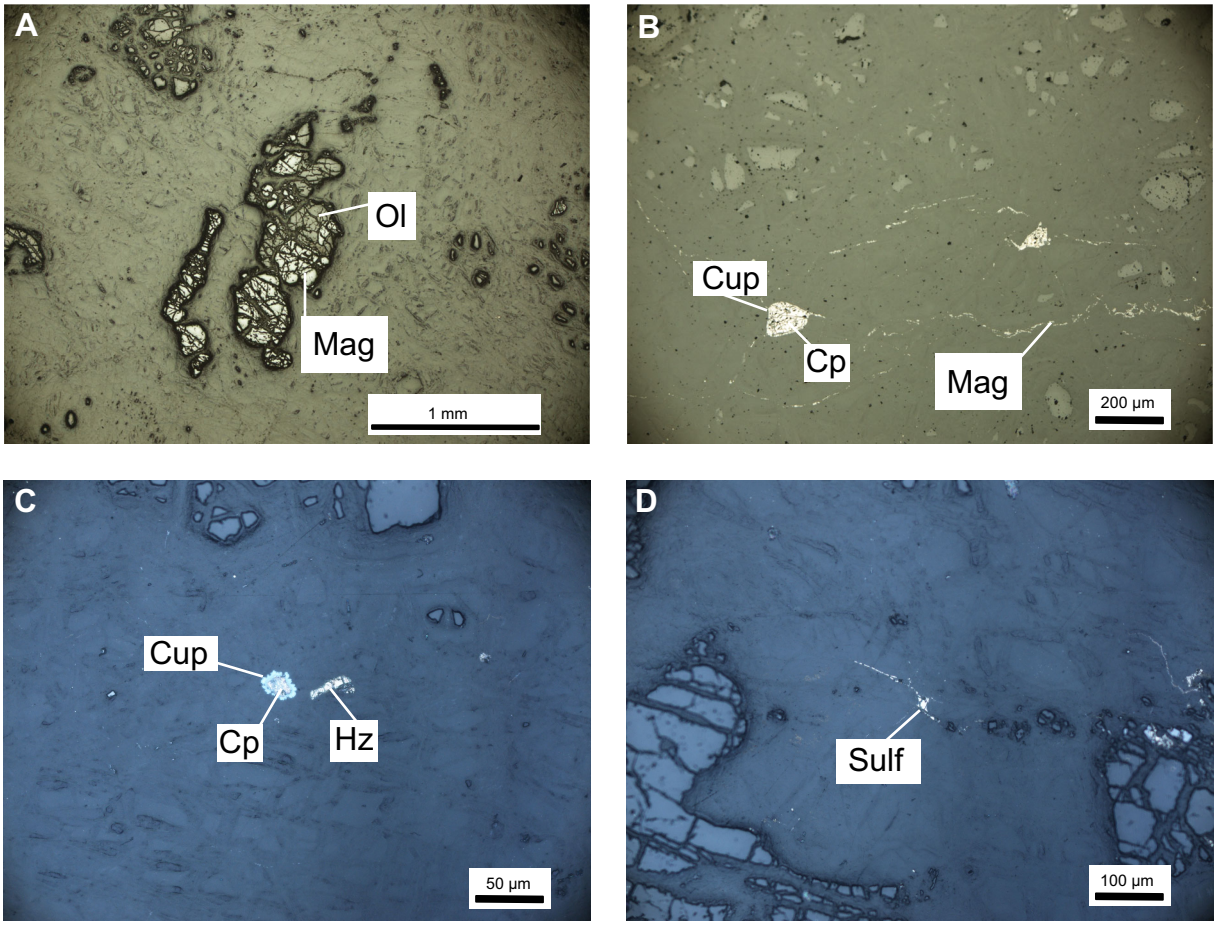

Figure F12. Pseudomorphically altered gabbros, Hole BA4A (40Z-1, 33–35 cm; 102 m). **A, B.** Olivine replaced by serpentine and chlorite (Srp + Chl) surrounded by plagioclase altered to clay (×2.5; A: PPL, B: XPL). **C, D.** Clinopyroxene (Cpx) with clay-altered plagioclase inclusions (×2.5; C: PPL, D: XPL). **E, F.** Clinopyroxene altered to tremolite (Tr) (×10; E: PPL, F: XPL). **G, H.** Hydrogrossular (Hgr) on vein margin (×20; G: RL, H: PPL).

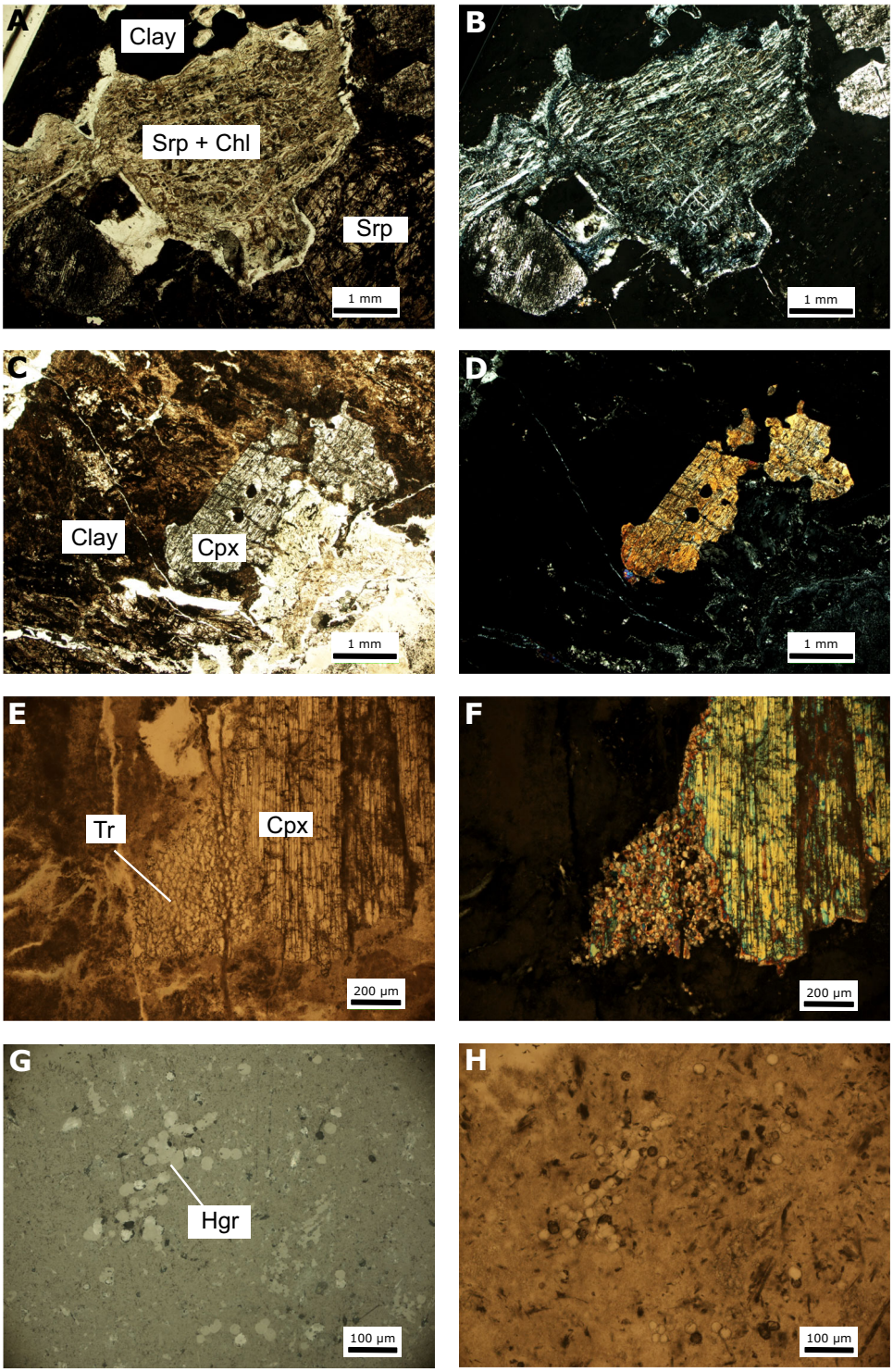

Figure F13. Pegmatitic gabbro, Hole BA4A. **A.** Section 11Z-4. **B, C.** Vein with prehnite (Prh), serpentine (Srp), and carbonate (Carb; undifferentiated) (11Z-4, 22–26 cm, 29.2 m; ×2.5; B: PPL, C: XPL).

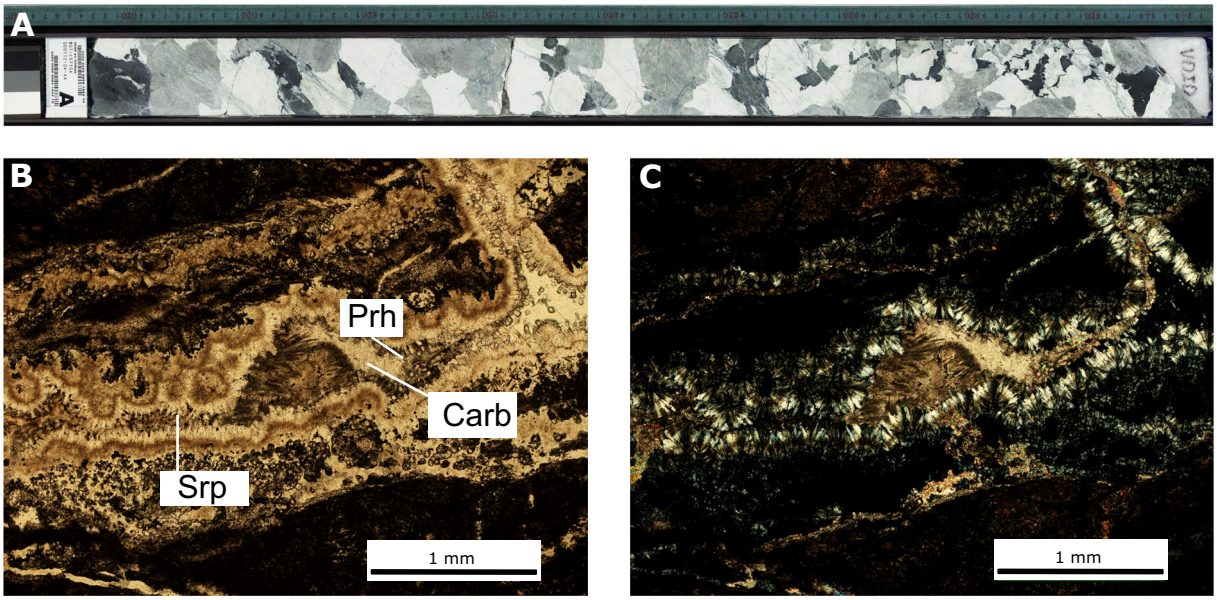

Figure F14. Highly altered gabbros, Hole BA4A. **A, B.** Altered clinopyroxene (Cpx) (19Z-3, 40–42 cm; 40.3 m, ×10; A: PPL, B: XPL). **C, D.** Clinopyroxene altered to prehnite (Prh) (84Z-4, 14–17 cm; 227.2 m; ×2.5; C: PPL, D: XPL). **E, F.** Clinopyroxene altered to tremolite and chlorite (Tr + Chl) with prehnite on the margin (84Z-4, 14–17 cm; 227.2 m; ×2.5; E: PPL, F: XPL).

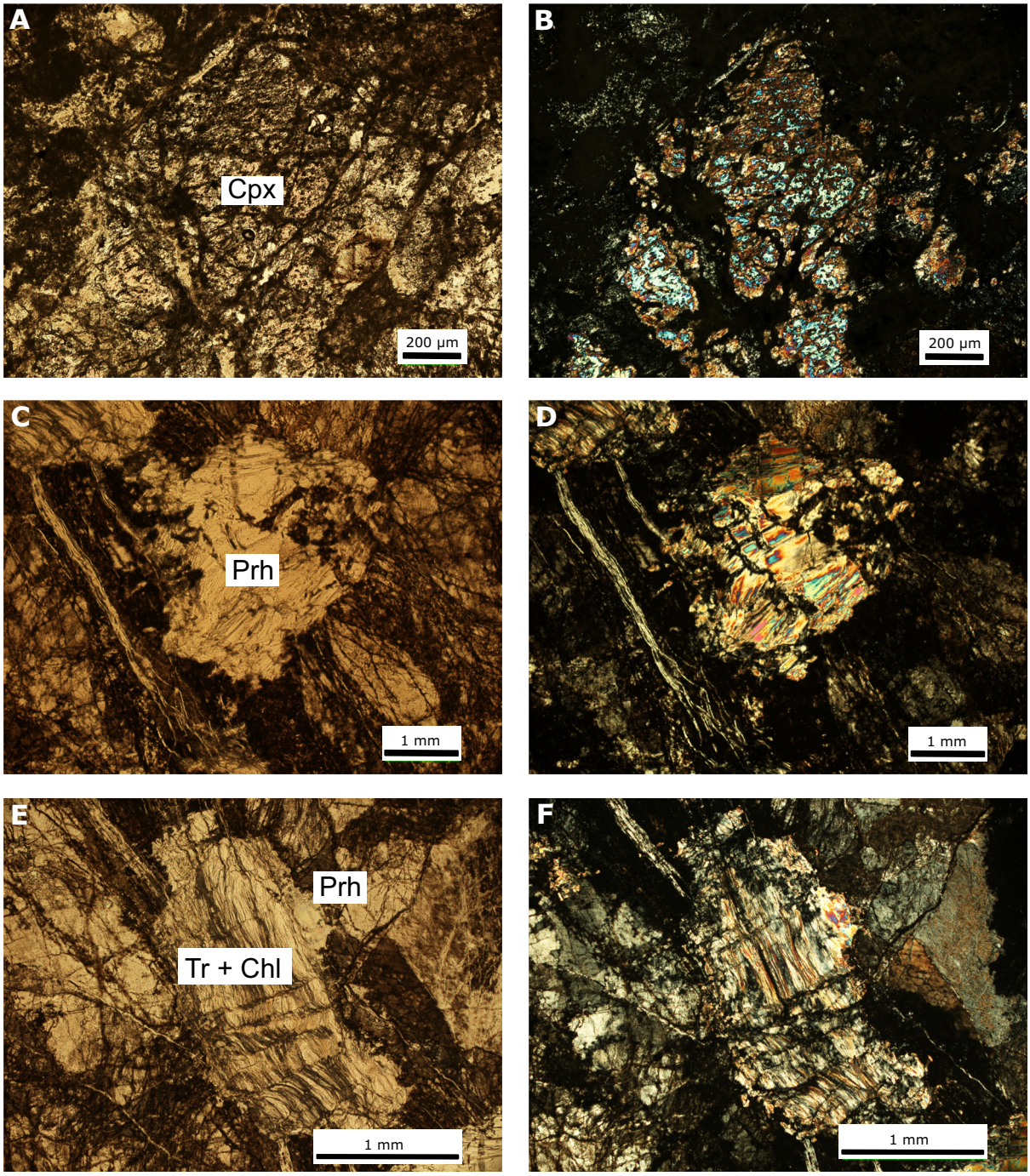

Figure F15. Features of the most extremely altered gabbros, Hole BA4A. **A**, **B.** Titanite (Ttn) (95Z-2, 16–18 cm; 258.7 m; ×5; A: PPL, B: XPL). **C**, **D.** Prehnite (Prh) in a vein (15Z-2, 87–90 cm; 31.2 m; ×10; C: PPL, D: XPL). **E**, **F.** Zoned vein with carbonate (Carb; undifferentiated) center (15Z-2, 87–90 cm; 31.2 m; E: PPL, F: XPL). Srp = serpentine.

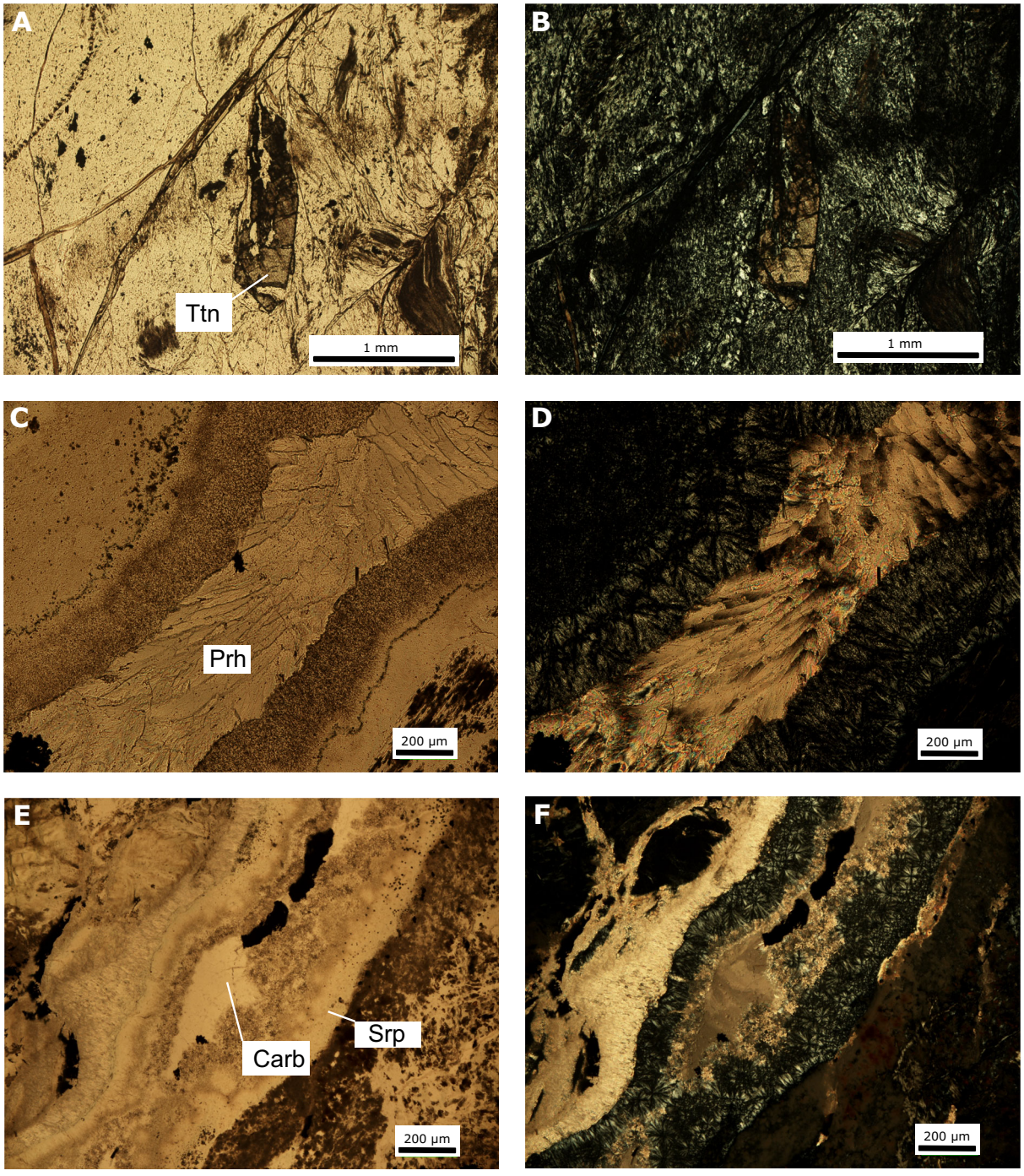

Figure F16. Relatively fresh olivine gabbro, Hole BA4A (40Z-1, 54–56 cm; 102.2 m). **A, B.** Equigranular grains in olivine (Ol) gabbro (×2.5; A: PPL, B: XPL). Pl = plagioclase, Cpx = clinopyroxene. **C, D.** Alteration zones between grains (×10; C: PPL, D: XPL). Srp = serpentine. **E, F.** Pale brown amphibole (Amp) in interstitial textural setting (×5; E: PPL, F: XPL).

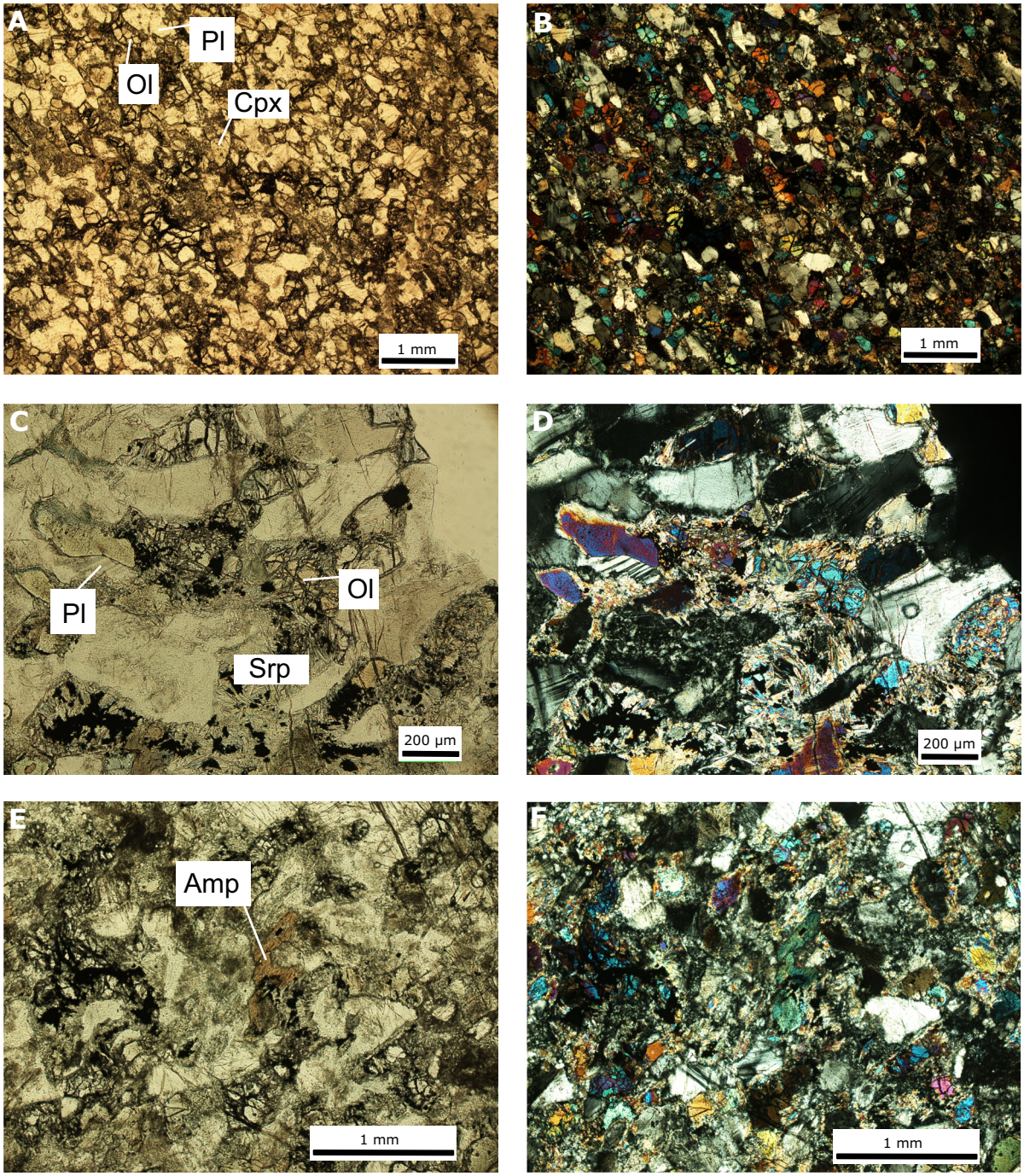

Figure F17. Olivine gabbro, Hole BA4A (RL). **A–D.** Sample 40Z-1, 54–56 cm (102.2 m; ×20). (A) Magnetite (Mag) in altered olivine. (B) Sulfides (Sulf; undifferentiated) in magnetite associated with alteration. (C) Composite sulfides associated with alteration. Pn = pentlandite. (D) Magnetite and native copper (Cop) included in pale brown amphibole (Amp) (see Fig. F16). **E.** Fractured chalcopyrite (Cp) and associated alteration phase with vein (22Z-4, 79–82 cm; 50.6 m; ×20). **F.** Magnetite and scattered sulfides in the vicinity of hydrogarnet-bearing vein in highly altered olivine gabbro (32Z-2, 22–26 cm; 78.7 m; ×20).

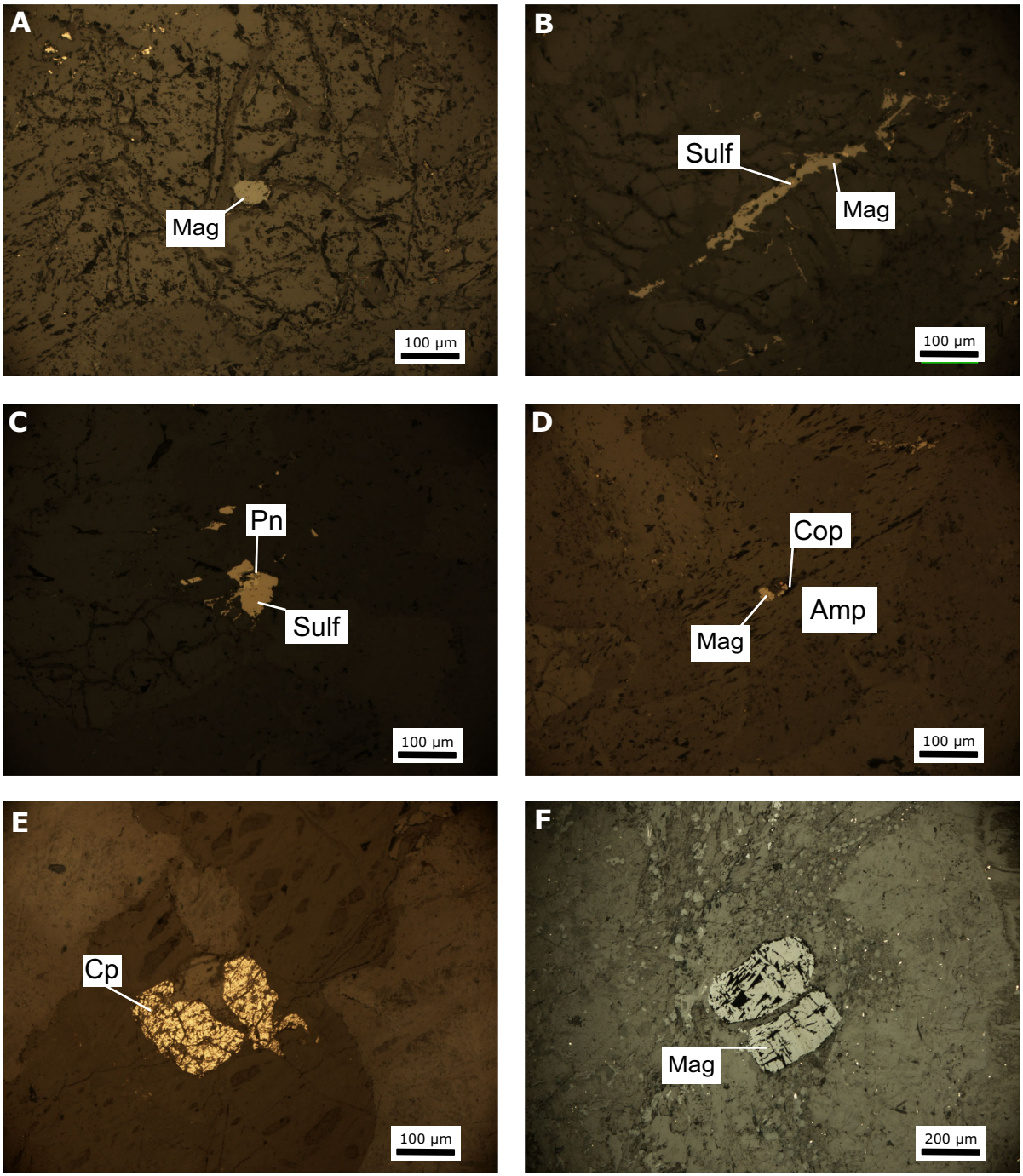

Figure F18. Pseudomorphically altered olivine gabbros, Hole BA4A. **A–D.** Sample 22Z-4, 79–82 cm (50.6 m). (A, B) Distribution of pseudomorphically altered alteration (×2.5; A: PPL, B: XPL). Srp + Chl = serpentine and chlorite. (C, D) Minimal disruption of pseudomorphically altered texture adjacent to a small fault in microgabbro (×2.5; C: PPL, D: XPL). Cpx = clinopyroxene. **E, F.** Tremolite (Tr) in drag fold on a fault and on the margin of a clinopyroxene grain (95Z-1, 8–10 cm; 257.8 m; ×5; E: PPL, F: XPL).

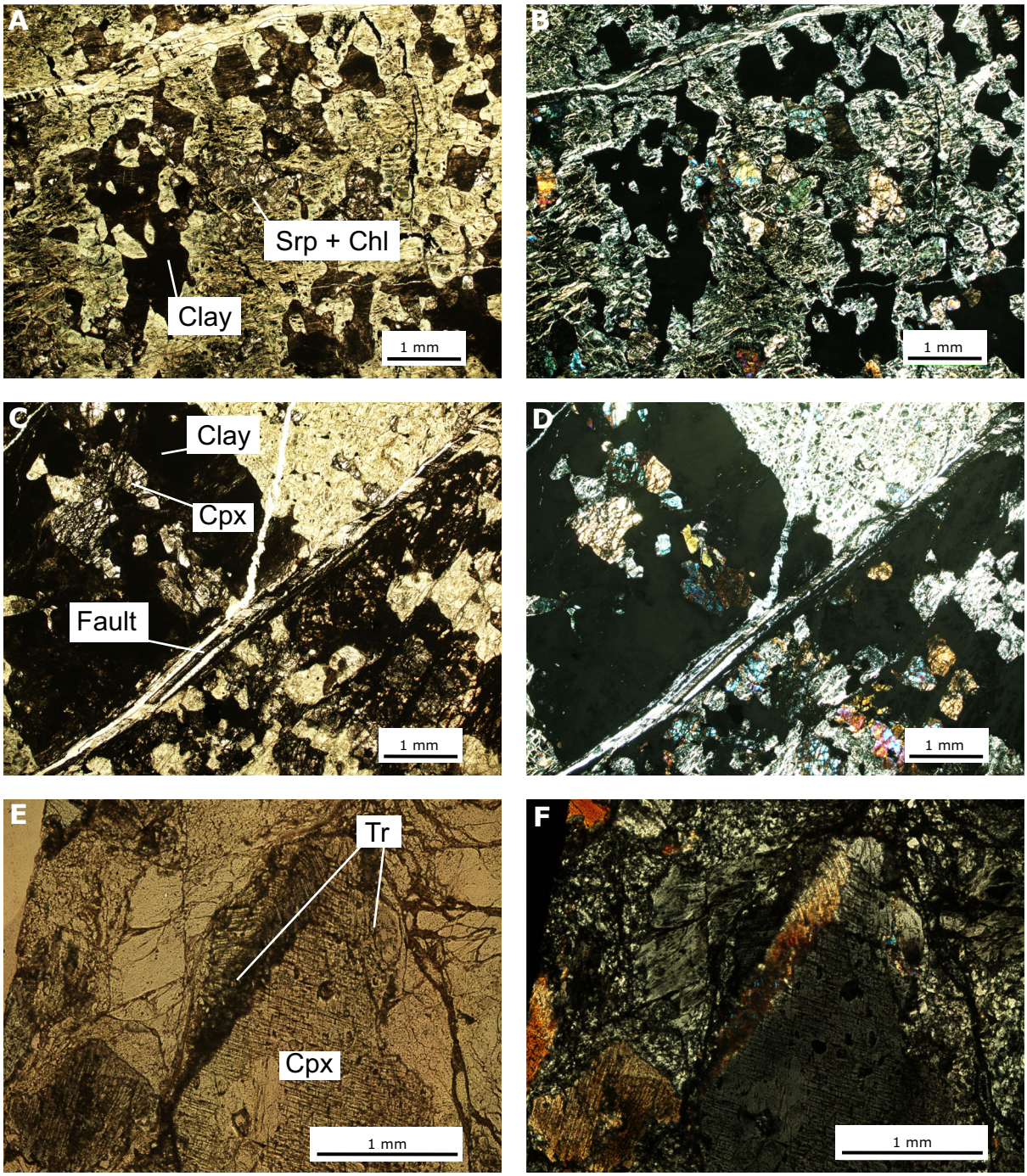

Figure F19. Highly altered olivine gabbros, Hole BA4A (32Z-3, 14–17 cm; 79.5 m). **A, B.** Hydrogrossular (Hgr)-bearing vein with serpentine + chlorite (Serp + Chl)- and prehnite (Prh)-bearing alteration zone on its margin (×10; A: PPL, B: XPL). **C, D.** Hydrogrossular on vein margin (×20; C: PPL, D: RL). Mag = magnetite. **E, F.** Folding of well-developed foliation (×5; E: PPL, F: XPL).

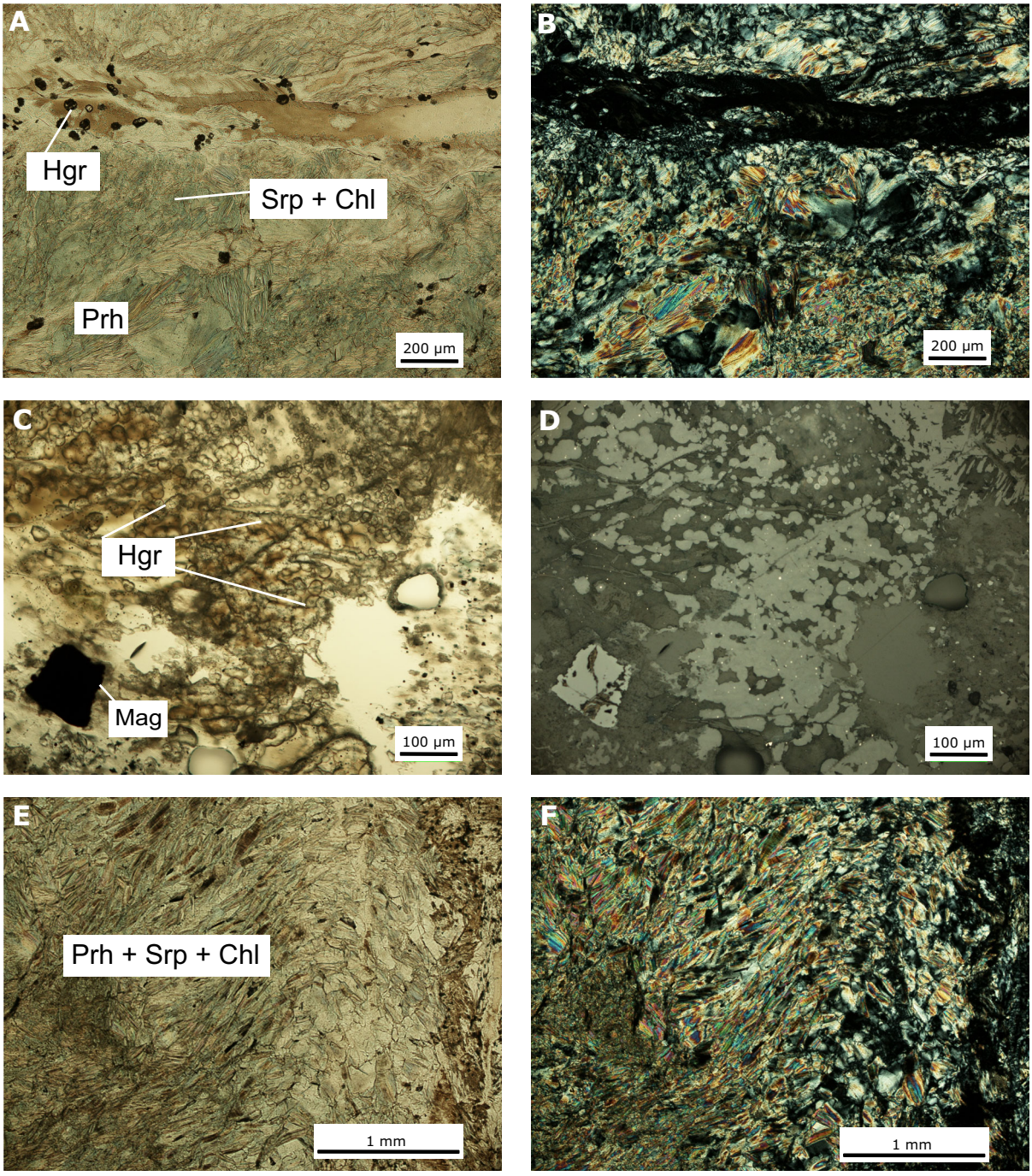

Figure F20. Textures in clinopyroxene (Cpx)-dominated dikes, Hole BA4A. **A, B, E, F.** Sample 71Z-2, 5–10 cm (189.7 m; ×5). **C, D, G, H.** Sample 51Z-1, 5–9 cm (134.8 m; ×2.5). (A, B) Strain zones in clinopyroxene (A: PPL, B: XPL). (C, D) Olivine inclusions in clinopyroxene (C: PPL, D: XPL). Srp + Chl = serpentine + chlorite. (E, F) Tremolite (Tr) needles on the margin of clinopyroxene (E: PPL, F: XPL). (G, H) Serpentine fabric wrapping around olivine grain with consequent destruction of the mesh texture (G: PPL, H: XPL).

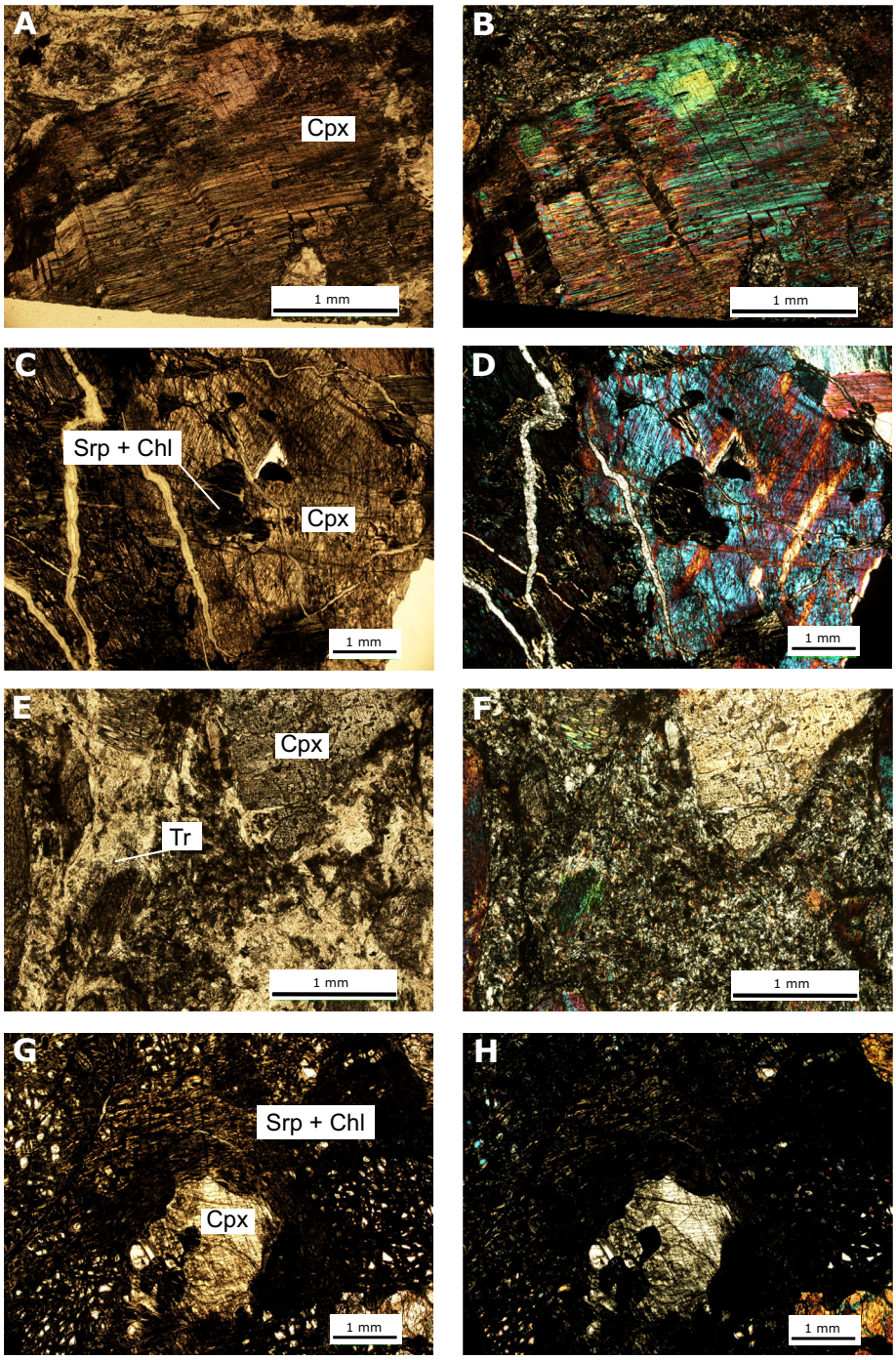

Figure F21. Altered clinopyroxene (Cpx)-dominated dikes, Hole BA4A (RL). **A–C.** Sample 71Z-2, 5–10 cm (189.7 m; ×20). (A) Magnetite (Mag) inclusions in clinopyroxene. (B) Native copper (Cop) in vein. (C) Native copper included in and associated with hematite (Hem). D. Pyrite (Py) after magnetite (51Z-1, 5–9 cm; 134.8 m; ×20).

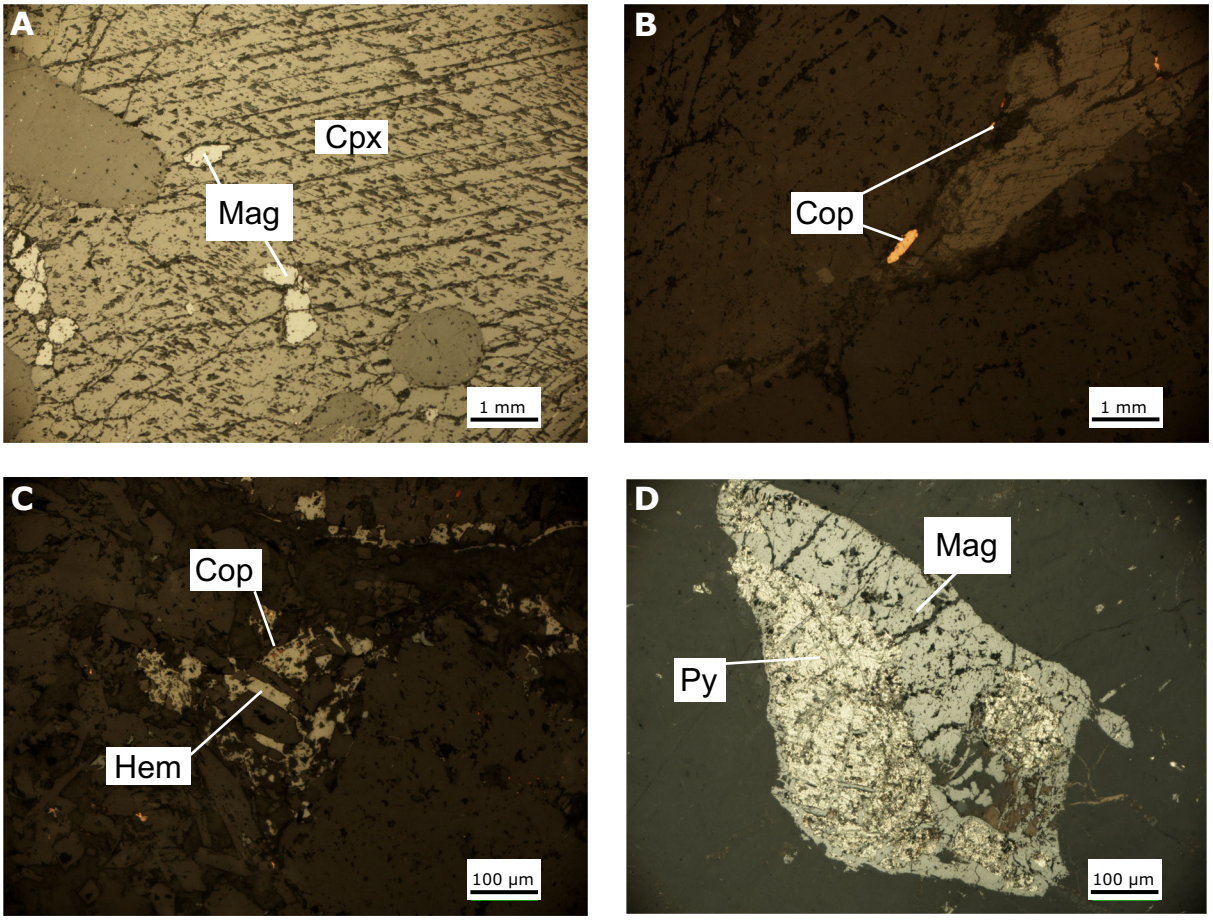

Figure F22. Clinopyroxene dissemination, Hole BA4A (48Z-1, 38–42 cm; 126.1 m). **A, B.** Black alteration on clinopyroxene (Cpx) (×2.5; A: PPL, B: XPL). Srp + Chl = serpentine + chlorite. **C, D.** Completely altered clinopyroxene (C: ×10; PPL; D: ×2.5; XPL). E, F. Variation in color in serpentine mesh cores (×10; E: PPL, F: XPL).

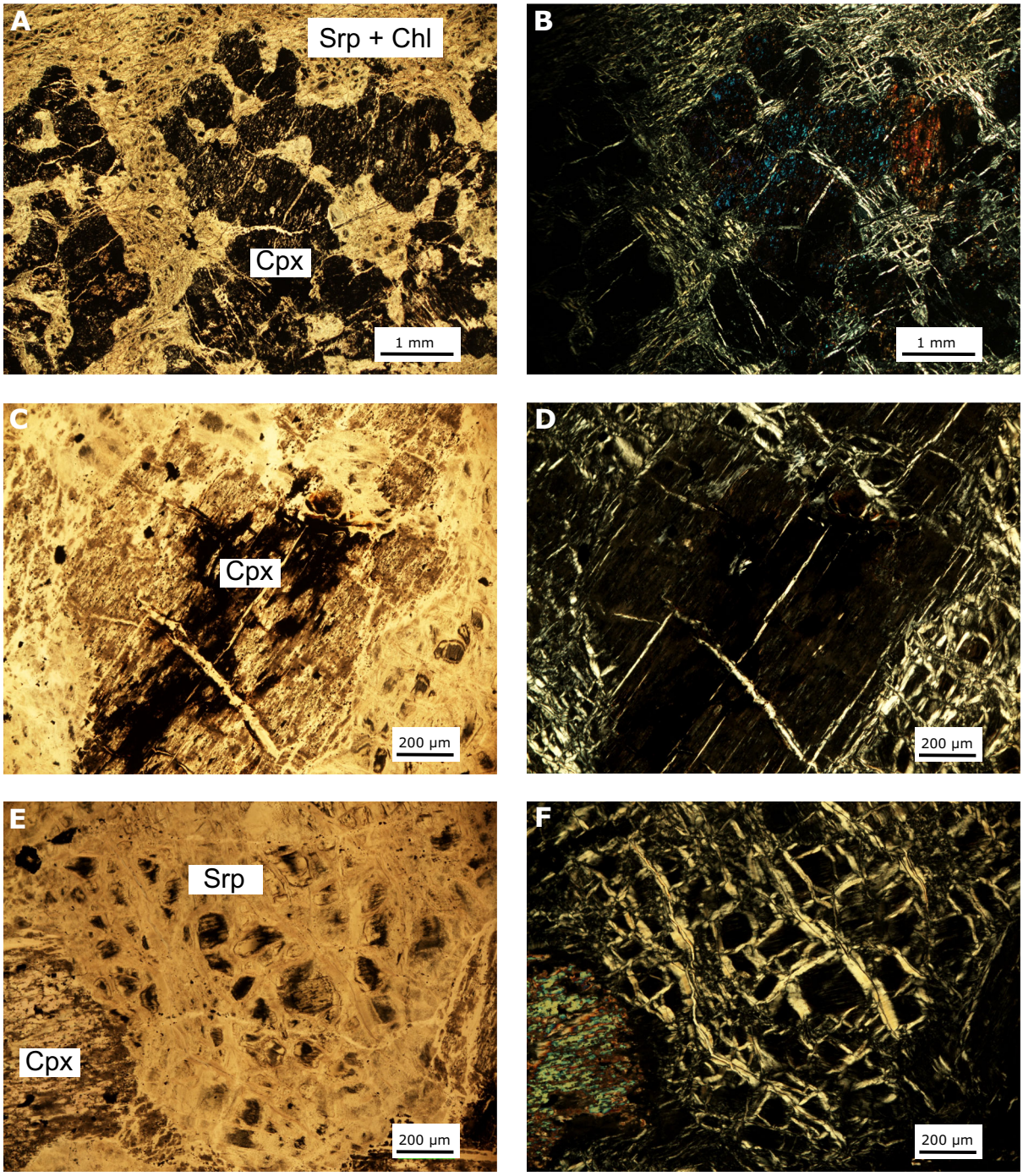

Figure F23. Disseminated clinopyroxenites, Hole BA4A (48Z-1, 38–42 cm; ×20; RL). **A.** Magnetite (Mag) in highly altered area of olivine. **B.** Chalcopyrite (Cp) rimmed by magnetite adjacent to vein.

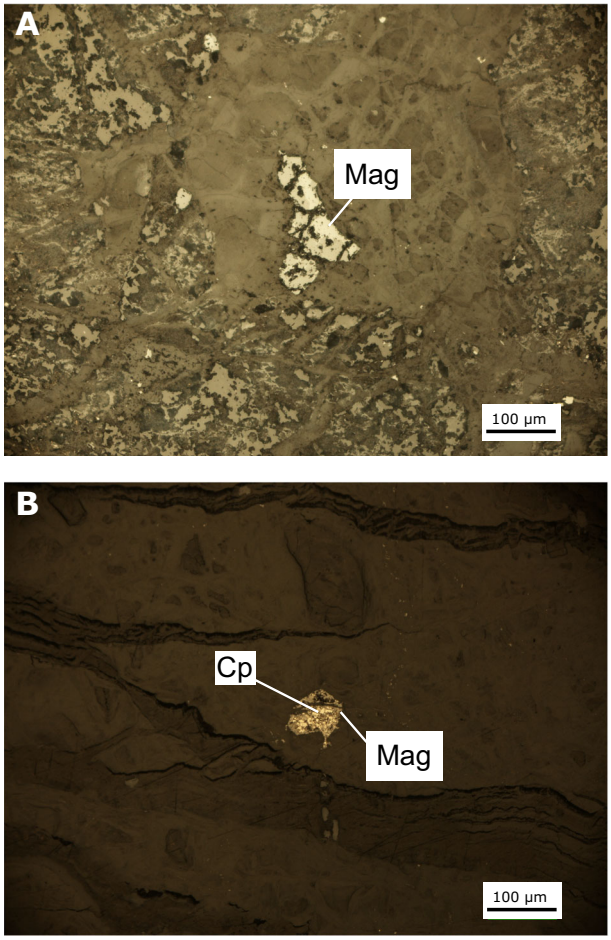

Figure F24. Breccia units, Hole BA4A. **A.** Section 32Z-2 (78.5 m). **B.** Section 77Z-4 (208.9 m). **C.** Sample 77Z-4, 10–12 cm (209.1 m; PPL). **D–G.** Sample 77Z-4, 58–61 cm (209.5 m; PPL). (E, F) Vein with xonotlite (Xon) fibers (×5; E: PPL, F: XPL). (G) Altered olivine clast or crystal showing zoning from serpentine (Srp)-rich core to serpentine + chlorite (Chl) + magnetite (Mag)-rich rim.

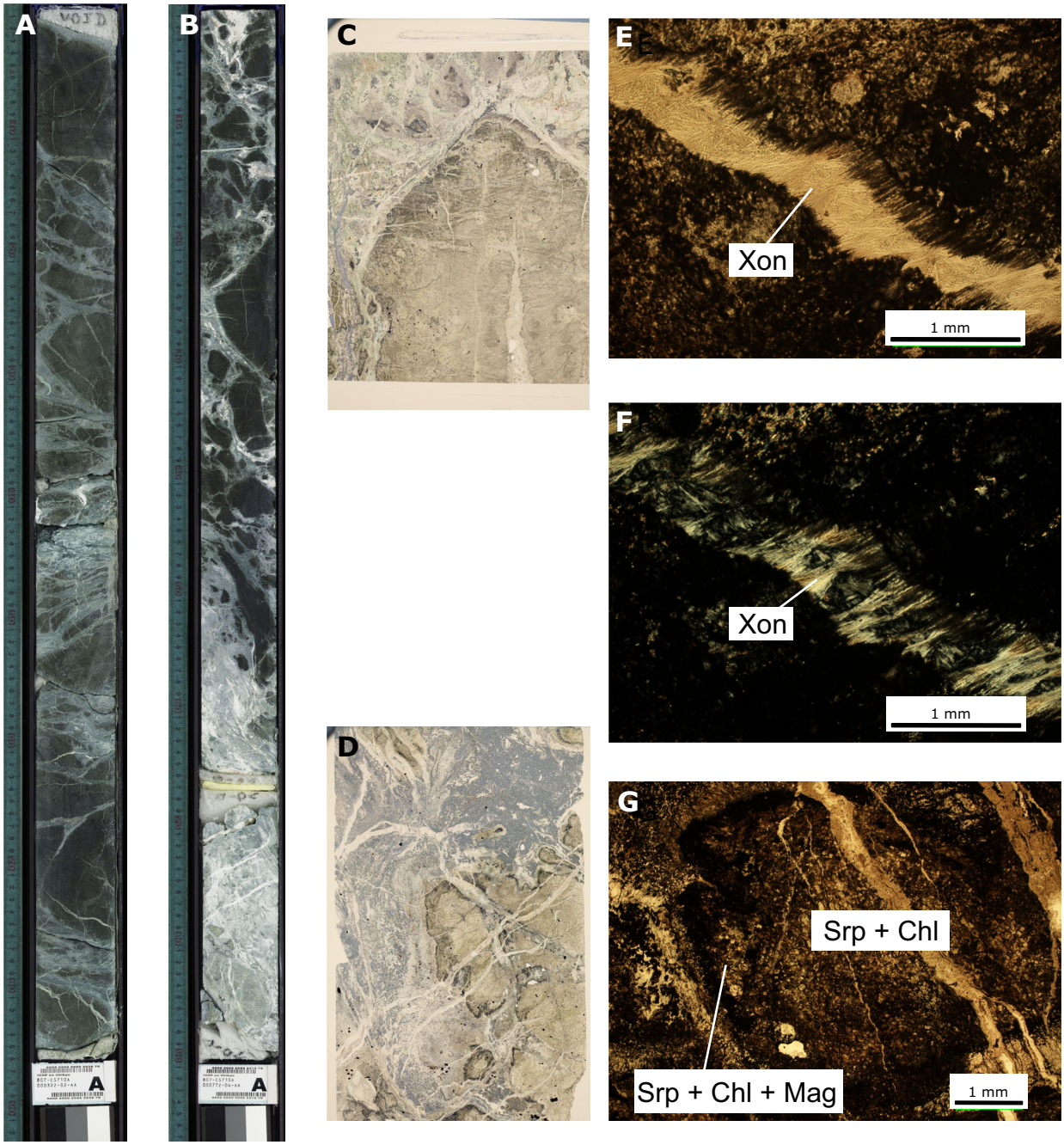

Figure F25. Deformed small-scale gabbroic intrusion unit, Hole BA4A. **A.** Section 95Z-3 (259.1 m). **B, C. E.** Sample 95Z-3, 36–38 cm (259.4 m) (PPL; field of view [FOV] = 48 mm). (C) Olivine (Ol) domain where fresh olivine mesh cores are preserved inside a serpentine + chlorite matrix (×2.5; PPL). (D) Calcium-rich domain, representing the altered gabbroic melt, inside dunitic domains. Large-zoned amphiboles are present in a matrix of fine-grained prehnite (Prh), amphibole (Amp), and talc (Tlc) (95Z-3, 46–48 cm; ×2.5; XPL). **E.** Zoned amphibole at the margin of a calcium-rich domain comprising a prehnite-rich outer area and a serpentine-rich inner area (×2.5; XPL).

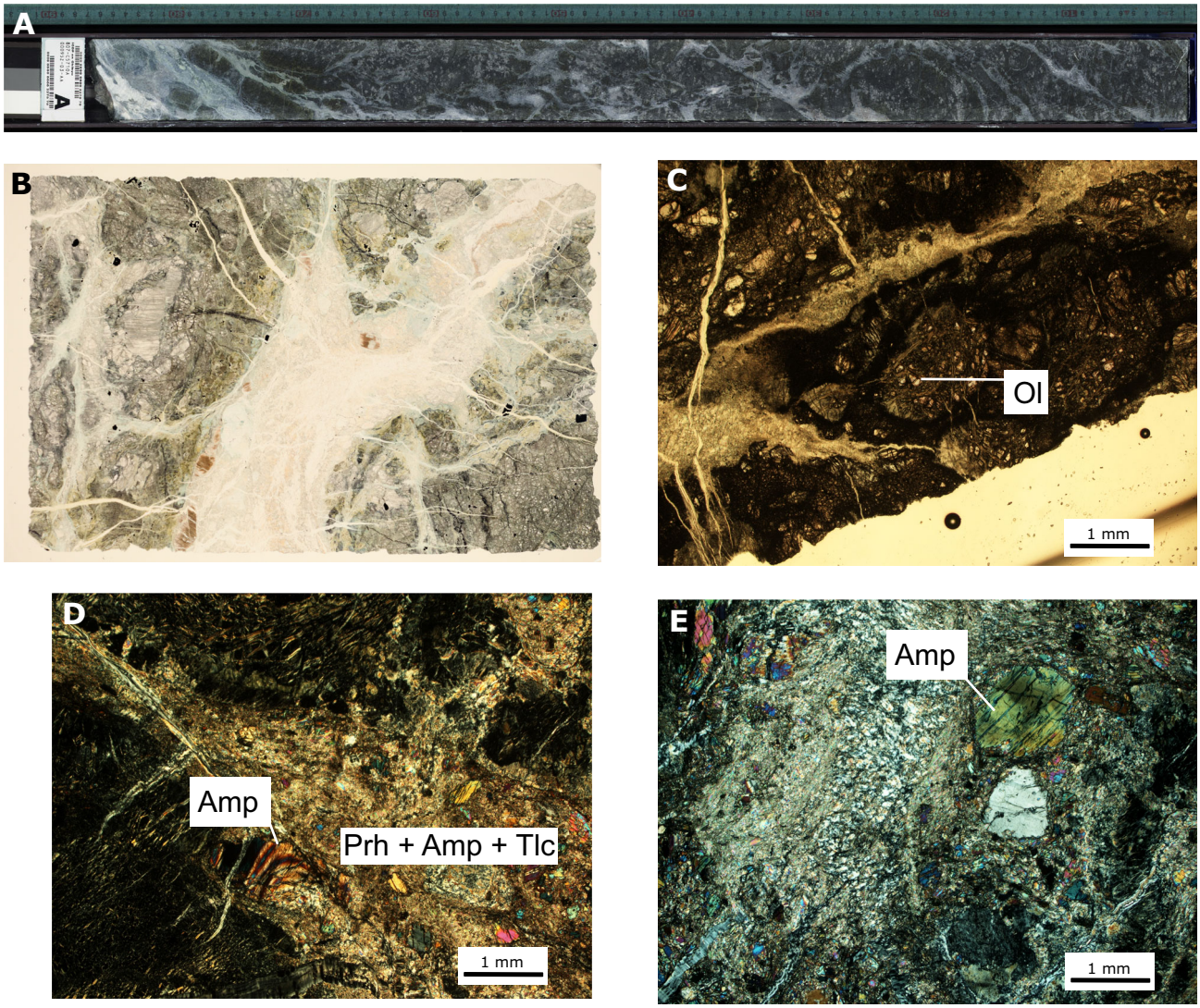

Figure F26. Lithologic summary, Hole BA4A.

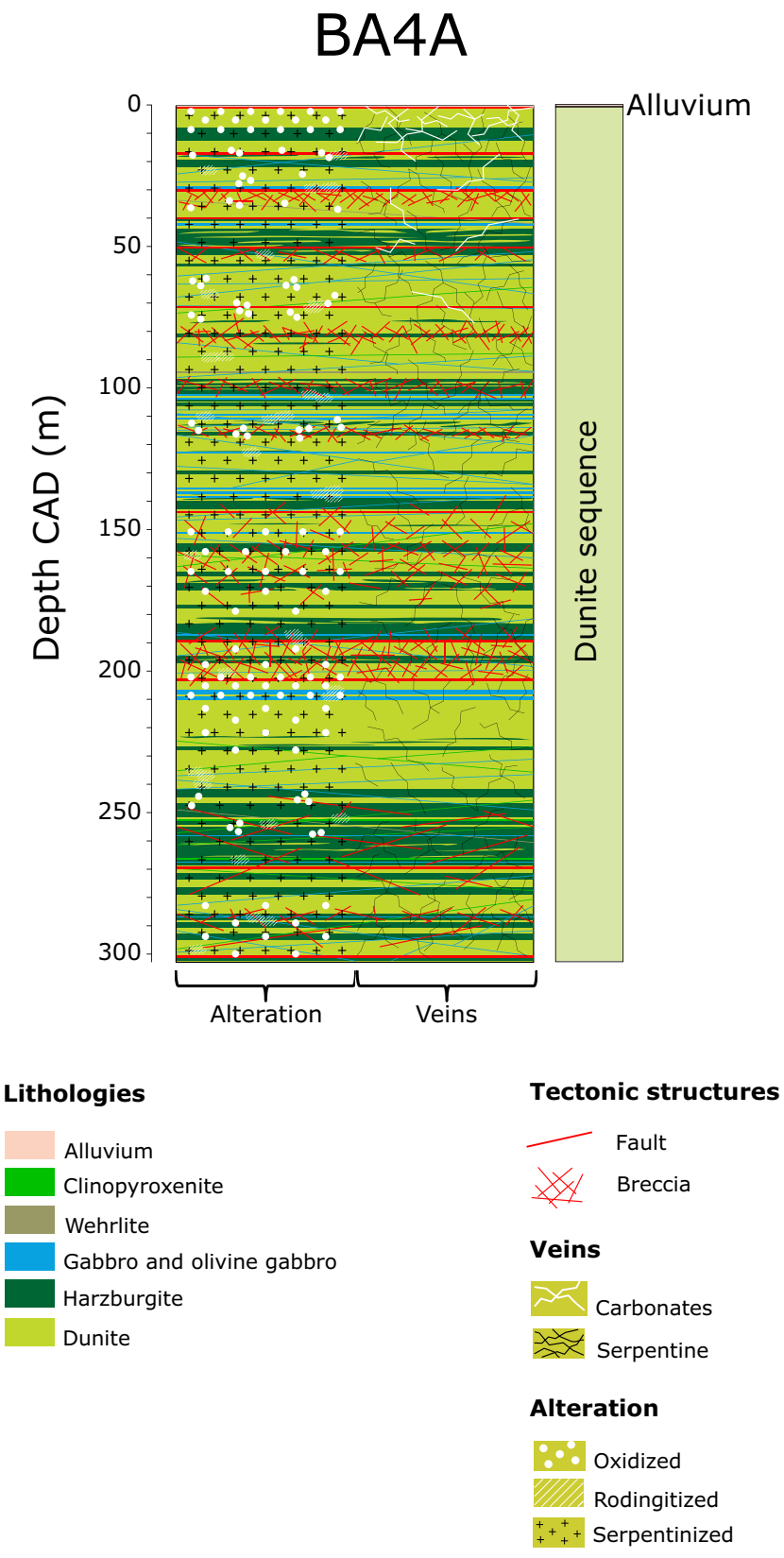

Figure F27. A. Described vein types, Hole BA4A. **B.** Type Ca1 (9.84–9.88 m). **C.** Type Ca2 (6.03–6.04 m). **D.** Type Ca3 (31.11–31.15 m). **E.** Type Cb (4.99–5.01 m). **F.** Type Sa (294.55–294.59 m).

A

- Carbonate-bearing serpentine
  - Ca1: Serpentinite (core) + carbonate (rim)
  - Ca2: Carbonate (core) + serpentine (rim)
  - Ca3: Carbonate (core) + waxy green serpentine (rim)
- Carbonate: Cb
- Serpentine
  - Sa: Black serpentine
  - Sb: Waxy green serpentine
  - Sc: Brown serpentine
  - Sd: Dark green serpentine
  - Se: Composite serpentine
  - Sf: White serpentine
  - Sg: Horrible green serpentine
- Xonotlite: X
- Others

B

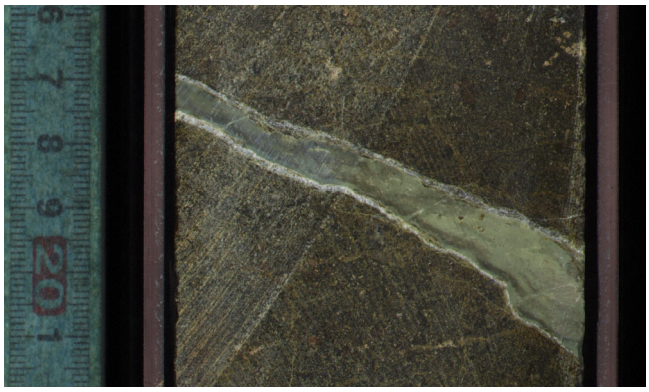

C

D

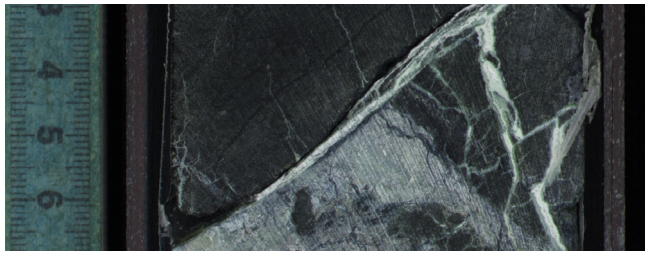

E

F

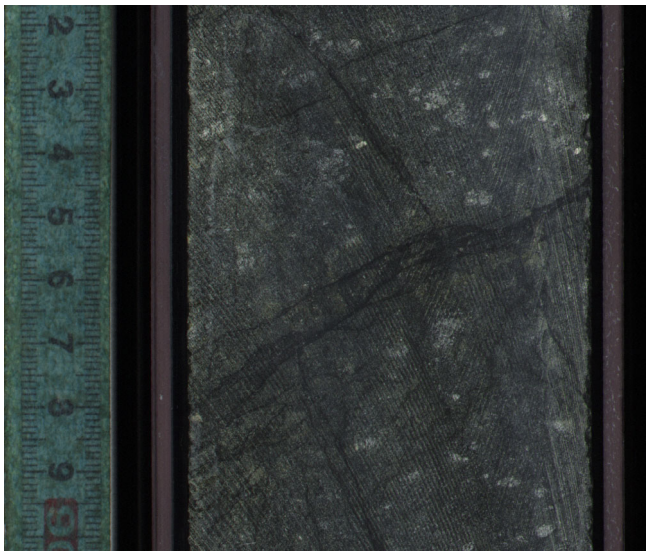

Figure F28. Vein types. **A.** Turtle-textured Type Sb vein (37.62–237.69 m). **B.** Type Sc (15.75–15.84 m). **C.** Type Sd (230.38–230.41 m). The thicker Sd vein is cut by thinner Sf veins. **D.** Composite white and black Type Se vein (162.63–162.74 m). **E.** Type Sf (297.35–297.42 m). **F.** Branched Type Sg (79.65–79.71 m). The thicker Sg vein is cut by thinner Sb veins. **G.** White Type X vein cutting a magmatic dike (207.48–207.53 m).

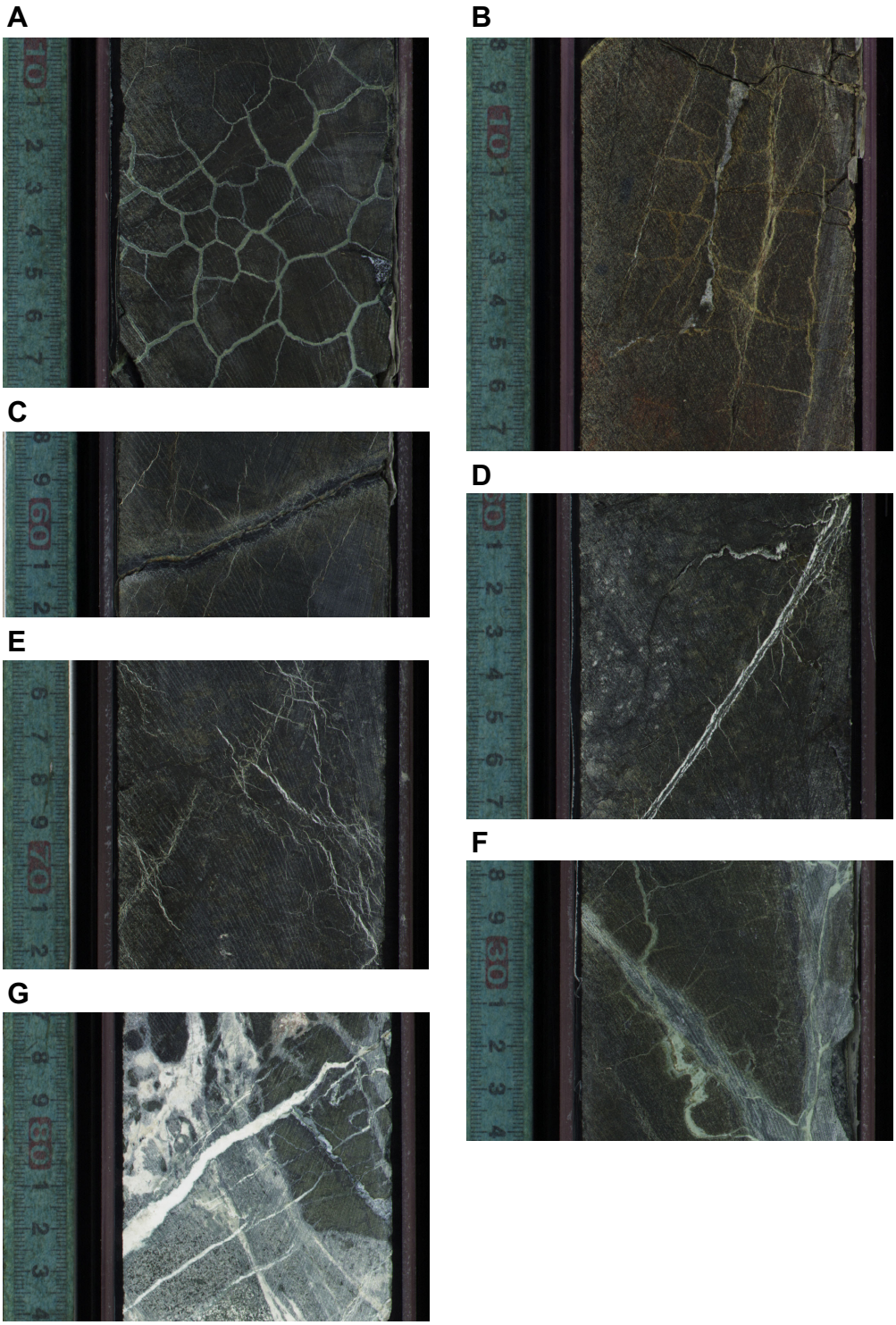

Figure F29. Selected examples of typical veins in dunite and harzburgite lithologies, Hole BA4A. **A.** Edge-shaped aggregates of two serpentine phases. **B.** Microcrystalline serpentine in the middle of two-phase serpentine vein. **C.** Serpentine veins with overlapping connectivity cut through the magnetite-bearing serpentine veins. D. Composite serpentine veins with twin calcite in the middle. **E.** Colloform calcite with serpentine (Srp) islands in the middle. **F.** Radial needle-like aggregate of xonotlite.

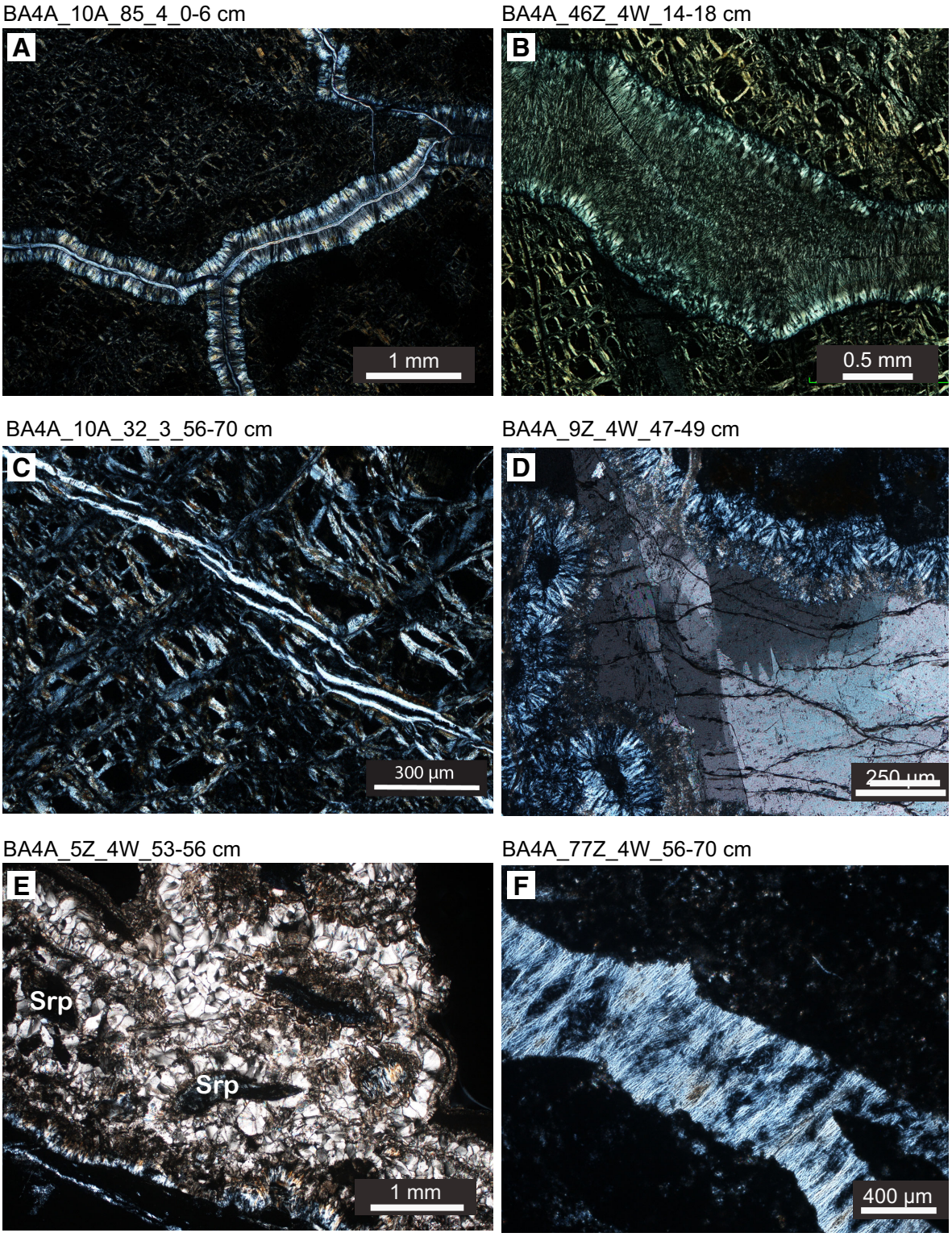

Figure F30. Opaque minerals, Hole BA4A (RL). **A.** Heazlewoodite vein. **B.** Chalcocite (Cct; blue-gray) replacing bornite (Bn; pinkish brown). **C.** High concentration of fine-grained magnetite in the middle of a serpentine vein cutting the mesh texture. **D.** Ferritchromite (Fe-Chr) alteration with medium reflectivity in the margins of chromite.

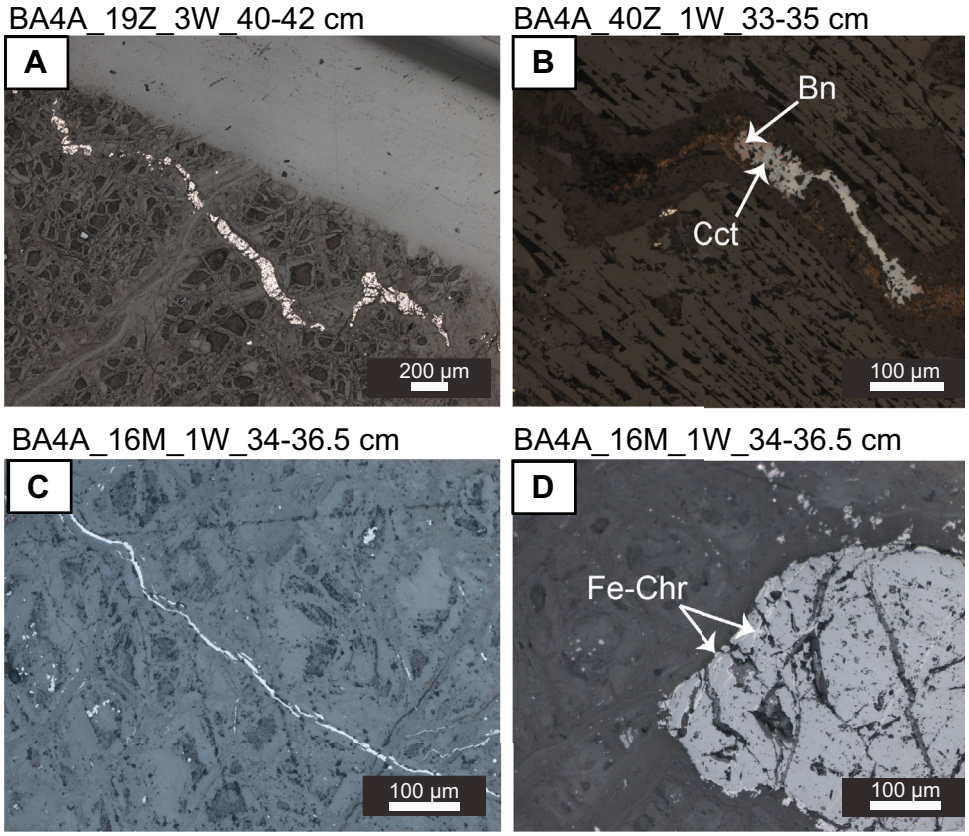

Figure F31. XRD patterns of powder samples collected at the locations marked by red crosses on core section images, Hole BA4A. Main diffraction peaks: S = serpentine, D = dolomite, M = magnesite, Cc = calcite, H = hydrogrossular, C = chlorite, P = phlogopite, X = xonotlite. **A, B.** Carbonate vein (Type Cb) mainly composed of magnesite (1Z-4, 42 cm). **C, D.** Vein with carbonate core (calcite) and serpentine rim (Type Ca2) (20Z-2, 7 cm). **E, F.** Serpentine vein (44Z-3, 22 cm). **G, H.** Composite vein (Type Se) with serpentine and hydrogrossular (43Z-1, 27 cm). **I, J.** Veins intensively mixed with magmatic features containing phlogopite (92Z-1, 61 cm). **K, L.** Xonotlite vein with minor serpentine (95Z-2, 45 cm).

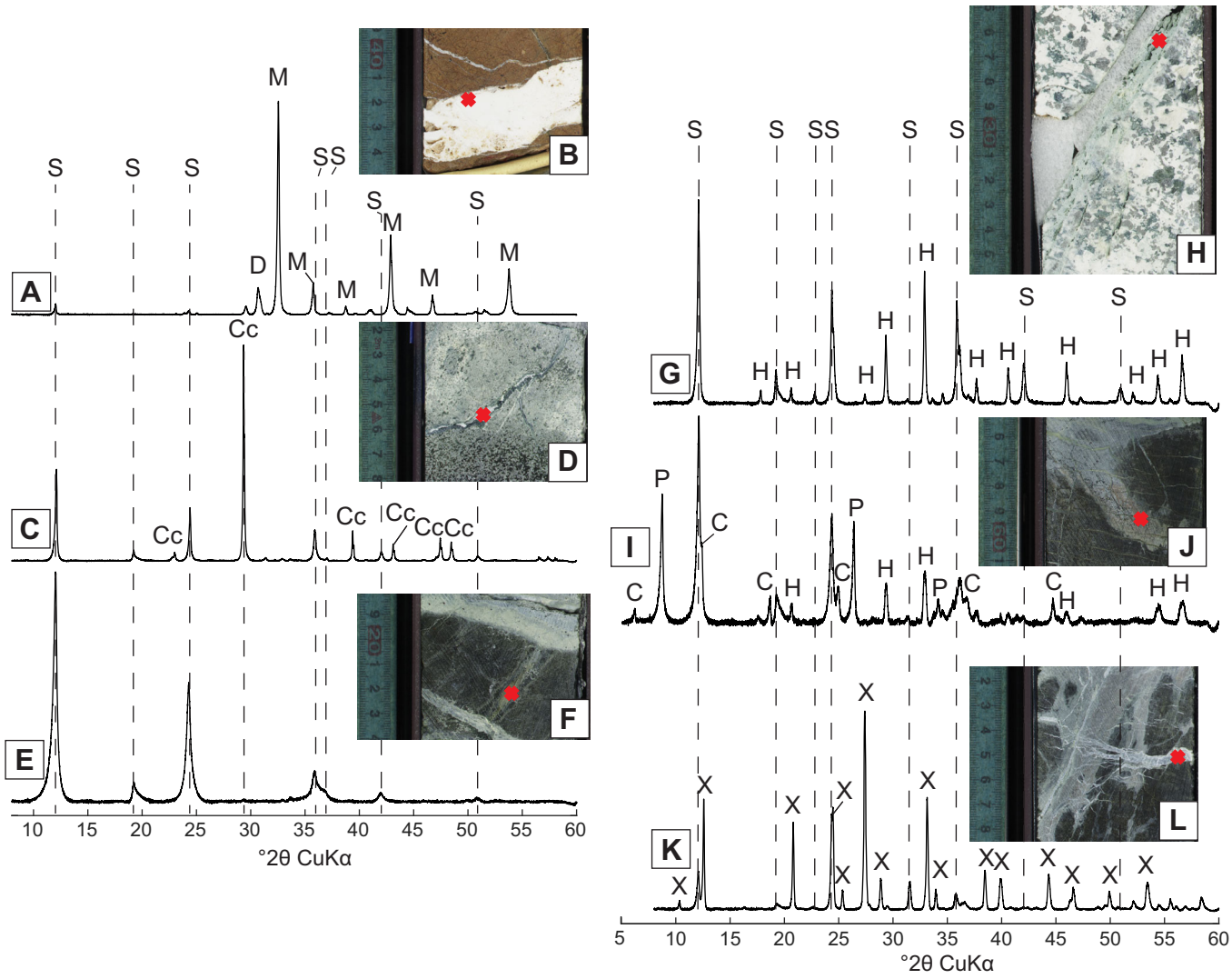

Figure F32. A. Observed vein types in core, Hole BA4A. **B.** Lithostratigraphy.

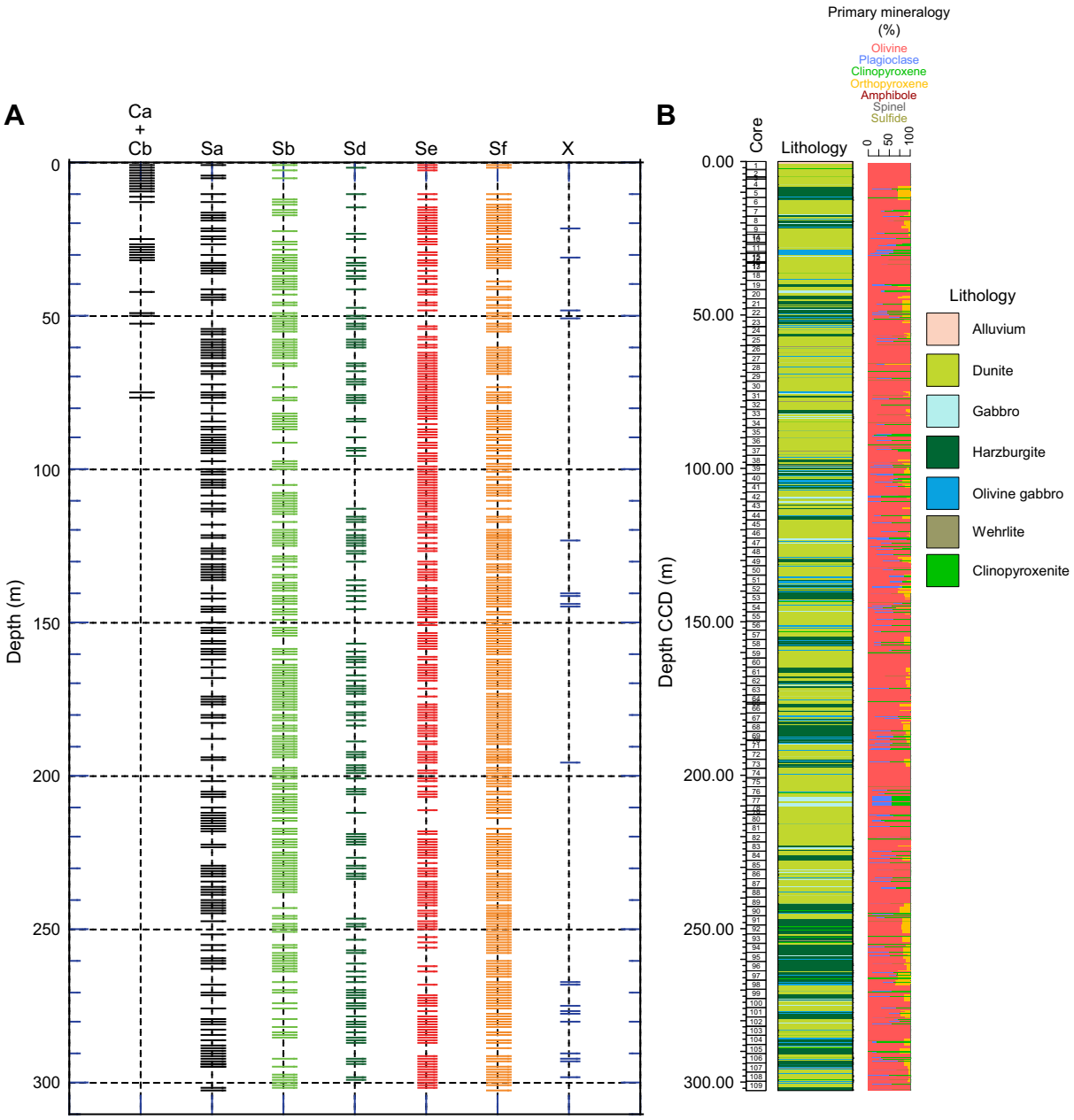

Figure F33. A–G. Specific vein types (average of 11 data points), Hole BA4A. **H.** Lithostratigraphy.

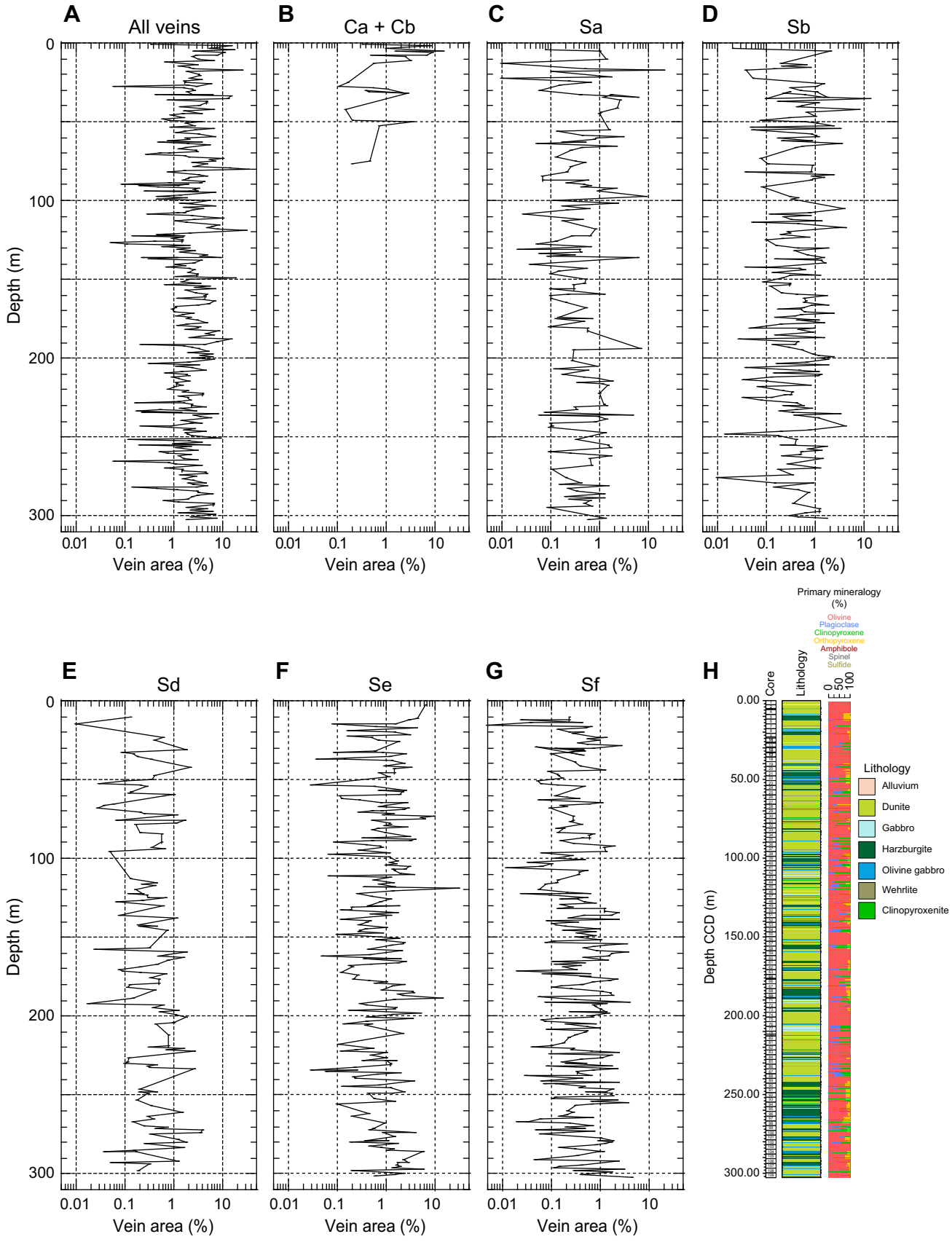

Figure F34. Crosscutting relationships of veins in core, Hole BA4A. Open symbols = carbonate-bearing veins. Labeled points correspond to all of the vein types for which a significant number of relationships were observed. Horizontal axis indicates the number of instances in which one of the many vein types was observed to cut one of the common types, and vertical axis represents instances in which one of the common types cuts them. For example, there are 3 observations of waxy green serpentine veins cutting carbonate-bearing veins and ~40 observations of carbonate veins cutting waxy green veins.

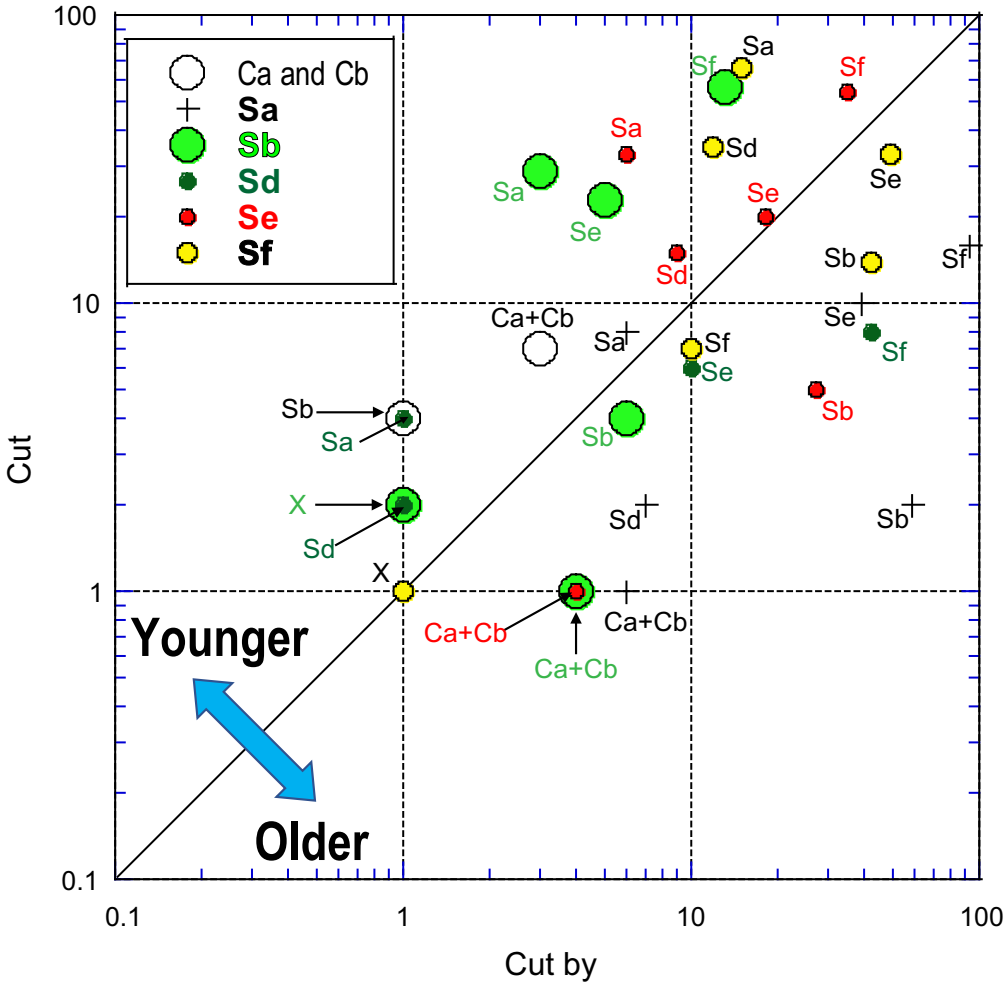

Figure F35. Intrusive texture, Hole BA4A. **A.** Largest pegmatitic gabbroic dike in the hole. **B.** Two different pyroxenite dikes. **C.** Pegmatitic dike grain size. **D**. Dunite/harzburgite contacts. **E.** Wehrlitic dike. **F.** Two different pyroxene dikes.

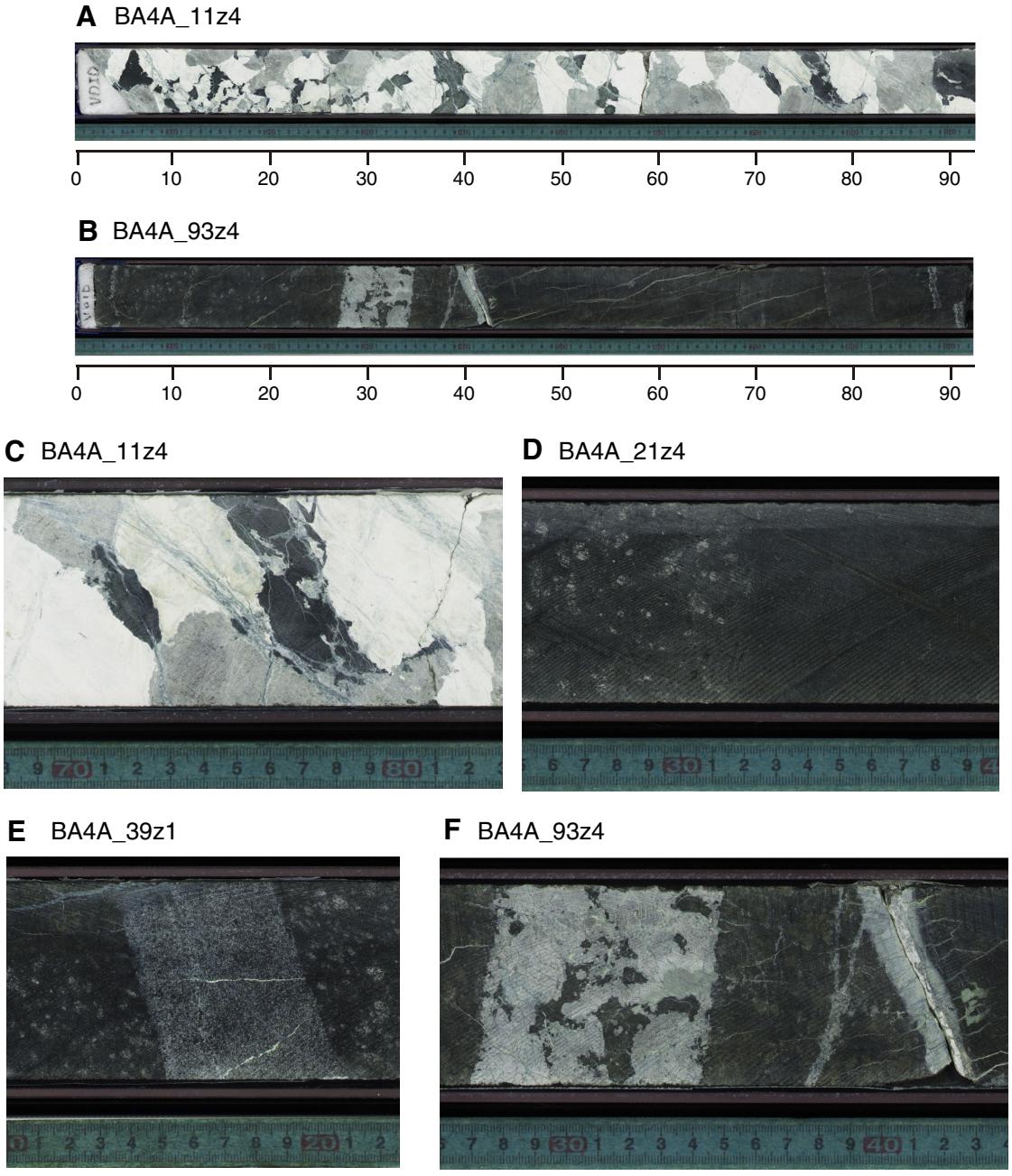

Figure F36. Locations and dip of magmatic contacts, Hole BA4A. Comparative graphic with the apparent thickness vs. depth, and rose diagram plots with statistics (using Stereonet 9.5; Cardozo and Allmendinger, 2013) of the dip angle for each type of contact.

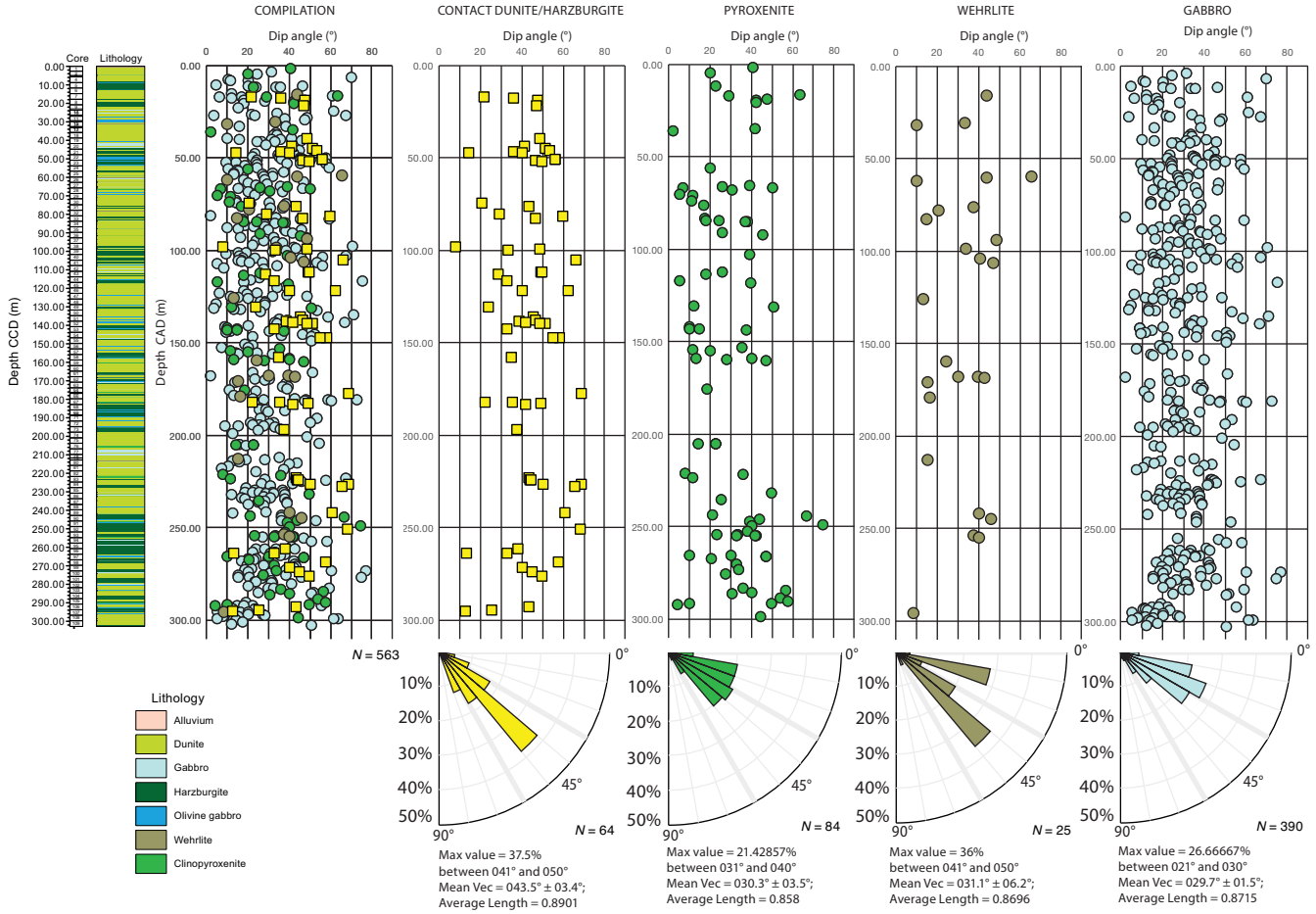

Figure F37. Locations and thicknesses of magmatic contacts, Hole BA4A. Histograms of dike thickness distribution appear to follow an approximately power-law scaling relation.

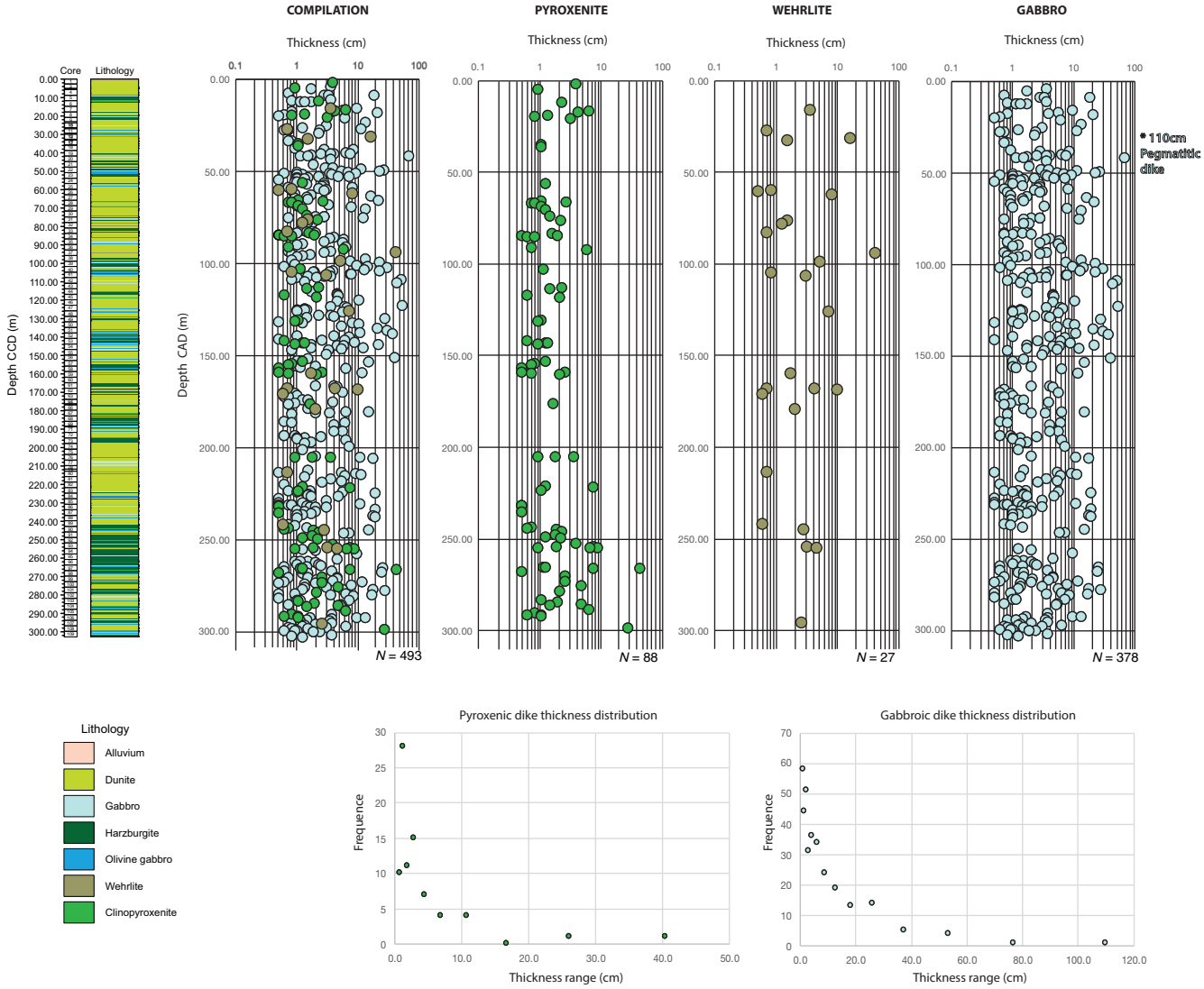

Figure F38. Peridotite fabric types defined by pyroxene geometry, Hole BA4A. **A.** Harzburgite with porphyroclastic texture defined by slightly elongated pyroxene. **B.** Harzburgite with protomylonitic texture defined by strongly elongated pyroxene. **C.** XCT image (0–40 cm) of slightly elongated pyroxenes (brighter color). **D.** XCT image (0–28 cm) of strongly elongated pyroxenes (brighter color). **E.** Texture differences. In interval 38Z-4, 69–71 cm, slightly elongated pyroxenes form porphyroclastic texture. In interval 53Z-1, 14–16 cm, strongly elongated pyroxenes form protomylonitic texture.

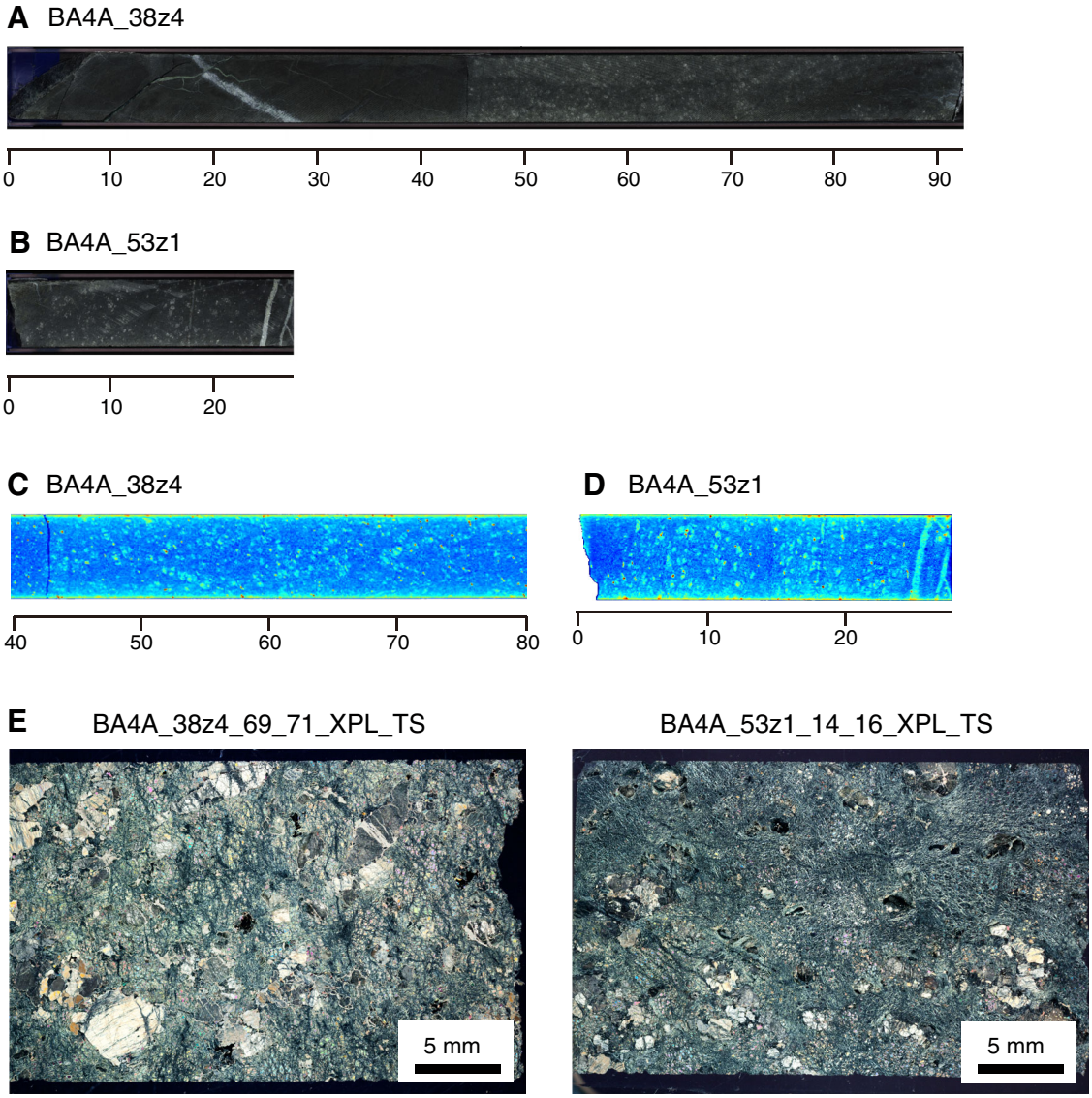

Figure F39. Dip angle calculated in crystal-plastic fabric (CPF) in dunites and harzburgites, Holes BA1B, BA3A, and BA4A.

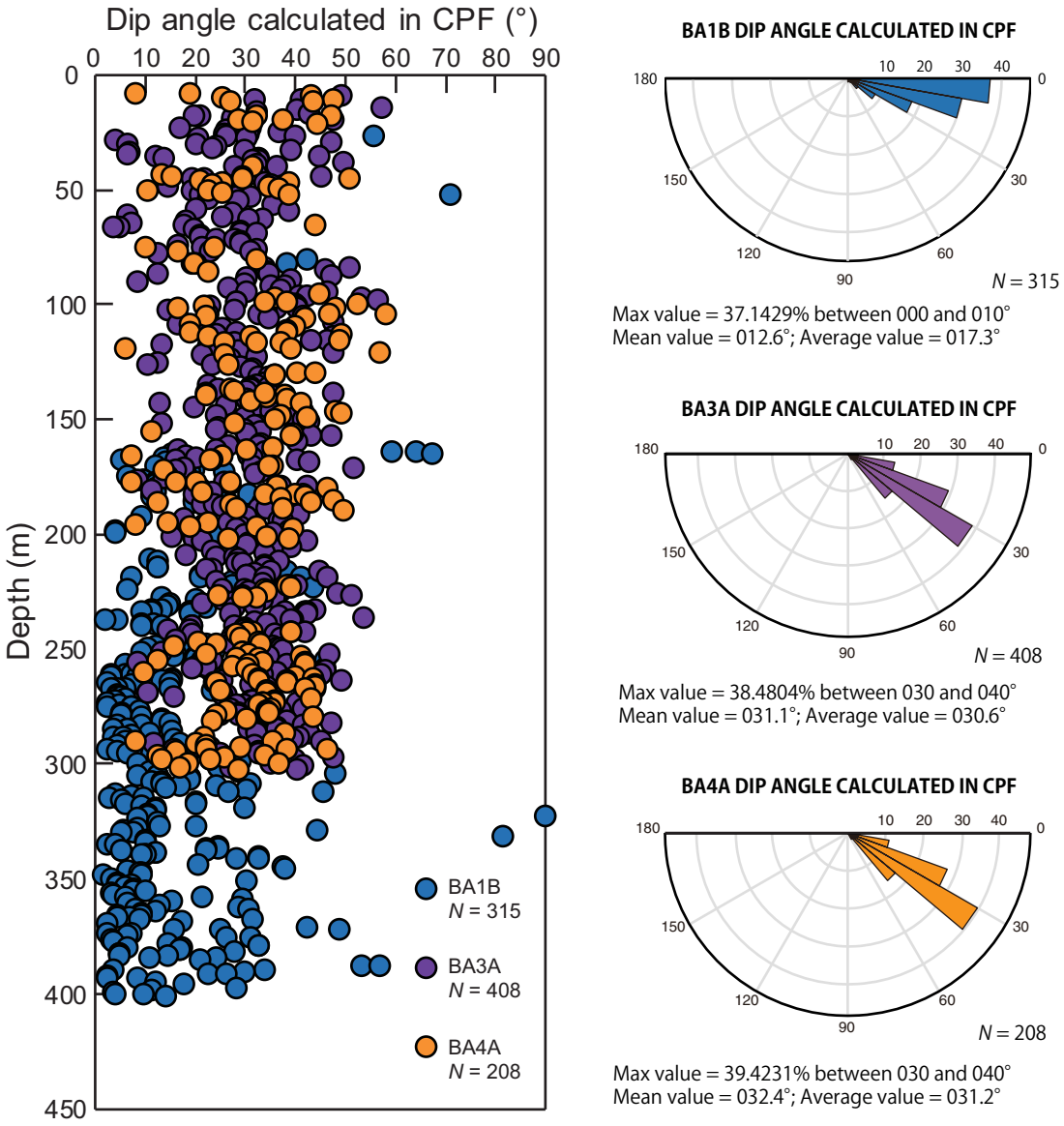

Figure F40. Collision between a largely unaltered clinopyroxene indenter grain (top center) with a partly chloritized grain (lower center), Hole BA4A. **A.** Chlorite-filled cleavage planes (dark elongated areas) of the indented grain were bent during the collision and seem to have developed a localized "fault-like" structure in the left part of the grain (arrow) (PPL). **B.** Crystal-plastic rotation reflected by a pronounced undulatory extinction. Note crystal-plastic deformation of the indenter grain near the grain contacts (arrow) (XPL).

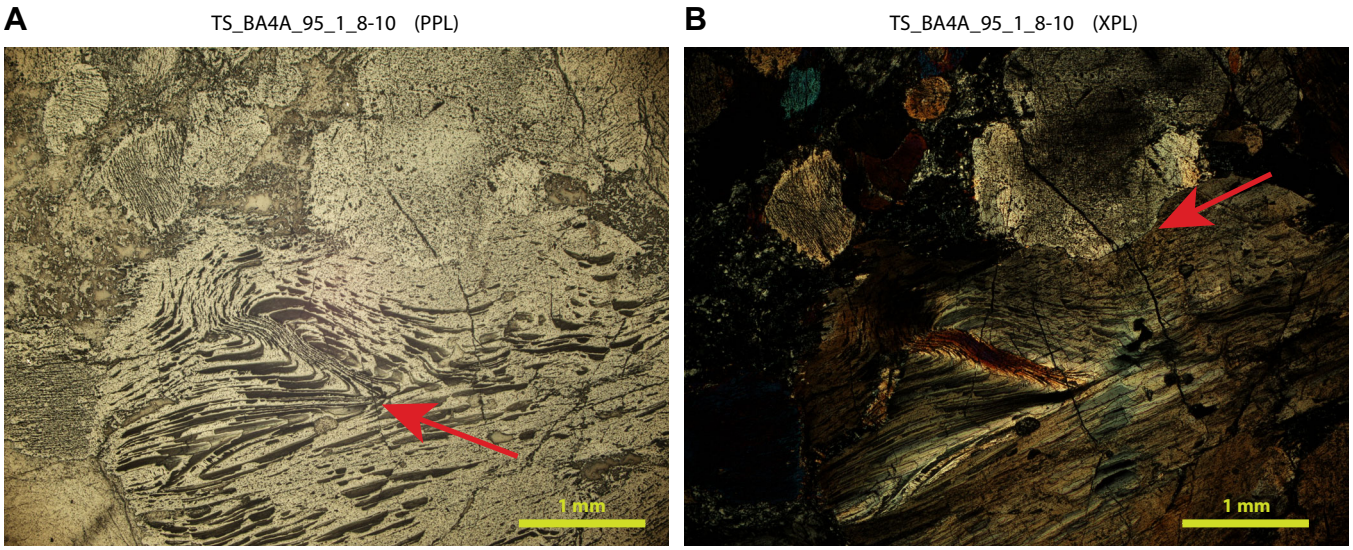

Figure F41. A. Locations and thicknesses of fault zones (red bars), Hole BA4A. The occurrence of fault zones correlates well with harzburgite-dominated sections. **B.** Thicknesses of damage zones. Note that where a feature crosses a discontinuous boundary between two sections of core, the two sides were logged as individual features because the relation between the two sections was not observed. **C.** Deformation intensity rank for each feature. Intensity increases from 1 to 5. **D.** Fracture and vein density rank. For full explanation of ranking procedures, see **Structural geology** in the **Methods** chapter.

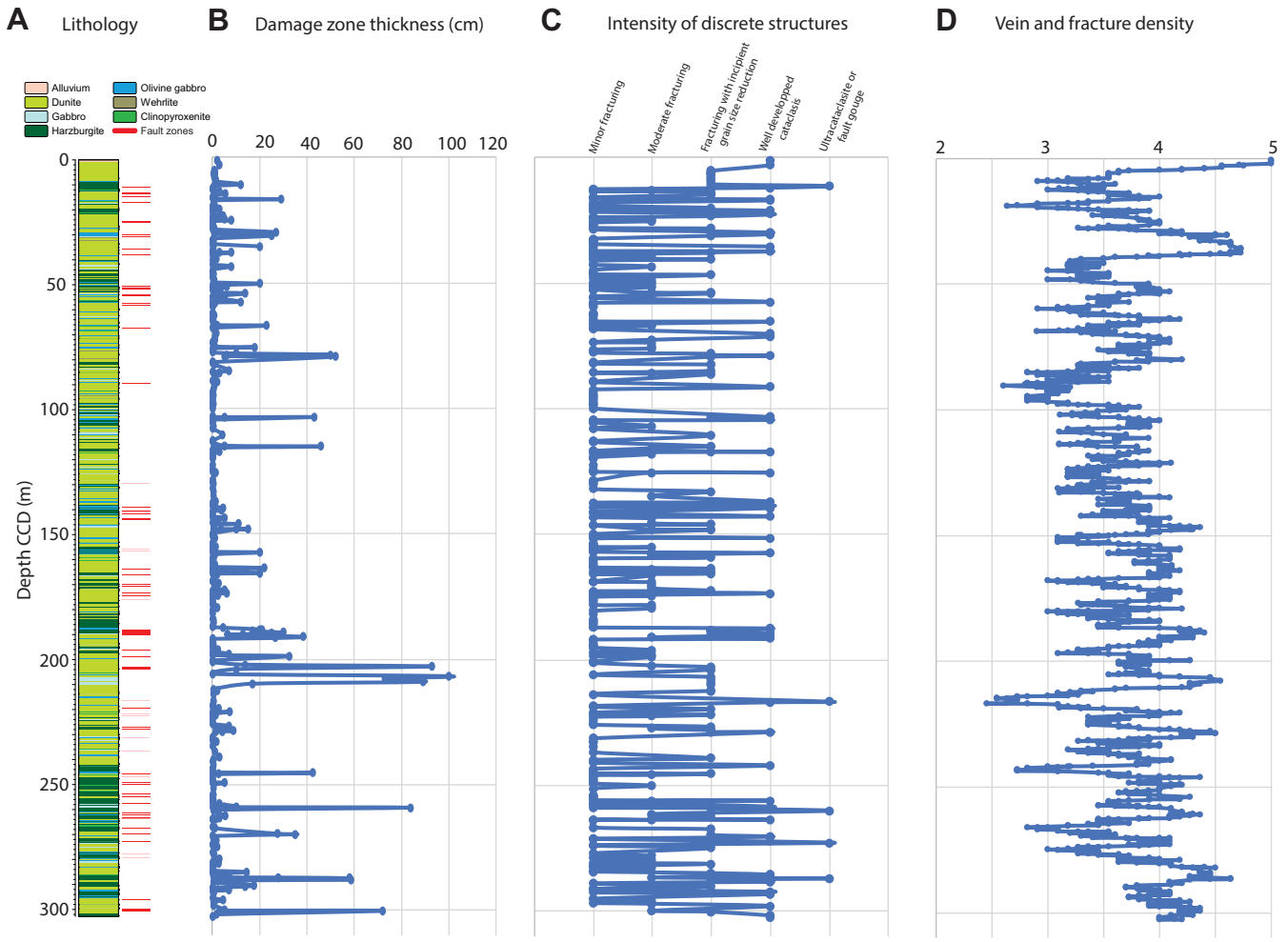

Figure F42. Deformation structure types, Hole BA4A. **A.** Altered gabbro dike cut by multiple fractures and offset along a slip plane. **B.** Typical fault zone characterized by a finite band of intense brittle deformation and cataclasis. **C.** Composite vein that has accommodated a small amount of shear. **D.** Narrow shear vein clearly offsetting a dike. In cases like this, slip probably occurred prior to vein mineralization. **E.** Wide, probably crystal-plastic shear zone displaying mylonitic texture with very fine grained, almost ultramylonitic fabric in the lower center and a greater number of porphyroclasts toward the upper and lower margins. This shear zone, like most observed in Hole BA4A, appears to have developed in a dike. **F.** Magmatic impregnation breccia displaying a leucocratic "matrix" with flow-like structures, which may have been some form of melt, and "clasts" of peridotite host rock.

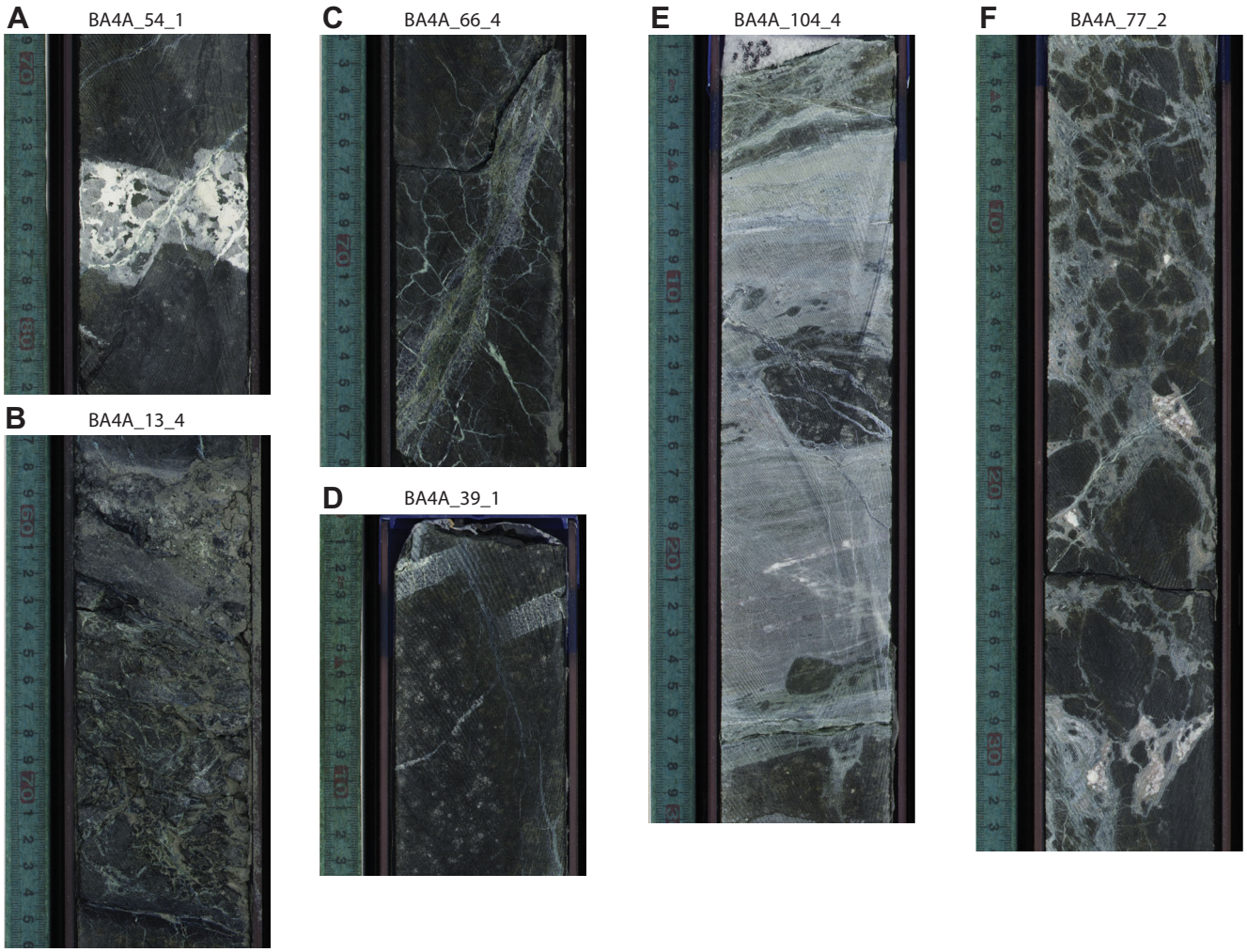

Figure F43. Cataclastic vein, Hole BA4A. **A, B.** Vein is located in the yellow box at 79–82 cm, near the bottom of the section. Note how the vein offsets the various dikes across faults with ~5 cm offsets. **C.** Full thin section. The cataclasite can be recognized as a dark pseudotachylite-resembling vein from the central lower part to the upper right corner. **D.** Photomicrograph in RL of area in red rectangle in (C) emphasizing the distribution of highly reflective minerals, mainly magnetite. A major fraction of these are <10 µm and many are submillimeter in size. **E.** Fragmentation of a large magnetite grain in (D). **F.** Green rectangle in (C) (XPL).

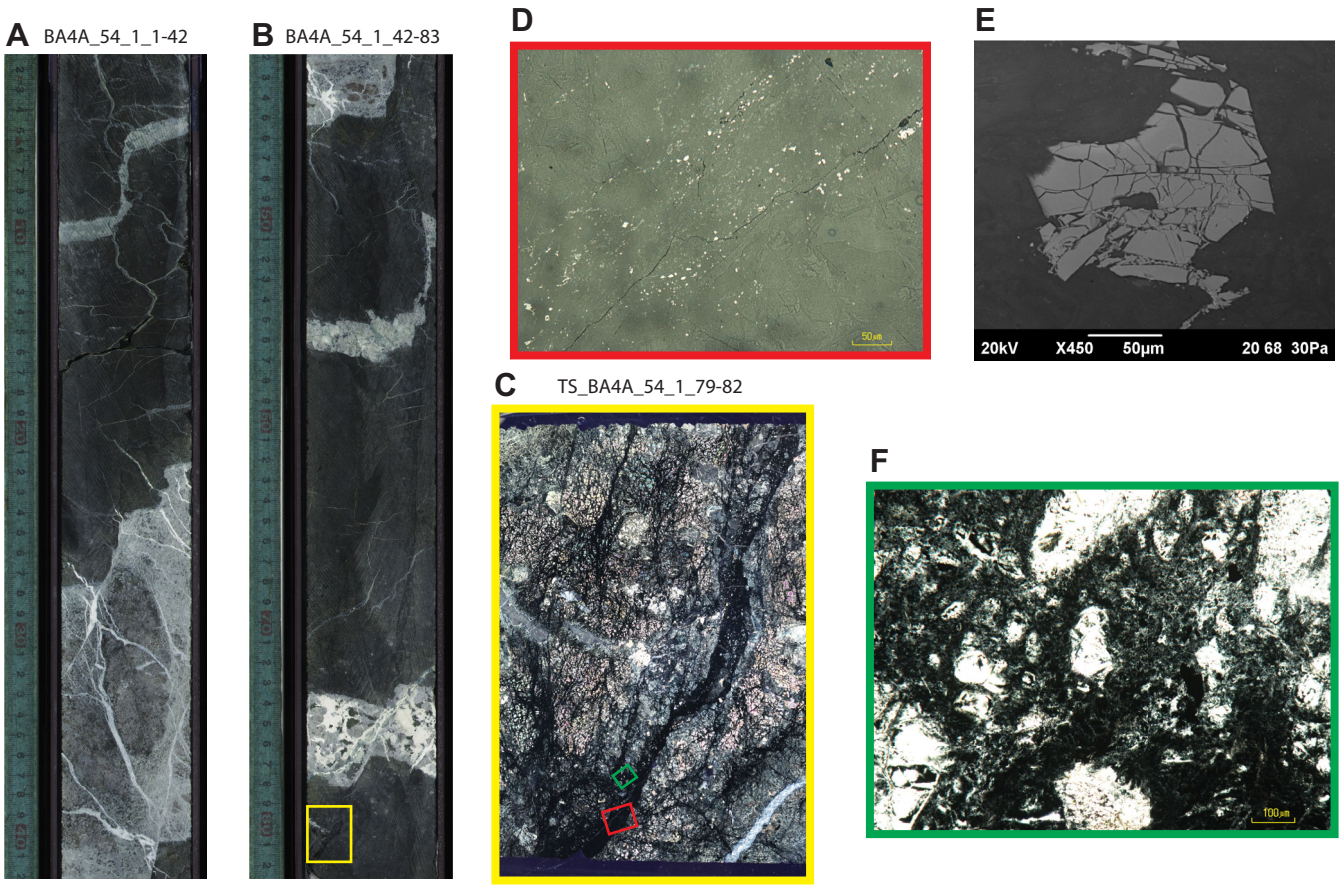

Figure F44. Dip angle vs. depth for each logged deformation feature, Hole BA4A. Features whose dip could not be accurately measured on the core are not included in this plot.

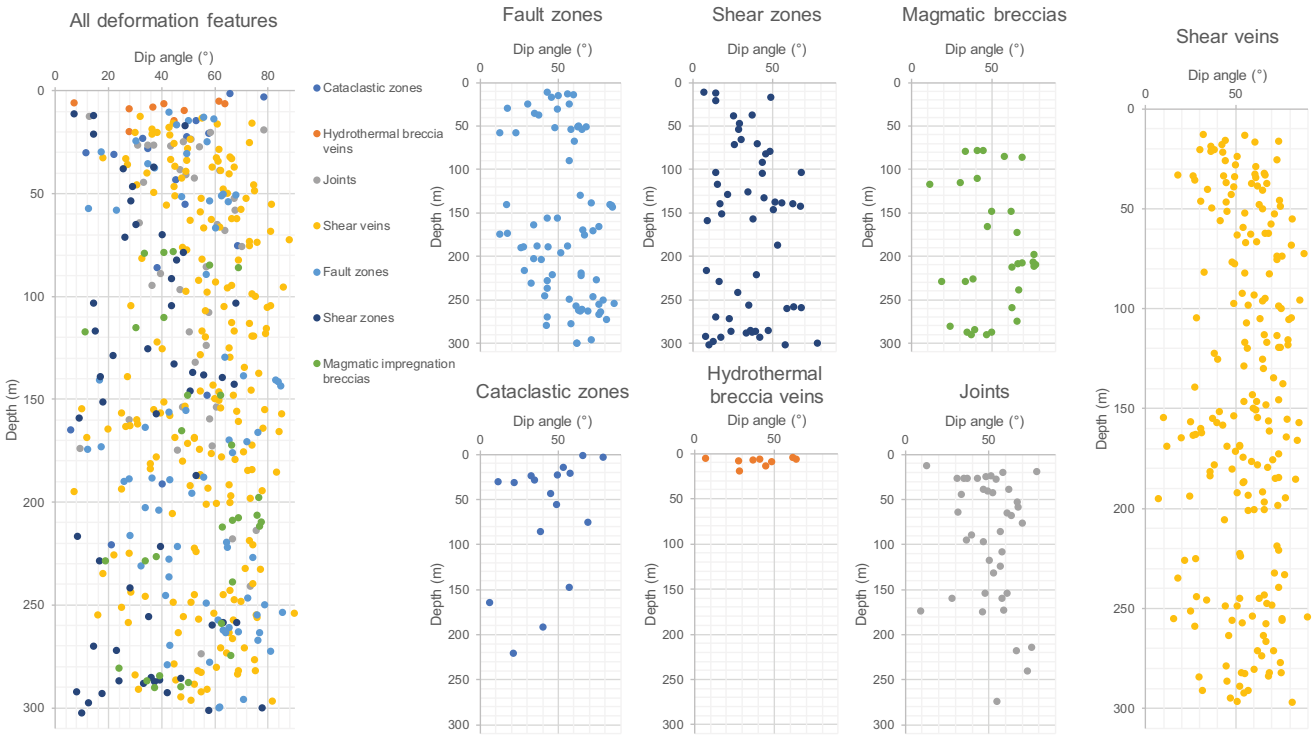

Figure F45. Dip angle of deformation structures, Hole BA4A. Fault zones, shear veins, and joints are typically steeply dipping, whereas shear zones generally have shallower dip angles. The magmatic impregnation breccias have a wide range of dip angles; these measurements usually represent somewhat unclear alignments of "clasts." Rose diagrams were calculated using Stereonet 9.5 (Cardozo and Allmendinger, 2013) with a binning angle of 10°.

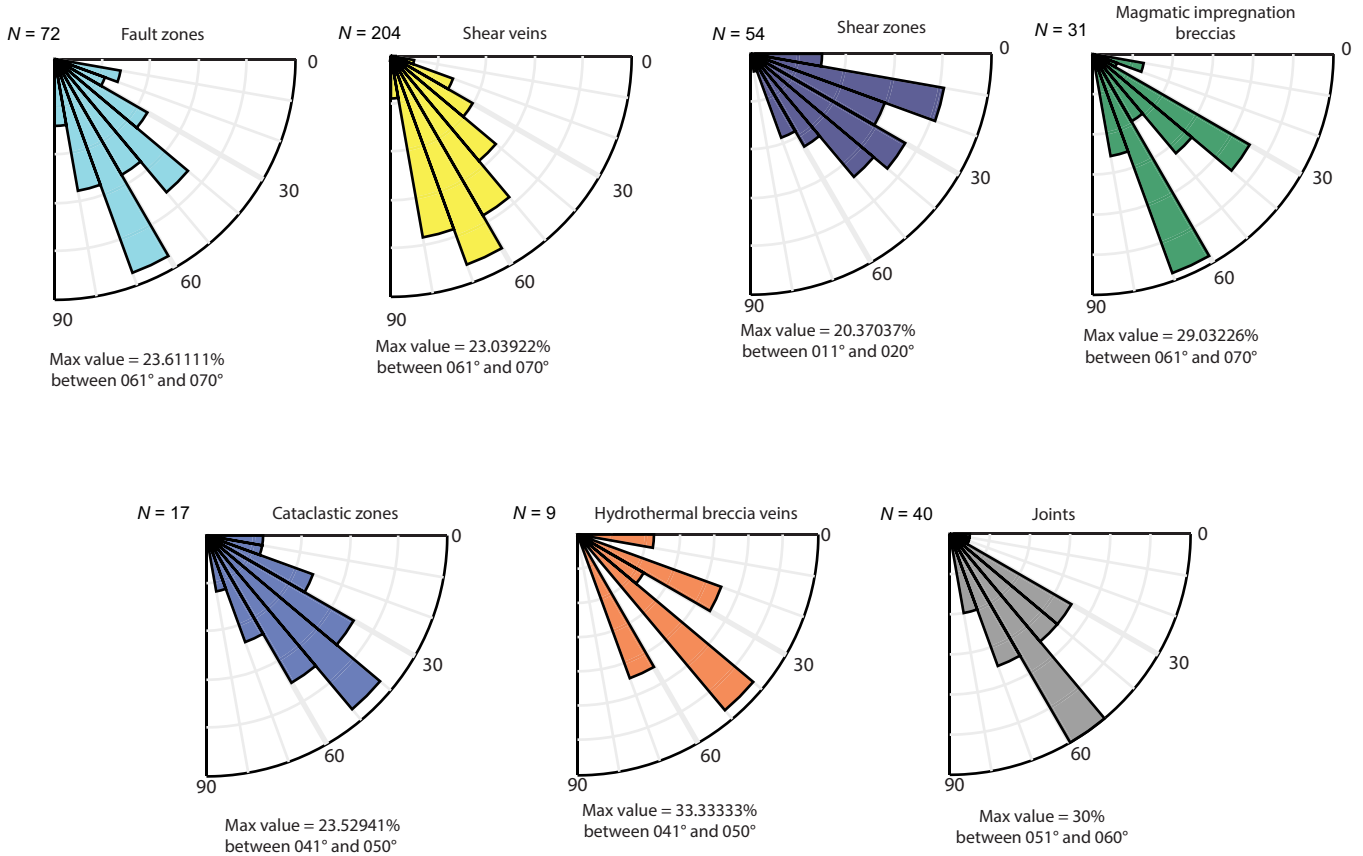

Figure F46. A. Dip angle of features that display an offset sorted into apparent normal or reverse shear sense based on that offset, Hole BA4A. Large offsets could not be captured in the core, so this data set is biased toward features with smaller, observable displacement. The shear sense given is that which was apparent when viewing the feature on the cut surface of the core. **B.** Lineation plunge. Only a few measured plunges are >50°, and these almost all occur between ~150 and 200 m. **C.** Plunge angle vs. dip angle of the plane on which they were measured. Points along the diagonal line are dip-slip (plunge similar to dip), points along the *y*-axis are strike-slip (plunge << dip), and points in between are oblique-slip (plunge < dip). Points beyond the diagonal line are likely due to the wavy nature of some of the measured planes; however, these points can be assumed to relate to dip-slip features.

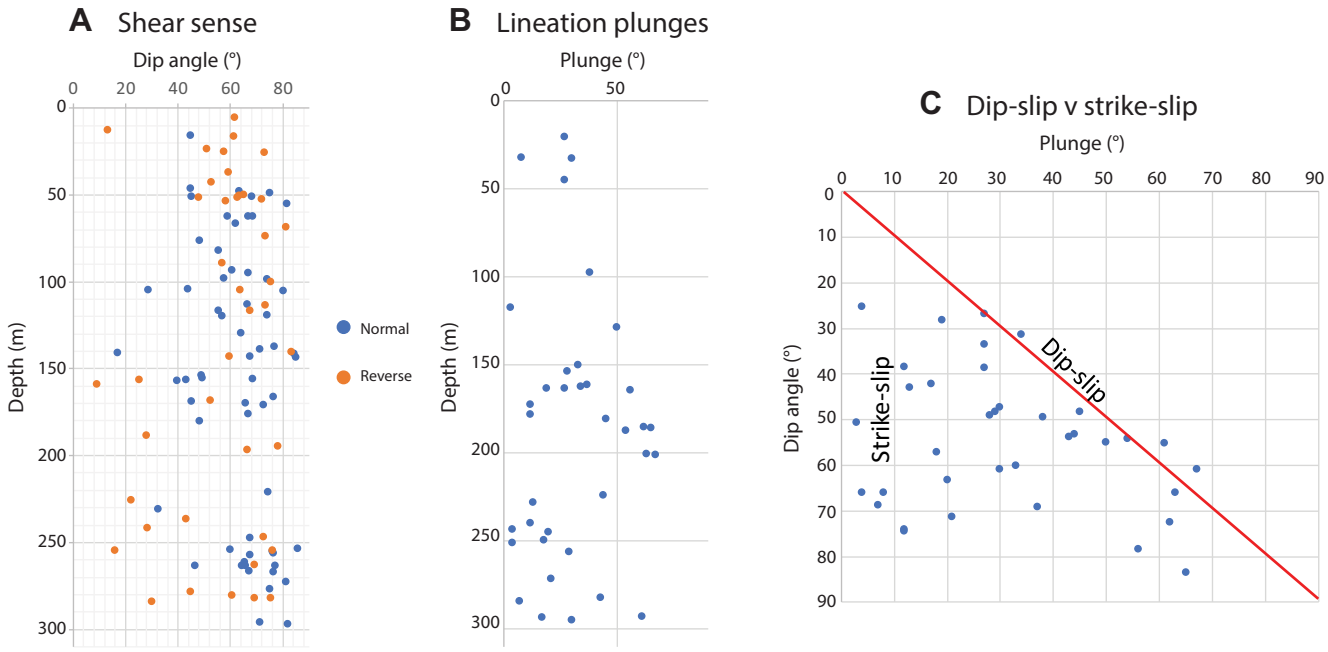

Figure F47. Variations of dip angles of the most abundant carbonate and serpentine vein types with depth superposed on dip angles of all serpentine veins (small light green data points) and overall rose diagrams of their dips weighted by vein density (using the vein density index as a preliminary weighting factor), Hole BA4A. Note that serpentine veins were only measured where clear orientations emerged from vein networks or the background mesh texture; therefore, their general frequency with depth is not representative for their true abundance. Rose diagrams are calculated using Stereonet 9.5 (Cardozo and Allmendinger, 2013) with a binning angle of 10°.

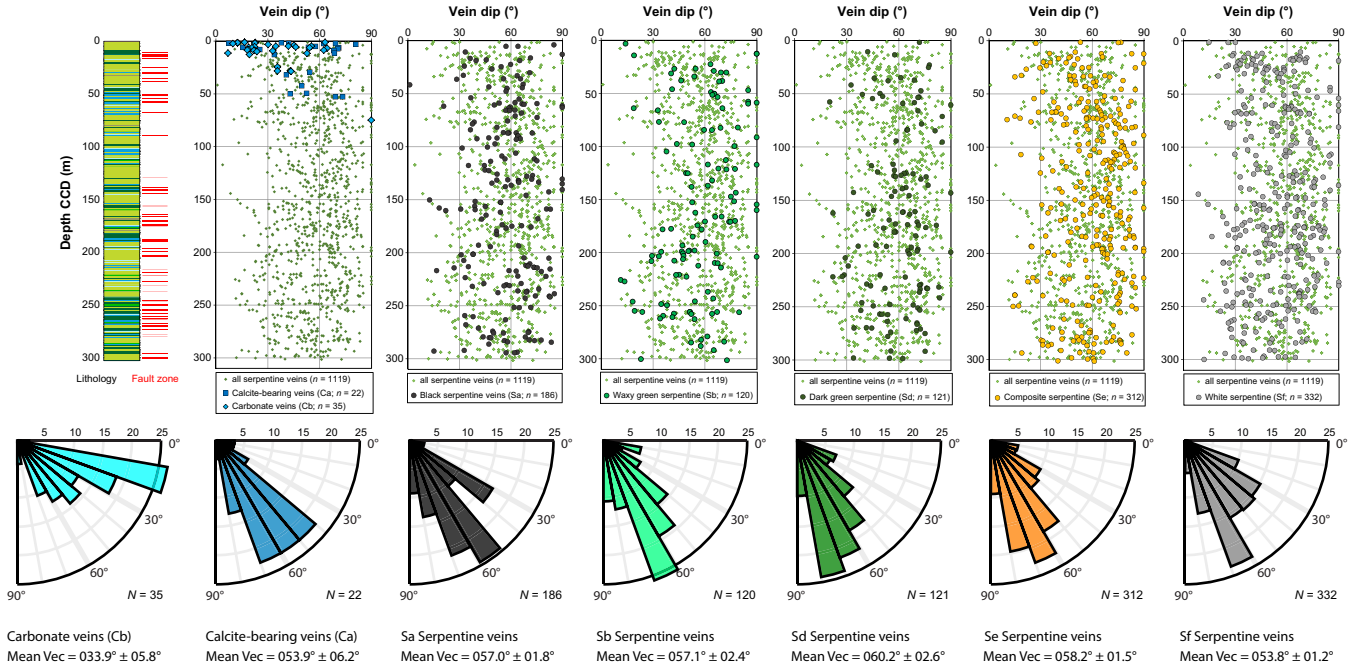

Figure F48. Downhole plots of LOI, Mg#, TiO_2, Ni, and Cr. Oman peridotite data from Godard et al. (2000), Hanghoj et al. (2010), Khedr et al. (2014), Lippard et al. (1986), Monnier et al. (2006), Rospabé et al. (2018), and Takazawa et al. (2003).

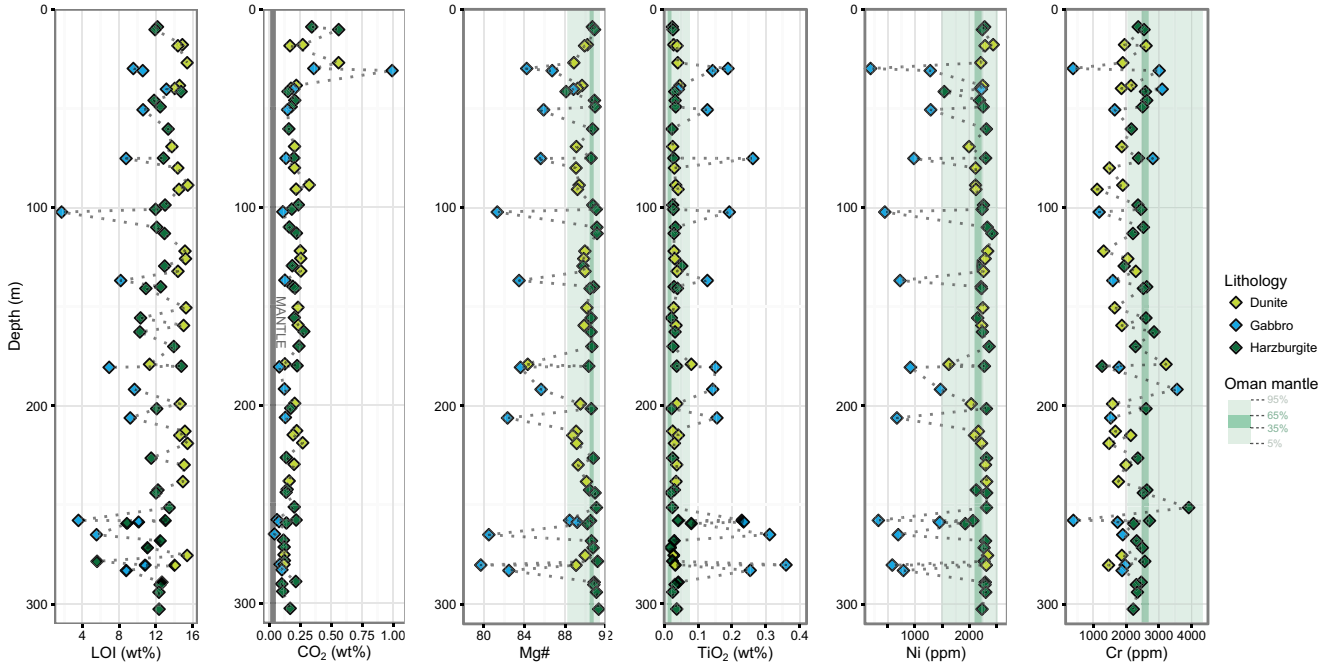

Figure F49. Volatile *X*-*Y* plots showing relationships between LOI, H_2O, and CO_2 and between total carbon (TC) and inorganic carbon (IC).

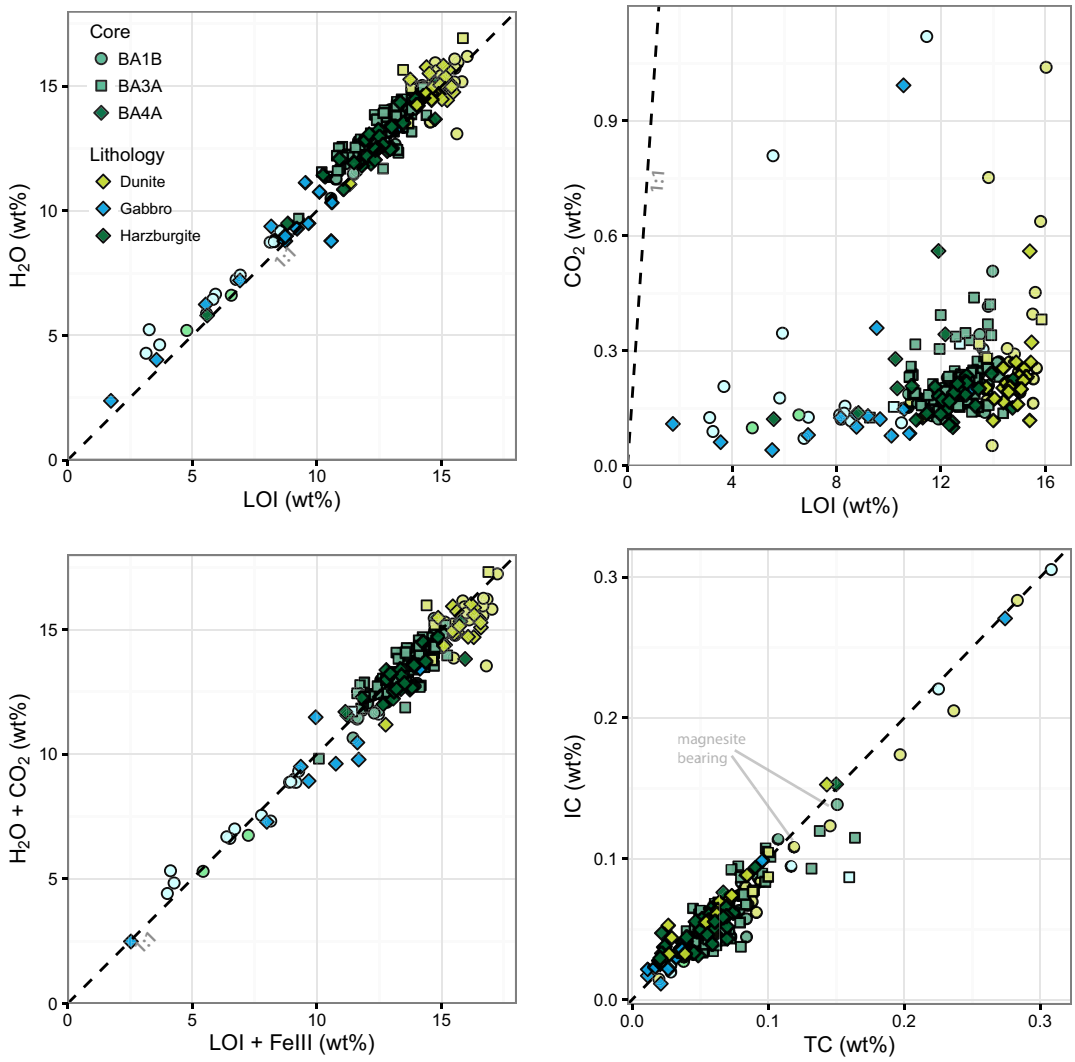

Figure F50. Peridotite differentiation diagrams showing MgO, SiO_2, CaO, Fe_2O_3, Cr, and TiO_2 against Al_2O_3. Oman peridotite data from Godard et al. (2000), Hanghoj et al. (2010), Khedr et al. (2014), Lippard et al. (1986), Monnier et al. (2006), Rospabé et al. (2018), and Takazawa et al. (2003).

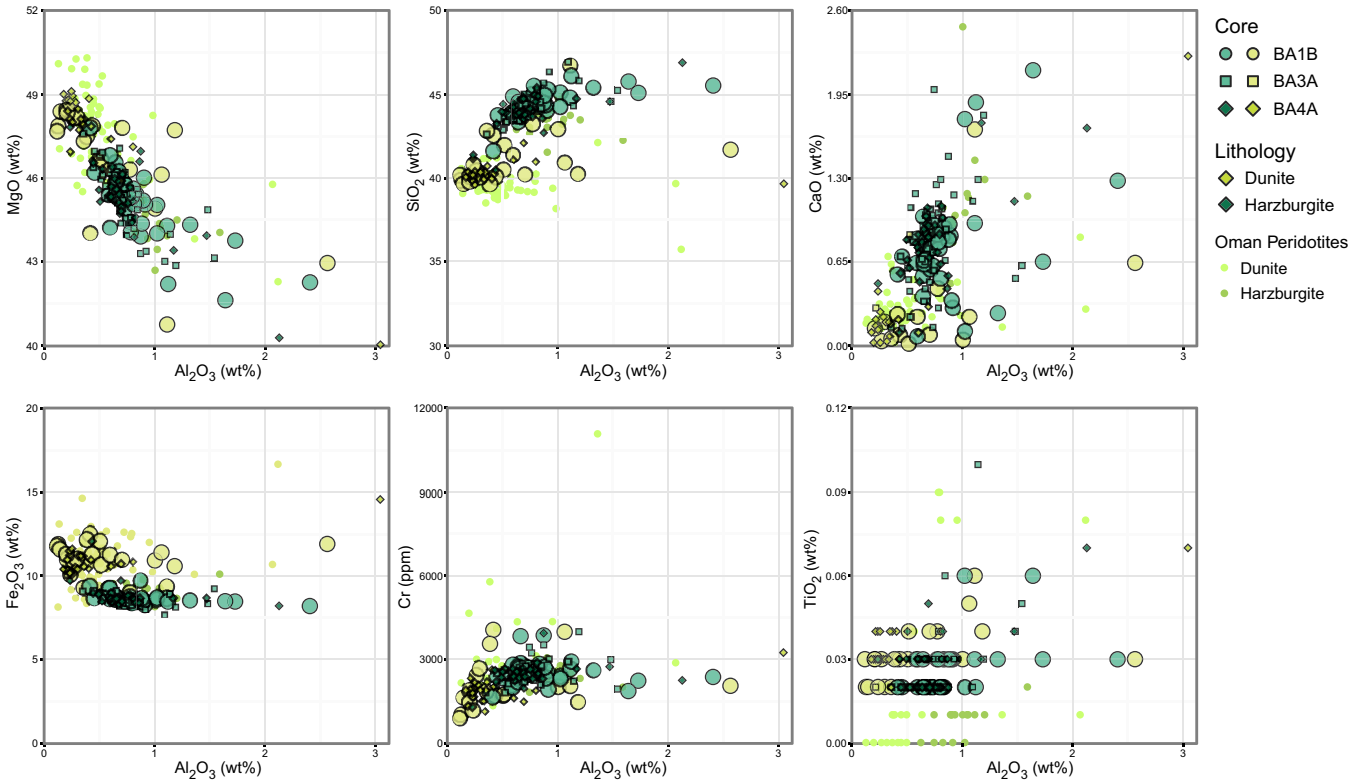

Figure F51. *X-Y* Plots of Mg# against Ni and Ca#. Oman peridotite data from Godard et al. (2000), Hanghoj et al. (2010), Khedr et al. (2014), Lippard et al. (1986), Monnier et al. (2006), Rospabé et al. (2018), and Takazawa et al. (2003).

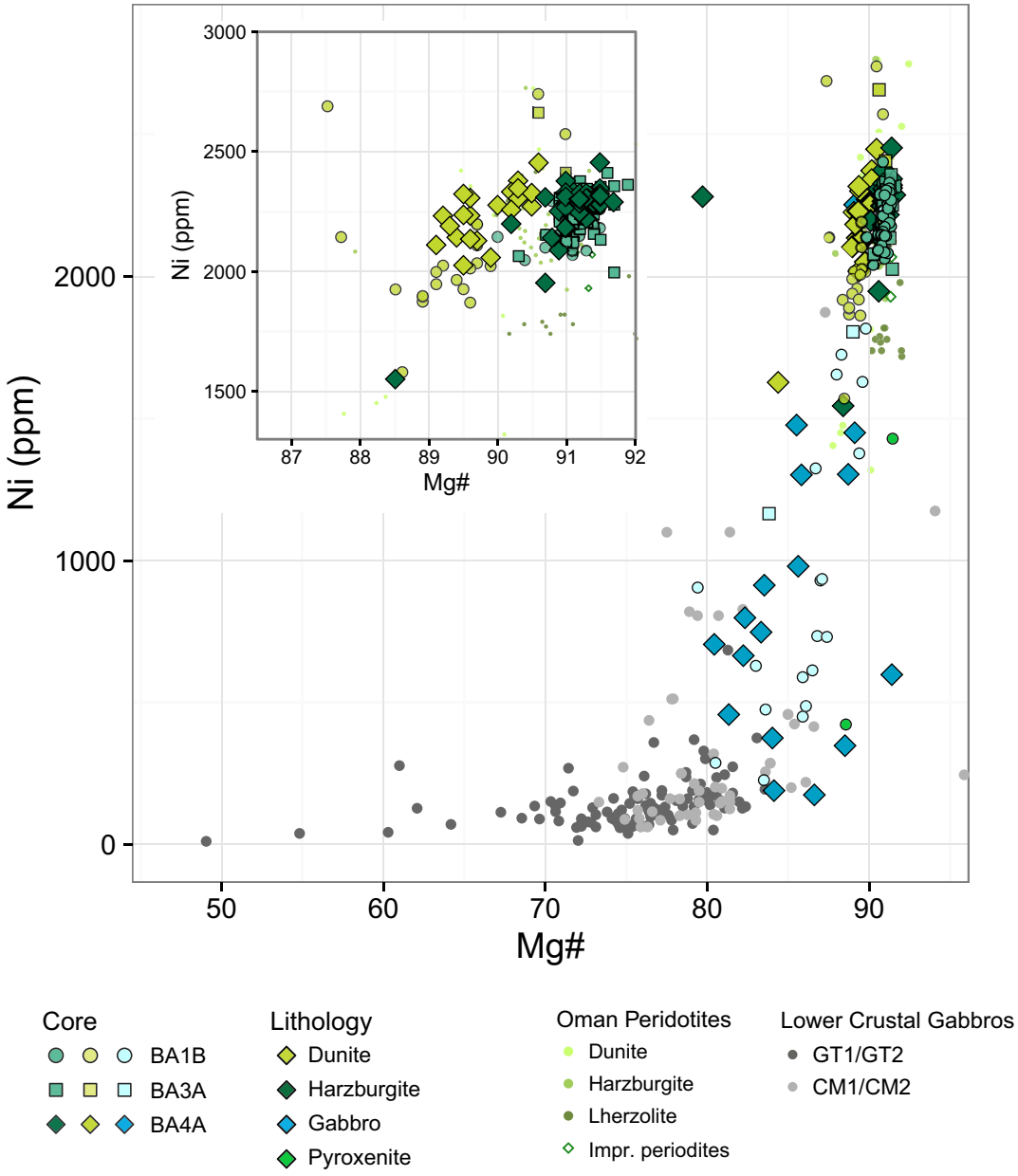

Figure F52. Magmatic differentiation diagram (Harker plots) showing Al_2O_3, MgO, Fe_2O_3, CaO, and TiO_2 against SiO_2. Lower crustal gabbro data are from Oman Drilling Project Holes GT1, GT2, CM1, and CM2. Oman peridotite data from Godard et al. (2000), Hanghoj et al. (2010), Khedr et al. (2014), Lippard et al. (1986), Monnier et al. (2006), Rospabé et al. (2018), and Takazawa et al. (2003).

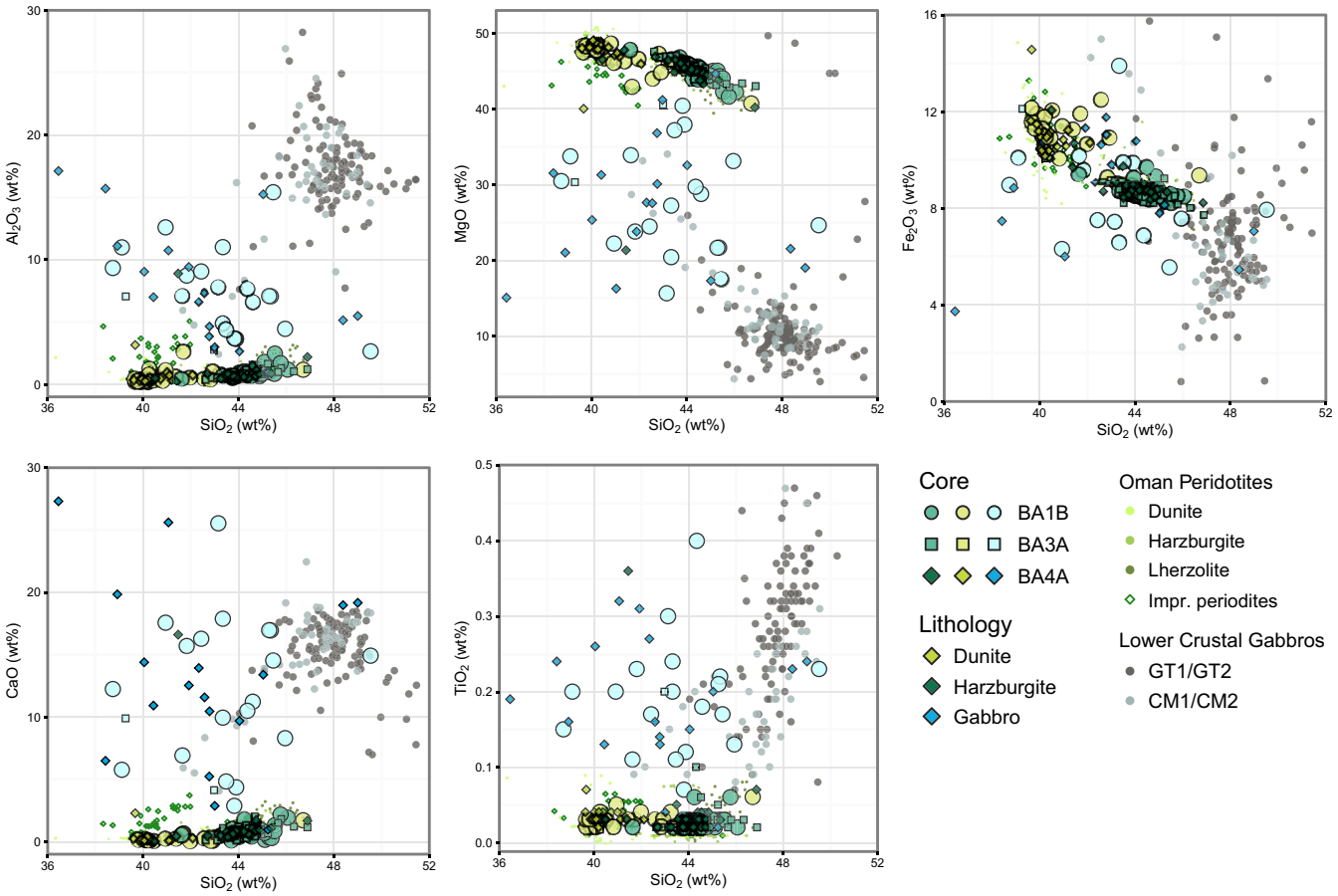

Figure F53. *X-Y* Plot of MgO against FeO (total). Oman peridotite data from Godard et al. (2000), Hanghoj et al. (2010), Khedr et al. (2014), Lippard et al. (1986), Monnier et al. (2006), Rospabé et al. (2018), and Takazawa et al. (2003).

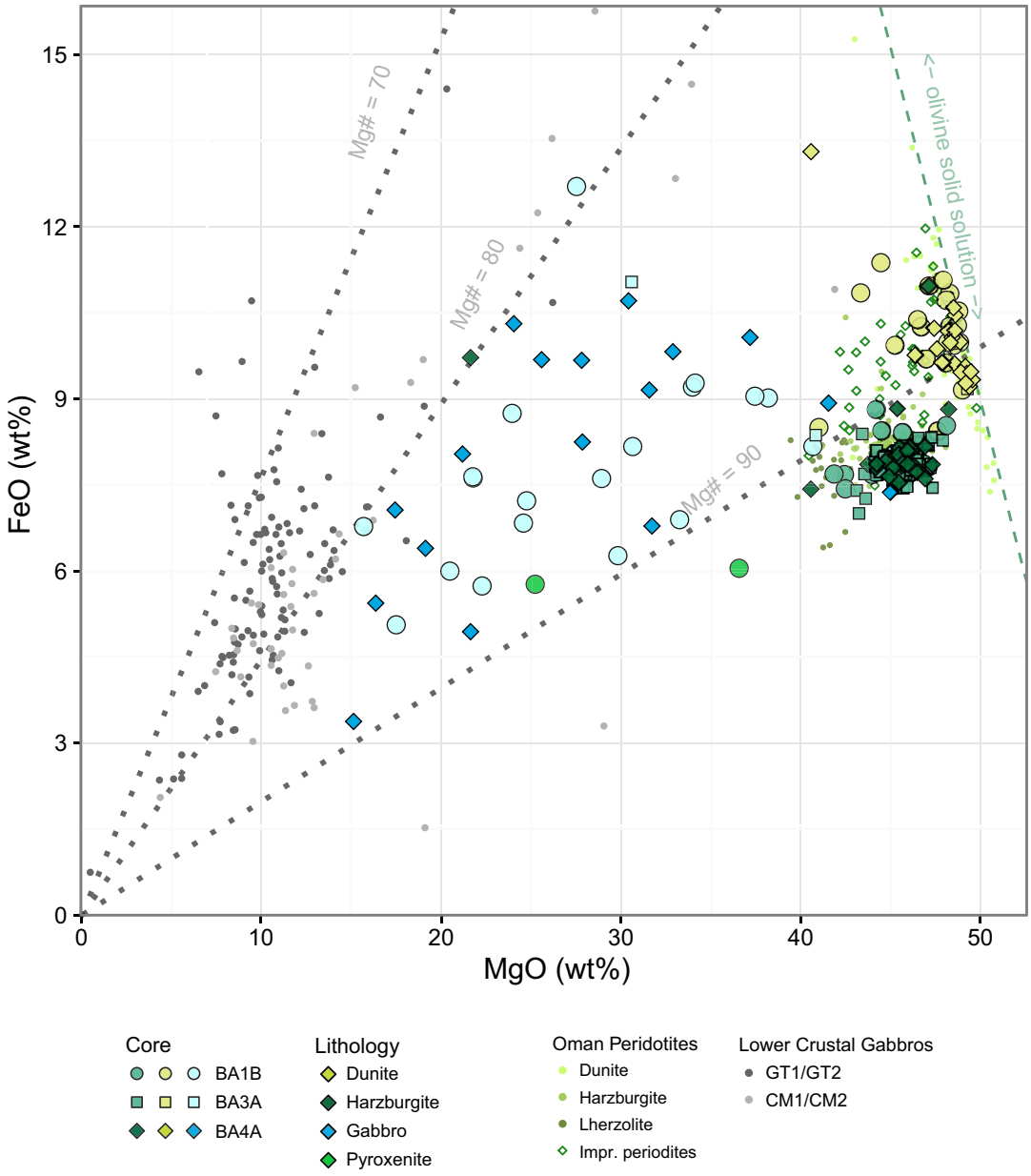

Figure F54. Ni and TiO_2 vs. Mg#. Oman peridotite data from Godard et al. (2000), Hanghoj et al. (2010), Khedr et al. (2014), Lippard et al. (1986), Monnier et al. (2006), Rospabé et al. (2018), and Takazawa et al. (2003).

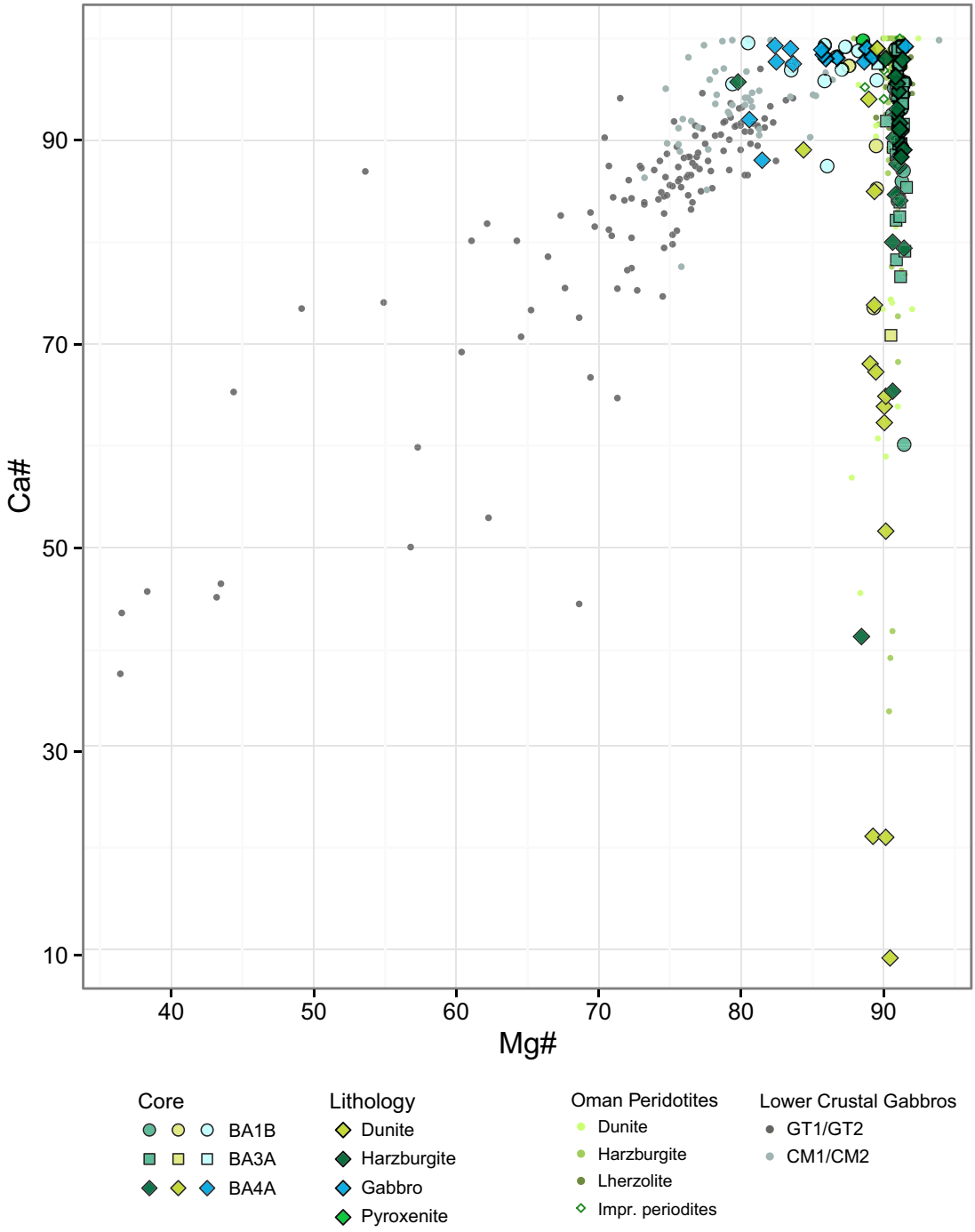

Figure F55. CI chondrite-normalized REE plot and Primitive Mantle (PM)-normalized trace element plot for selected harzburgites and gabbros analyzed by laser ablation–inductively coupled plasma–mass spectrometry (LA-ICP-MS). CI Chondrite and PM values from Sun and McDonough (1989).

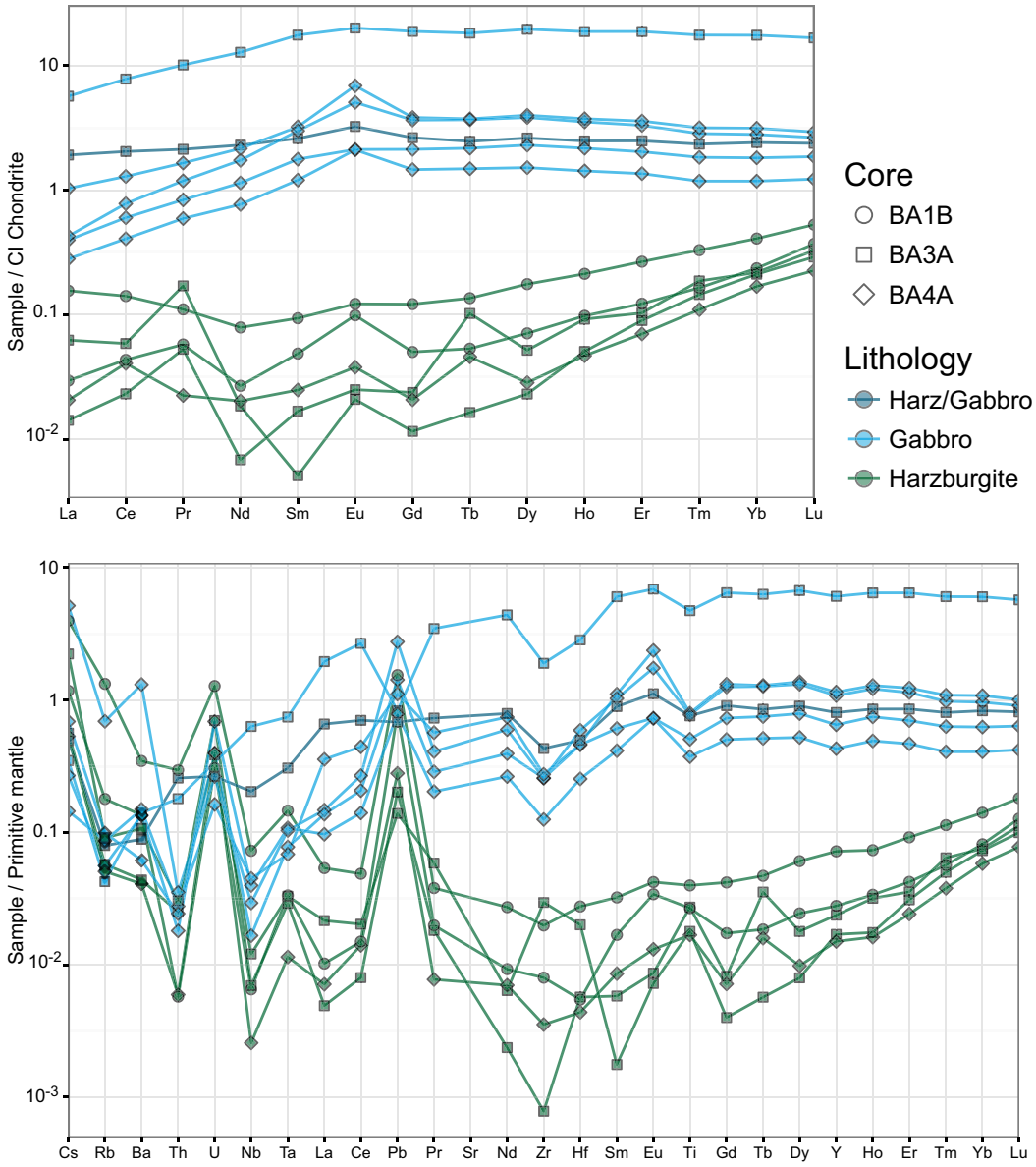

Figure F56. A: Downhole plots of NRM intensity, bulk (volume) magnetic susceptibility, and Koenigsberger ratios (*Q*), Hole BA4A.

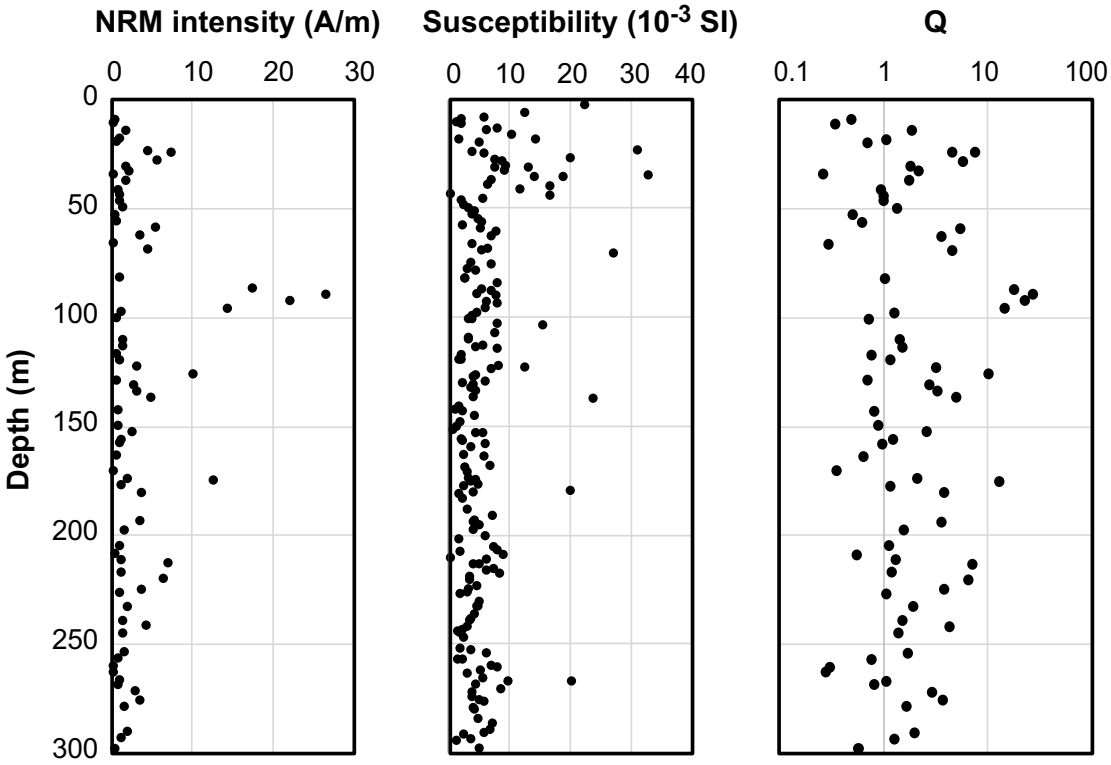

Figure F57. Downhole plots of NRM, ChRM, and soft component inclinations determined from principal component analysis, Hole BA4A.

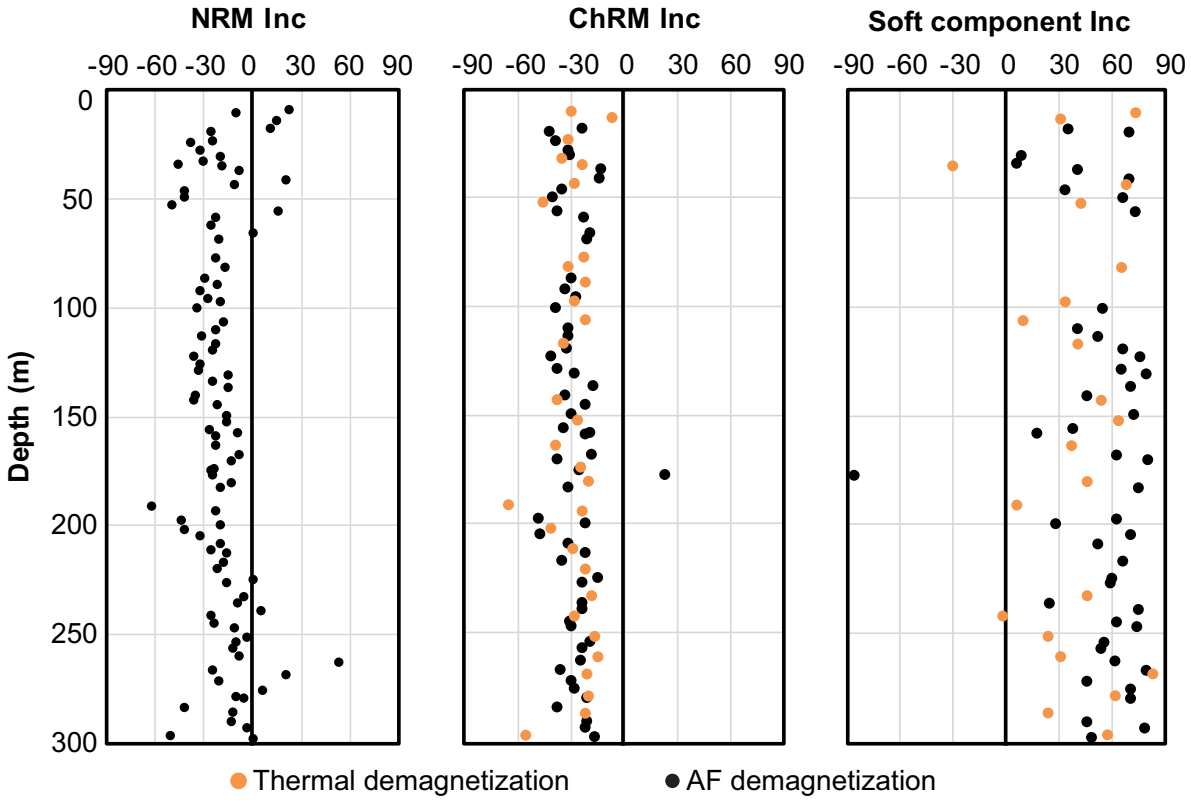

Figure F58. A. Representative orthogonal vector projections displaying behavior of magnetic remanence directions during progressive AF demagnetization of discrete samples. **B.** Changes in normalized remanence intensity as a function of field strength, Hole BA4A.

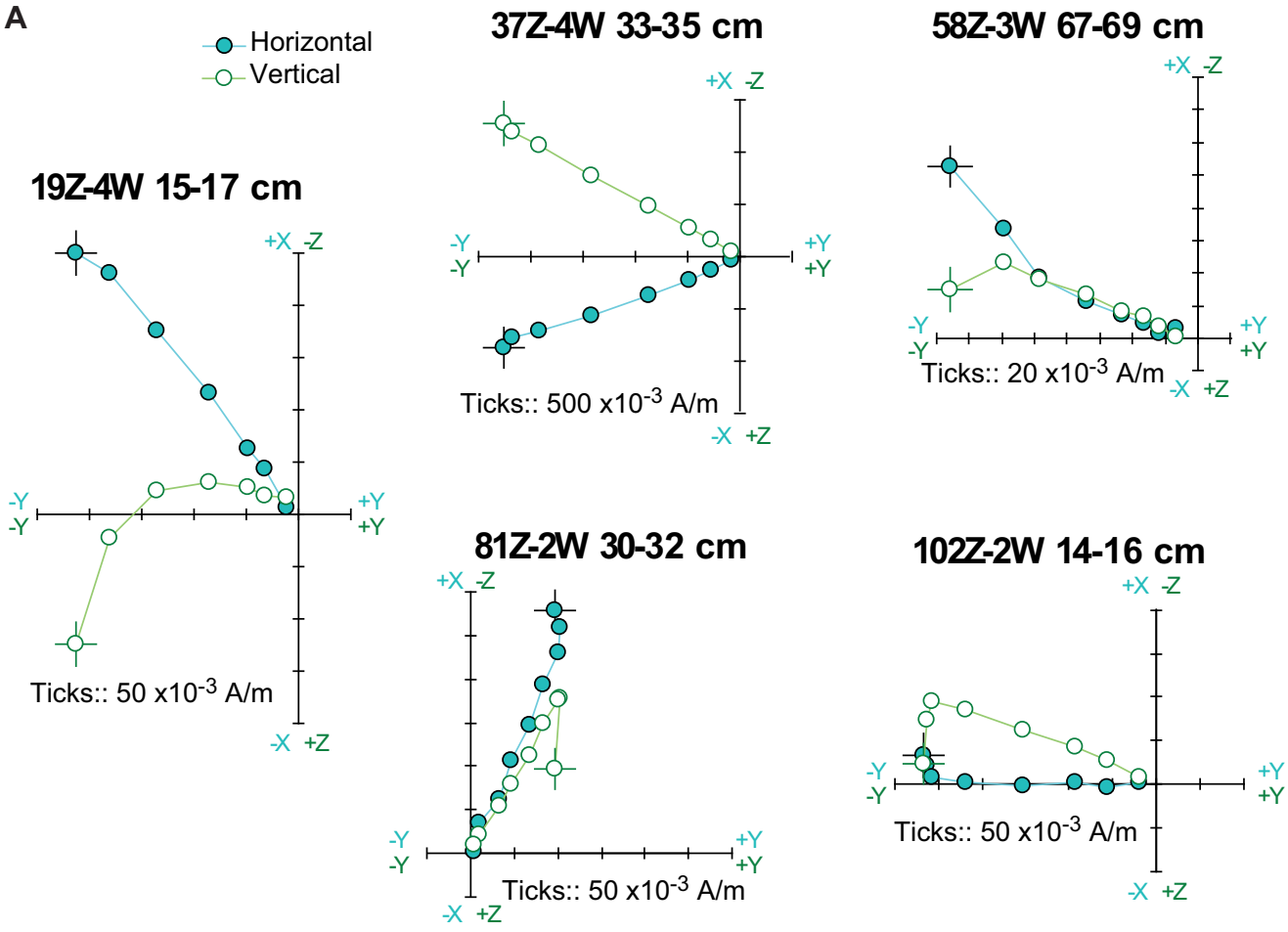

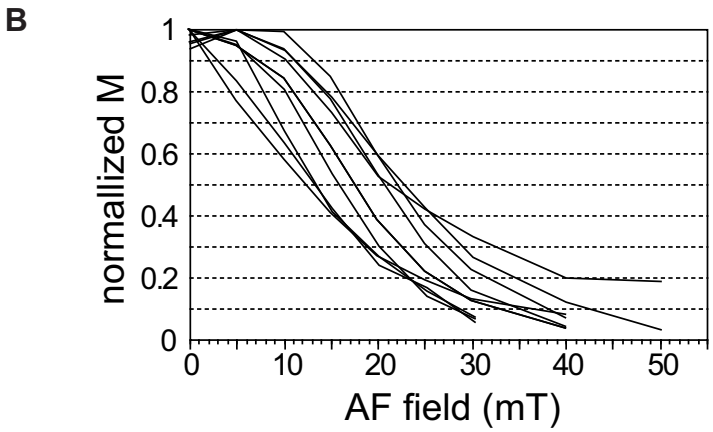

Figure F59. A. Representative orthogonal vector projections displaying behavior of magnetic remanence directions during progressive thermal demagnetization of discrete samples. **B.** Changes in normalized remanence intensity as a function of temperature, Hole BA4A.

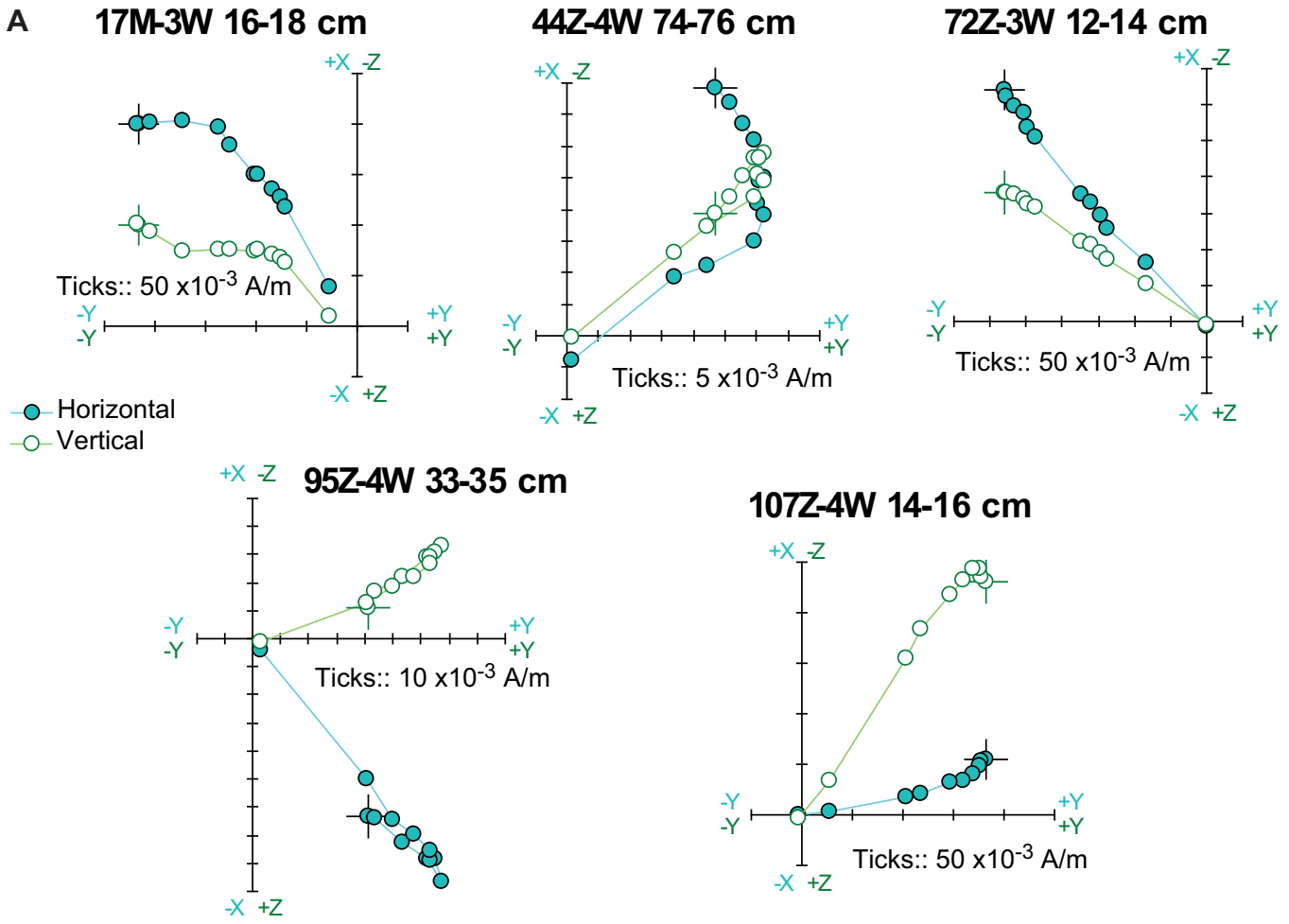

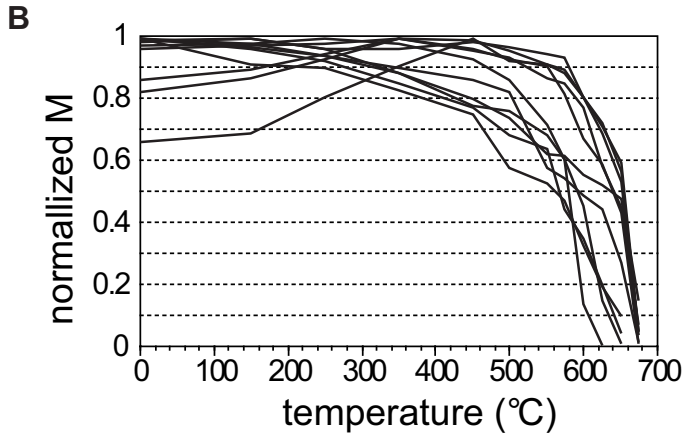

Figure F60. Downhole plots of median destructive field (MDF) and median destructive temperature (MDT) during demagnetization experiments, Hole BA4A.

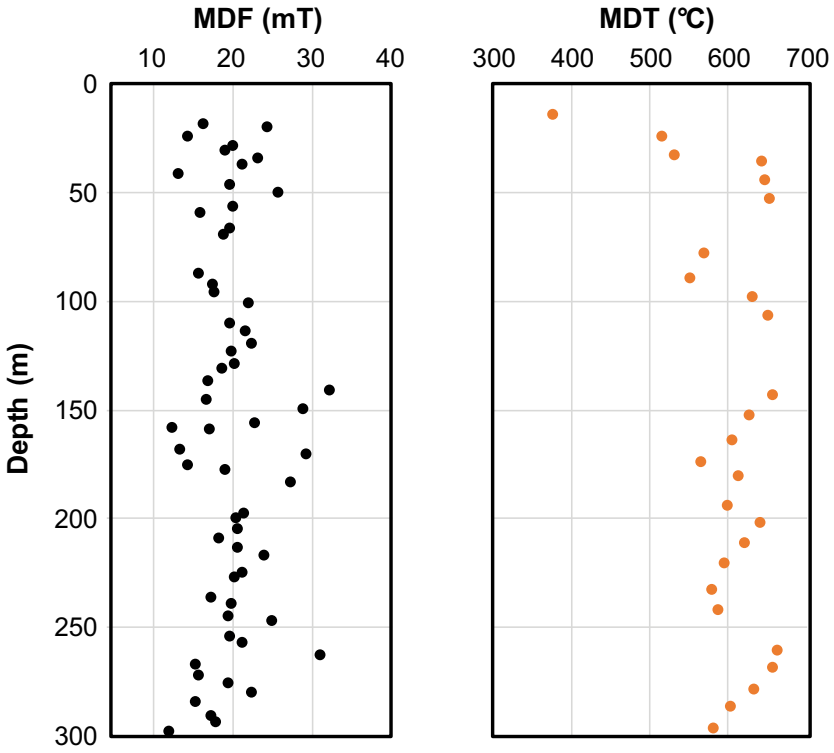

Figure F61. A. Downhole plots of magnetic anisotropy intensity (P'), shape parameter (T), and K_{max} and K_{min} inclinations. **B.** Degree of anisotropy as a function of bulk susceptibility. **C.** Shape parameter T vs. degree of anisotropy of magnetic susceptibility.

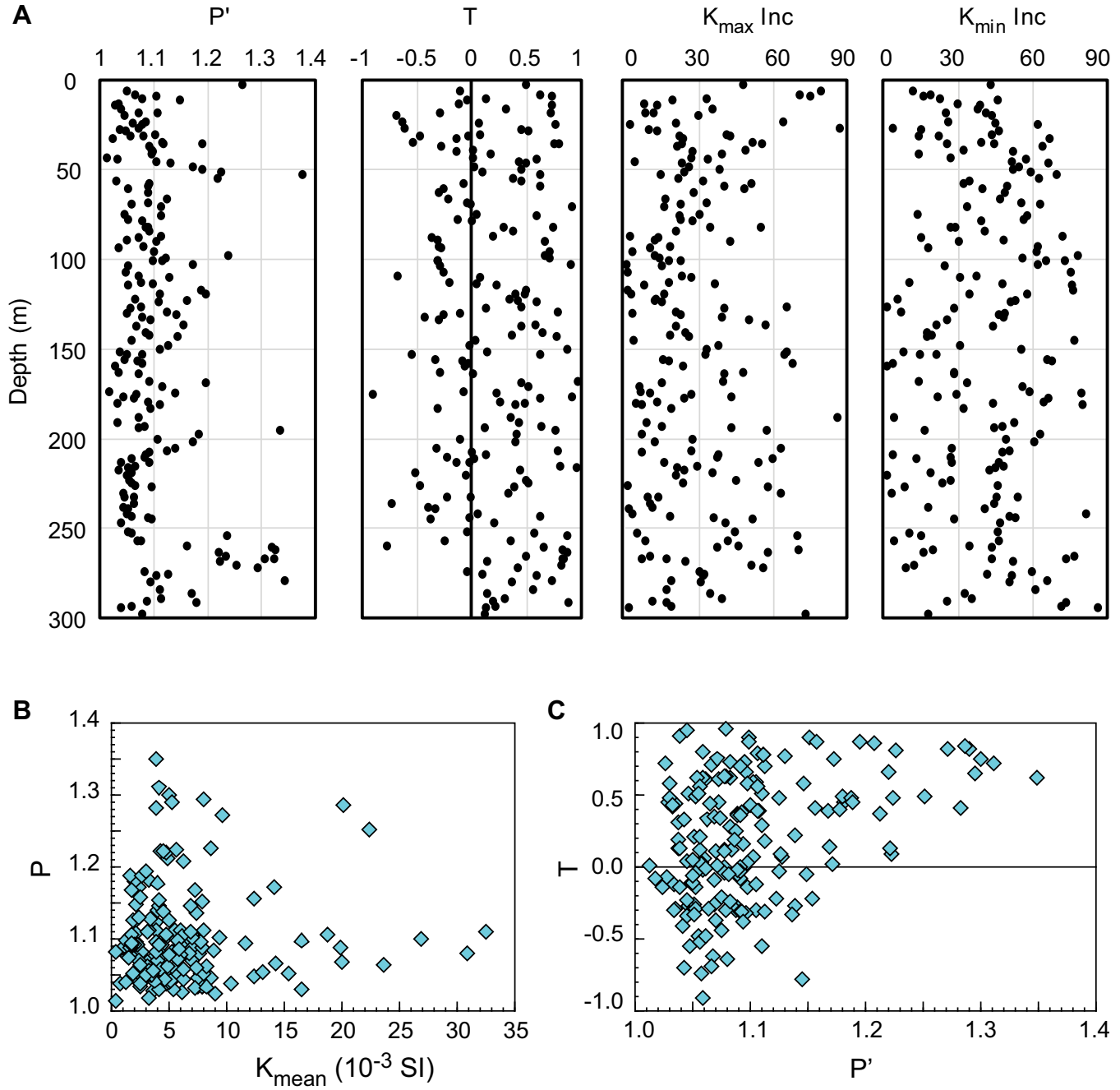

Figure F62. Contoured stereoplots of principal susceptibility axes from AMS analyses plotted on lower hemisphere equal-area projections in the core reference frame, Hole BA4A.

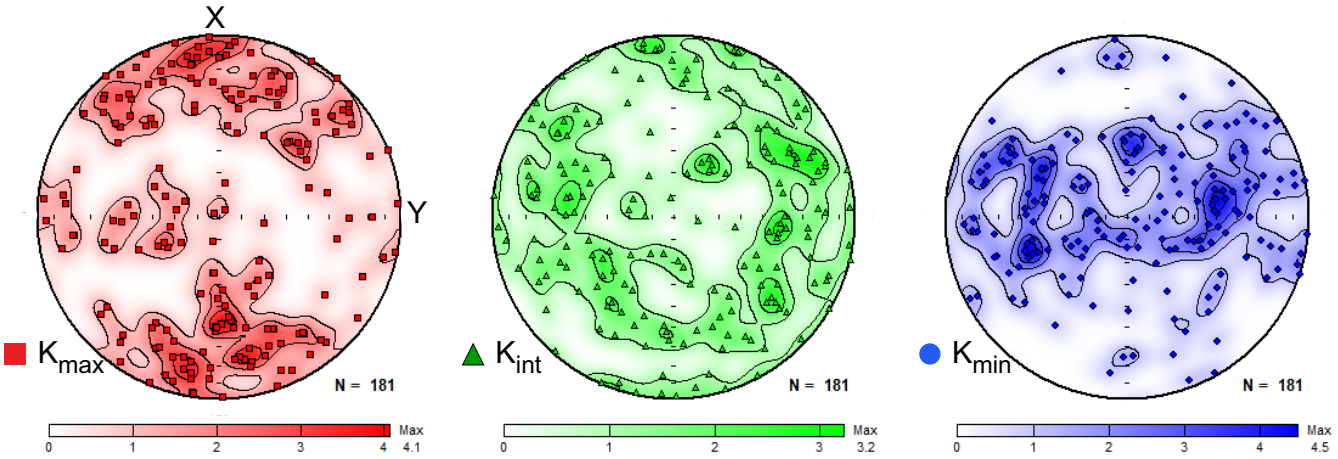

Figure F63. GRA density, MS, NCR, NGR, and average XCT values by lithology, Hole BA4A.

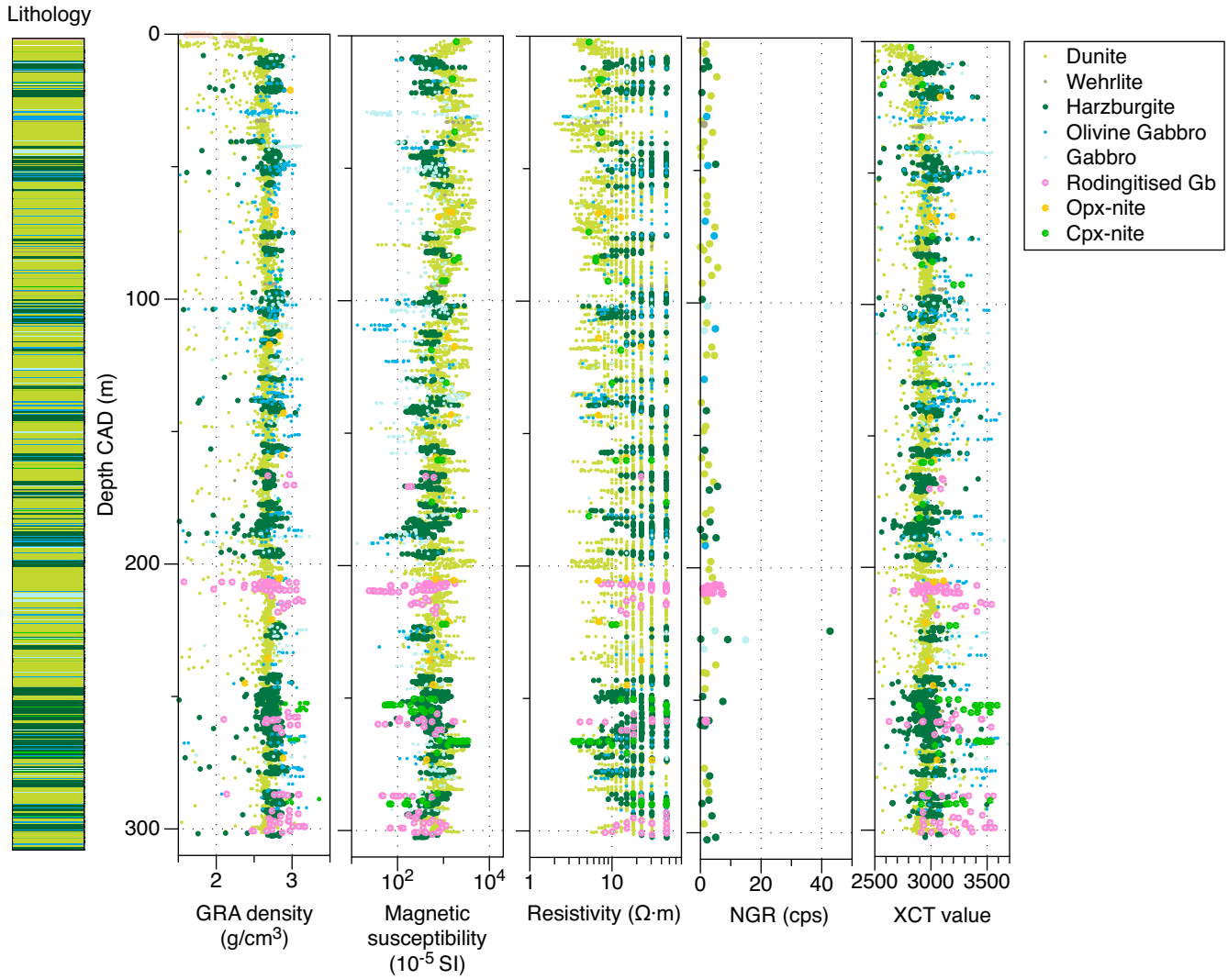

Figure F64. Examples of MSCL-I image, average and mode of CT values, and CT image. **A.** Dunite with gabbroic dikes (Section 49Z-4). **B.** Dunite with dikes and fractures (Section 92Z-1). The relatively high XCT number for Section 49Z-4 suggests less alteration.

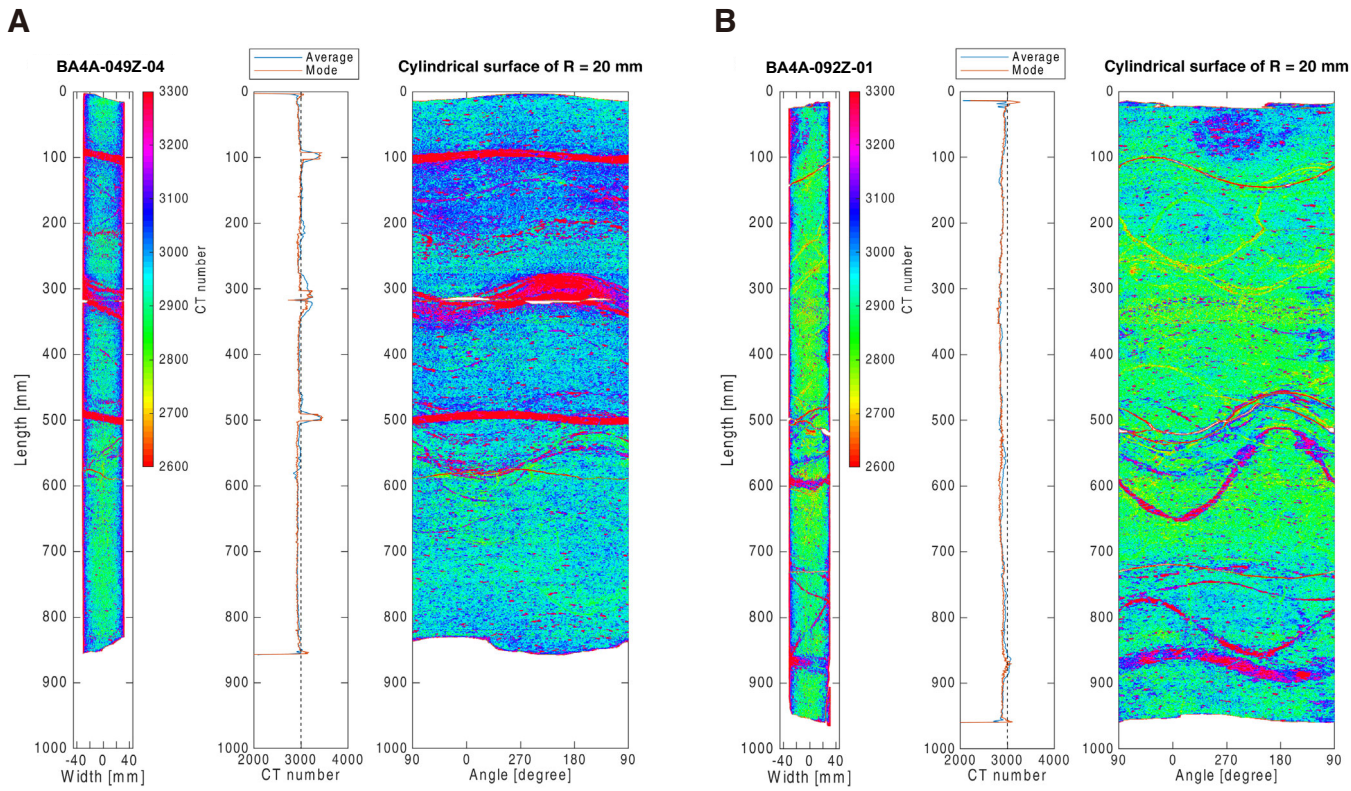

Figure F65. Correlation between GRA density and (**A**) XCT value and whole-round resistivity (i.e., electrical conductivity) and (**B**) magnetic susceptibility, Hole BA4A. Liner fitting lines are shown in each figure. Holes BA3A and CM2B data are plotted for comparison.

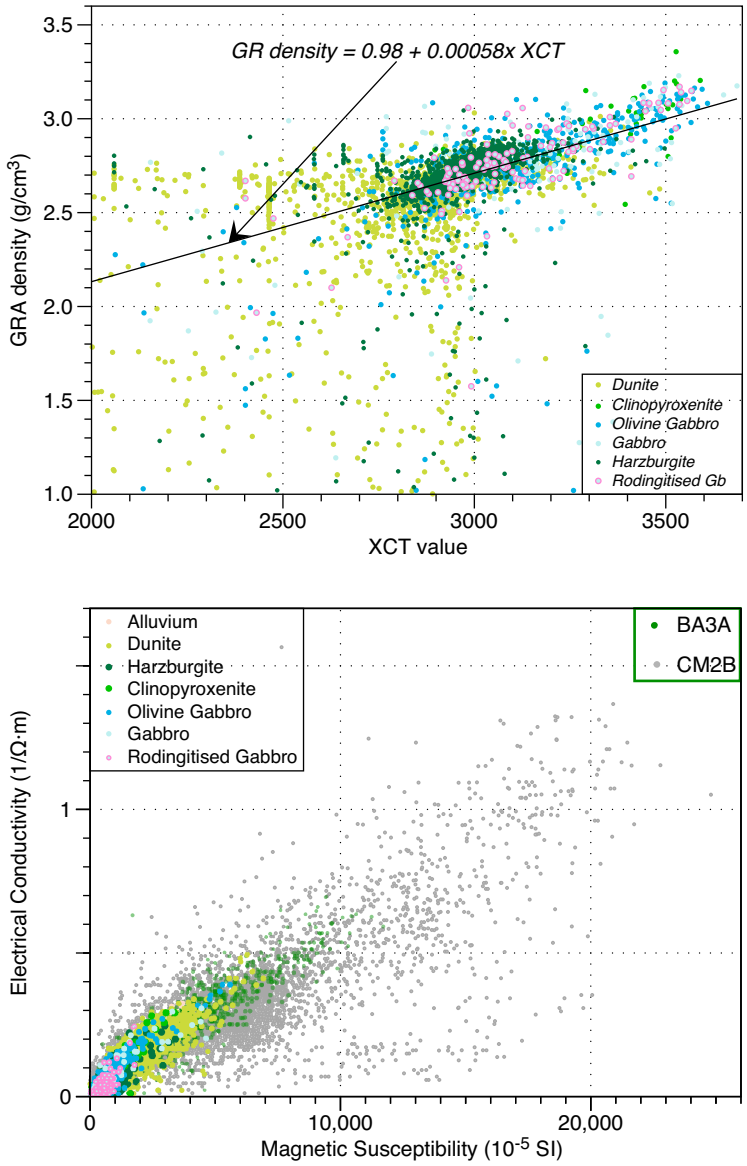

Figure F66. Downhole plots of discrete sample measurements of physical properties. (**A**) P-wave velocity, (**B**) bulk density, (**C**) grain density, (**D**, **E**) porosity on normal and log scales, (**F**) electrical resistivity under dry and wet conditions, (**G**) bulk magnetic susceptibility (AMS), and (**H**) thermal conductivity, Hole BA4A.

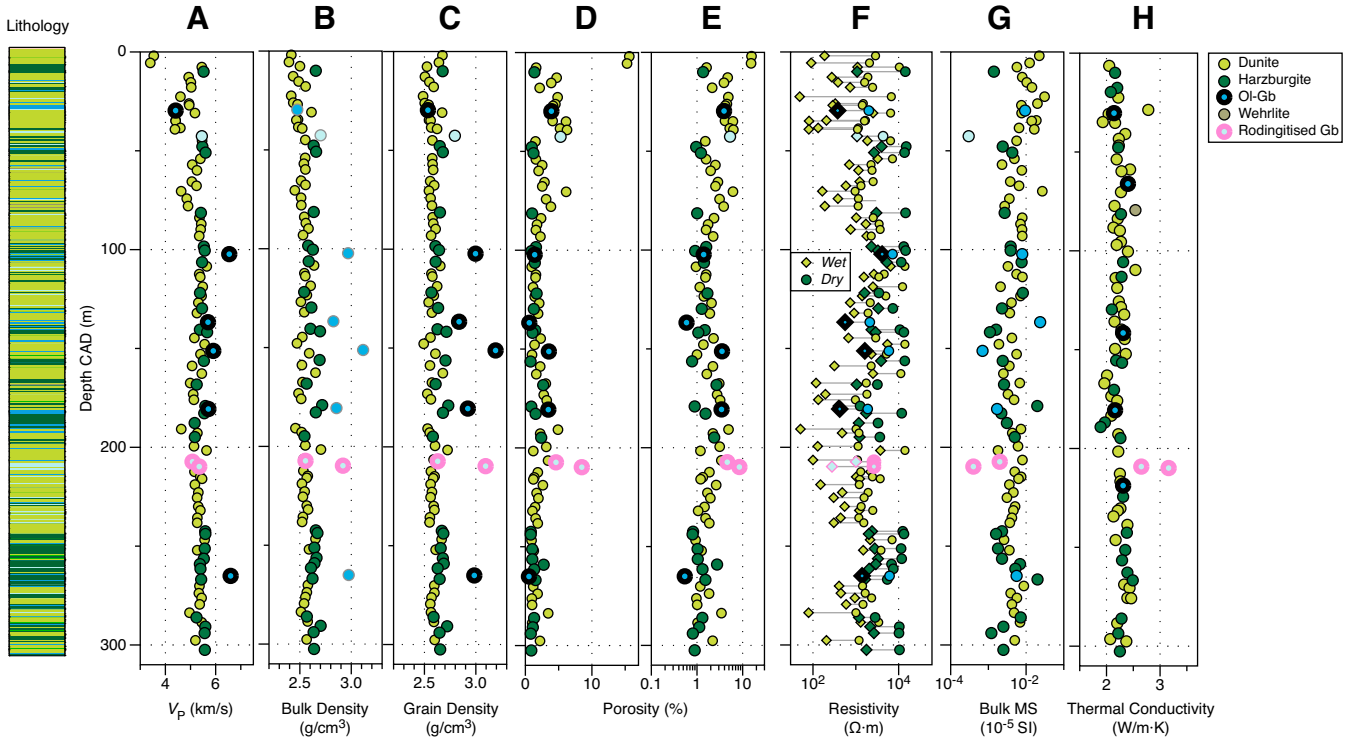

Figure F67. Downhole plot of averaged P-wave velocity, azimuthal anisotropy, and perturbation of velocity in each orientation from the average, Hole BA4A.

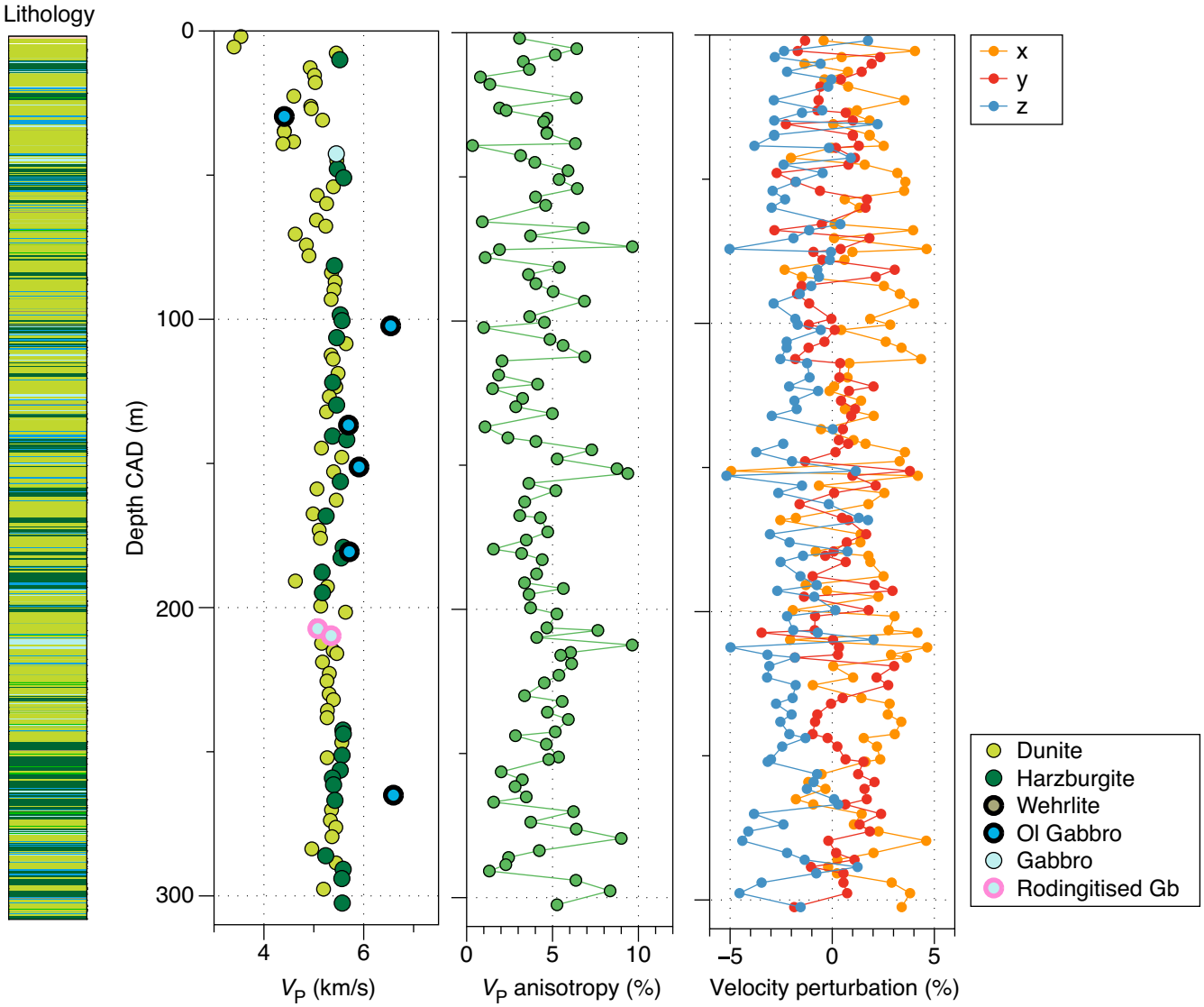

Figure F68. Relationships between P-wave velocity and (**A**) bulk density and (**B**) grain density of minicube samples. Hole BA3A data are plotted for comparison, Hole BA4A.

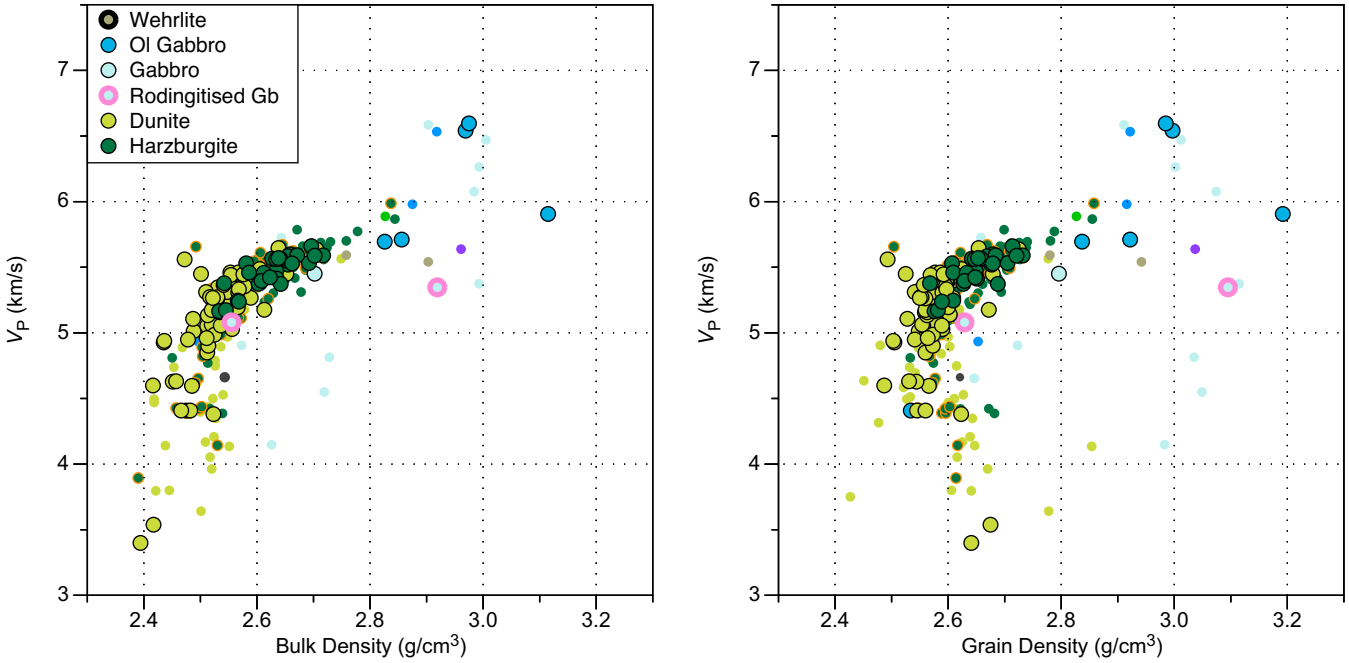

Figure F69. Relationships between P-wave velocity and porosity of minicube samples plotted with (**A**) linear scale and (**B**) logarithmic scale of the horizontal axis, Hole BA4A. Hole BA3A data are plotted for comparison.

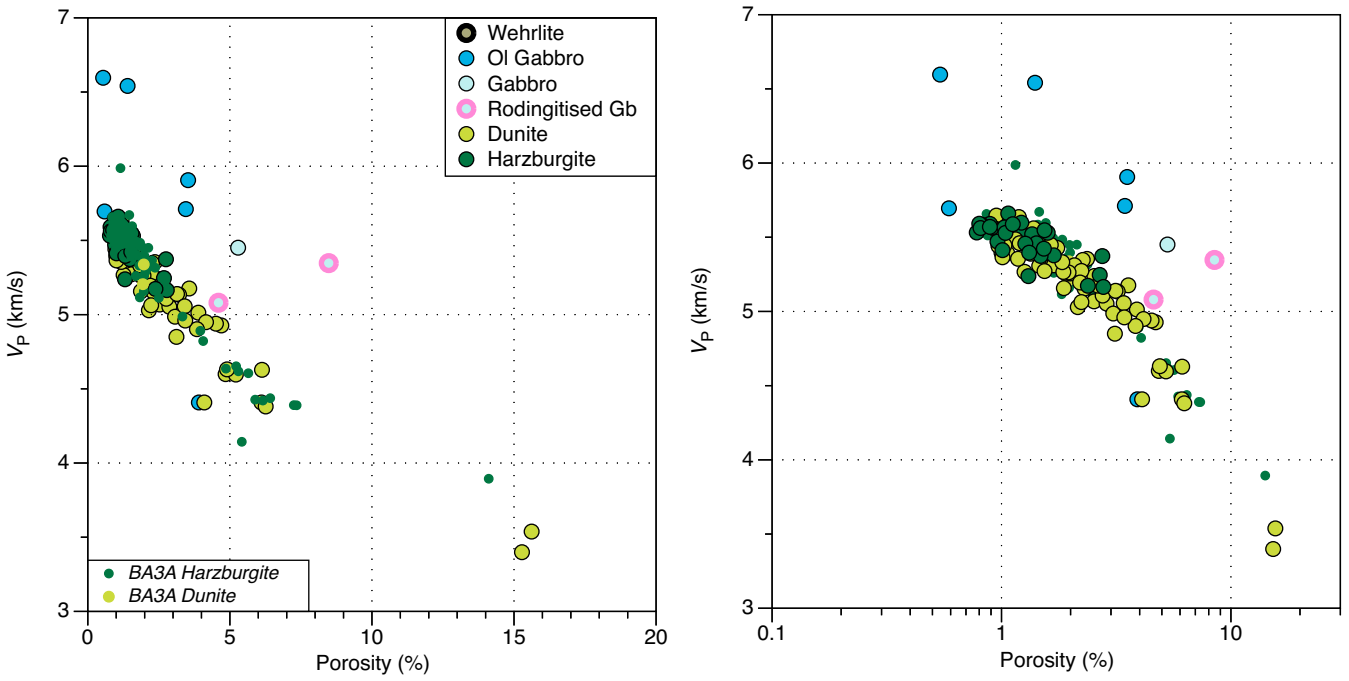

Figure F70. Relationships between porosity and average XCT value from Holes BA1B, BA3A, and BA4A. Black and gray lines are linear fitting lines for the dunites and harzburgites with XCT < 2980 and 3000, respectively.

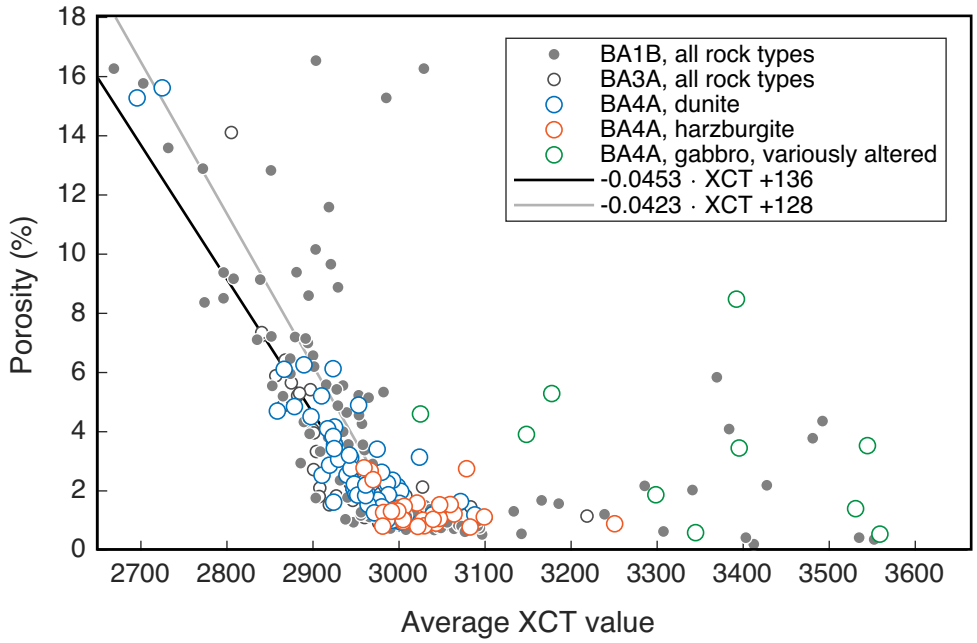

Figure F71. Relationships between grain density and standard deviation of XCT value in the cube samples from Hole BA4A. Gray line = linear fitting line for harzburgites.

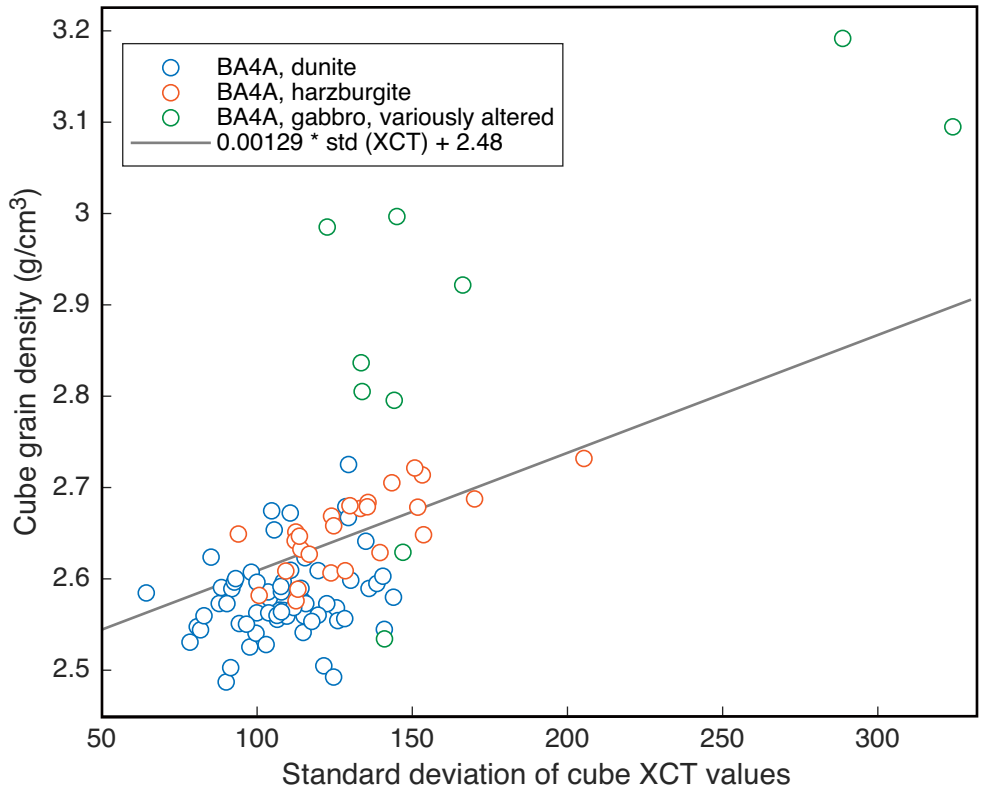

Figure F72. Downhole plot of porosity inferred from XCT data using the linear correlation, Hole BA4A.

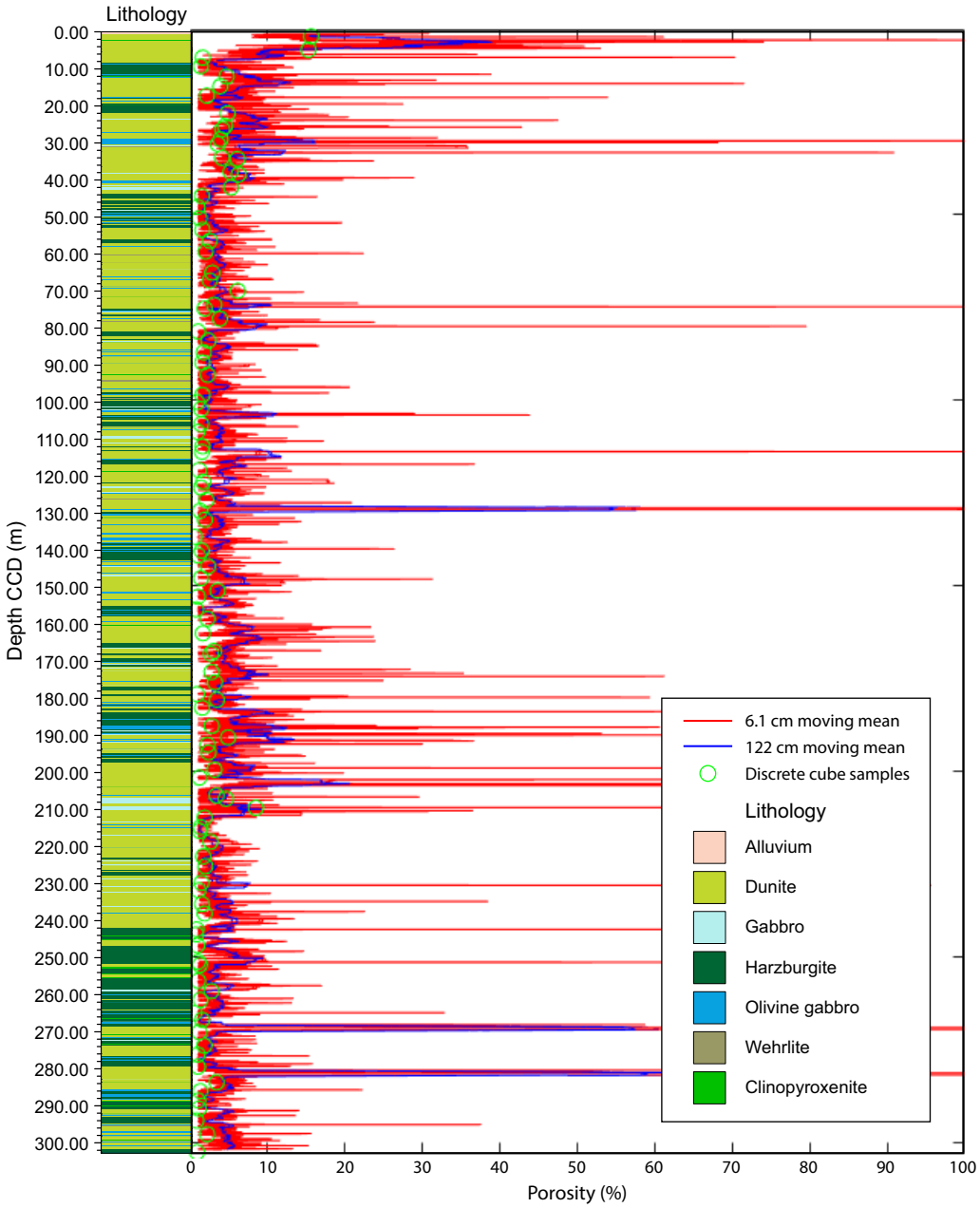

Figure F73. Correlation between bulk magnetic susceptibility and electrical resistivity of the minicube samples (dry and wet measurements), Hole BA4A. Hole BA1B and BA3A data are plotted for comparison.

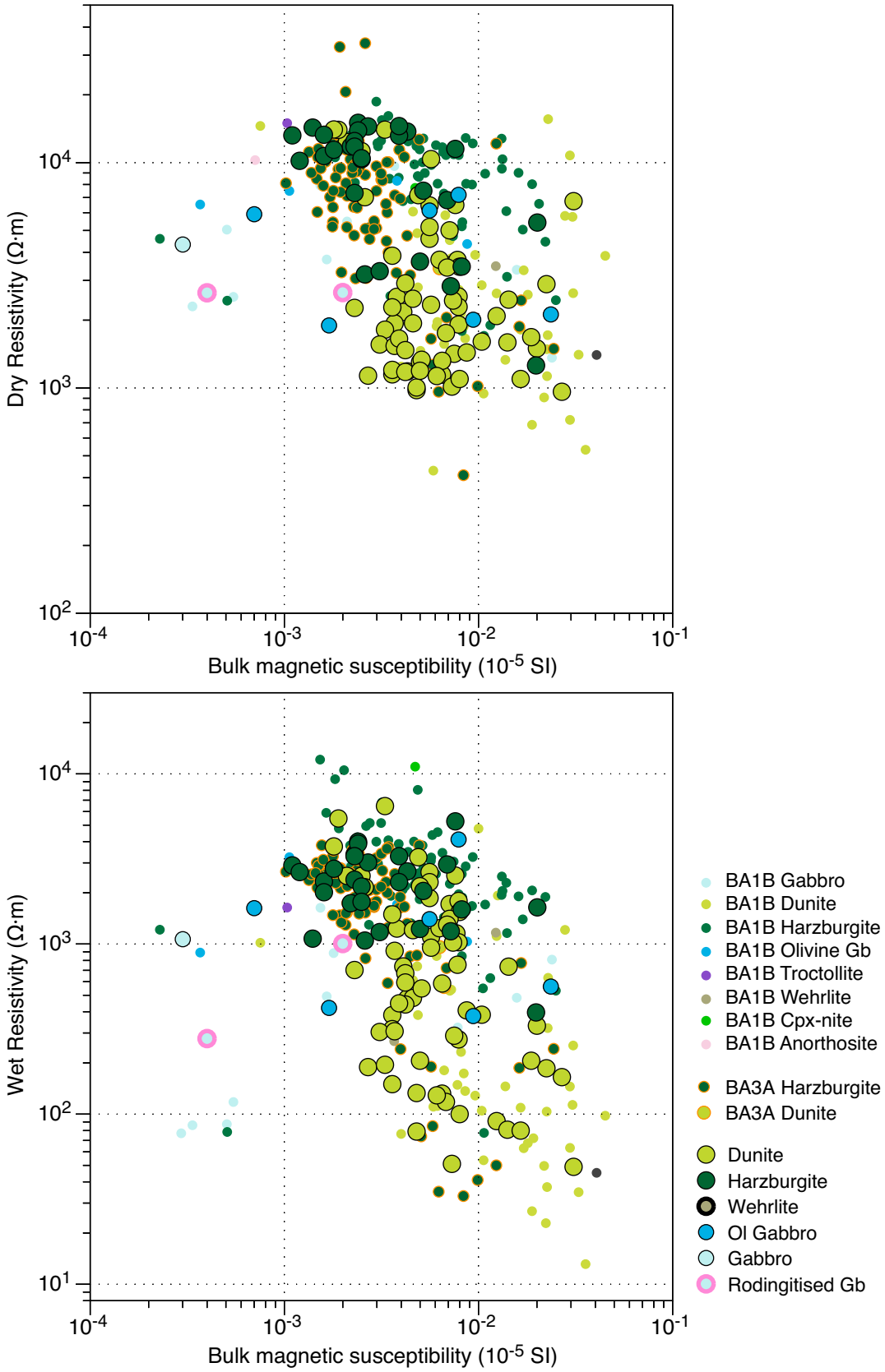

Figure F74. Thermal conductivity and P-wave velocity of the minicube samples plotted with XCT value, Hole BA4A. These physical properties are correlated to the XCT value, and fitting lines are shown in each figure. Hole BA1B and BA3A data are plotted for comparison.

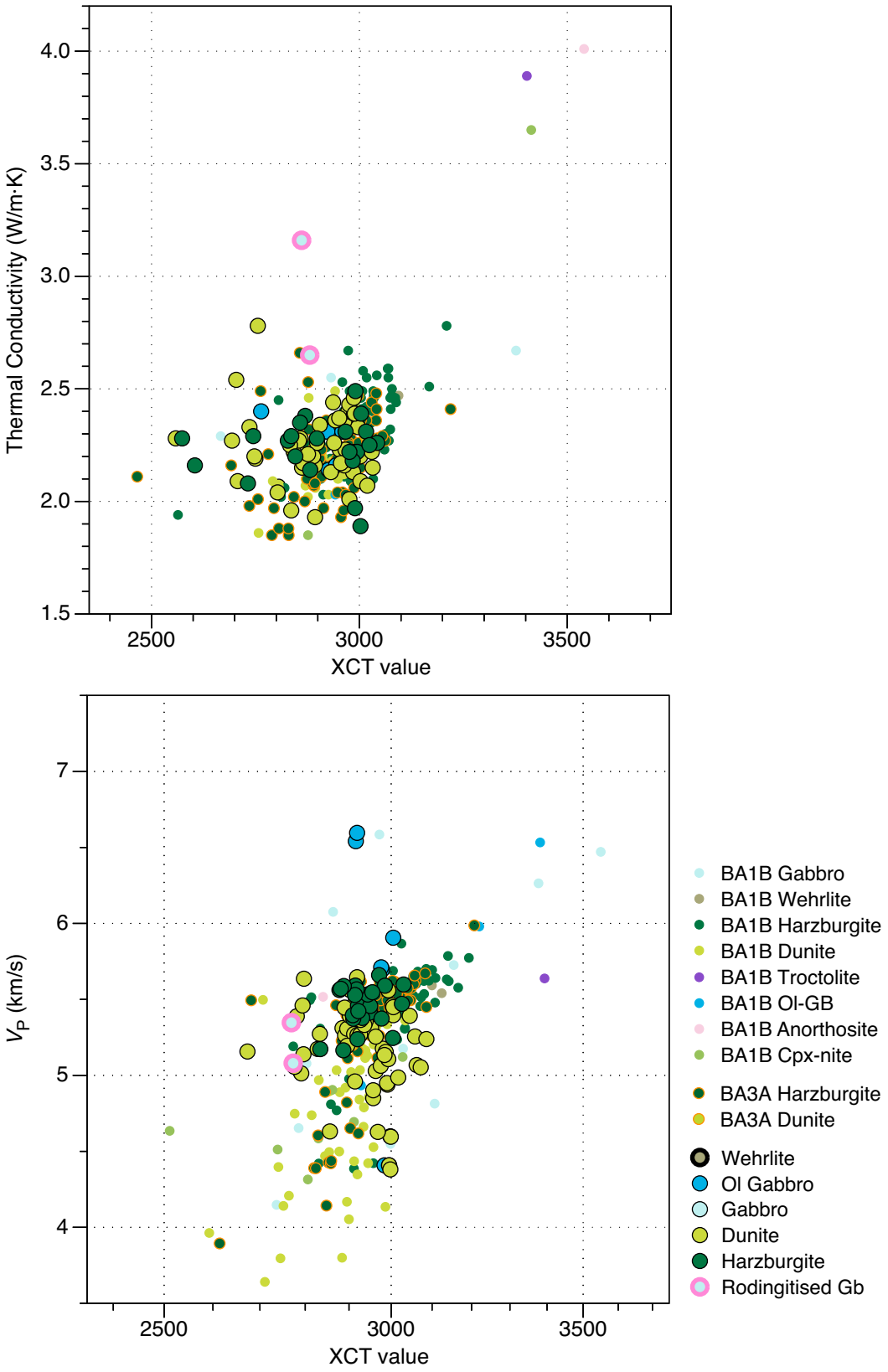

Tables

Table T1. Operations, Hole BA4A. **This table is available in Microsoft Excel format.**

Table T2. Igneous sequences, Hole BA4A. **This table is available in Microsoft Excel format.**

Table T3. Rock types, Hole BA4A. **This table is available in Microsoft Excel format.**

Table T4. XRD results, Hole BA4A. **This table is available in Microsoft Excel format.**

Table T5. Dikes, Hole BA4A. **This table is available in Microsoft Excel format.**

Table T6. Comparison of thickness of lithologies in Holes BA1B, BA3A, and BA4A. **This table is available in Microsoft Excel format.**

Table T7. Mineral abundances, Hole BA4A. **This table is available in Microsoft Excel format.**

Table T8. Comparison of LOI, Mg#, SiO_2, Al_2O_3, and CaO by lithology, Hole BA4A. **This table is available in Microsoft Excel format.**

Table T9. Whole rock major element, trace element and volatile compositions and mineralogy, Hole BA4A. **This table is available in Microsoft Excel format.**

Table T10. Whole rock trace element data from LA-ICP-MS, Hole BA4A. **This table is available in Microsoft Excel format.**

Table T11. Natural remanent magnetization and principal component analysis results, Hole BA4A. **This table is available in Microsoft Excel format.**

Table T12. Bulk magnetic susceptibility and anisotropy of magnetic susceptibility, Hole BA4A. **This table is available in Microsoft Excel format.**

Table T13. Physical properties by lithology, Hole BA4A. **This table is available in Microsoft Excel format.**

Table T14. WRMSL results, Hole BA4A. **This table is available in Microsoft Excel format.**

Table T15. Thermal conductivity, Hole BA4A. **This table is available in Microsoft Excel format.**

Supplemental Tables

Table ST1. Thin section descriptions, Hole BA4A. **This table is available in Microsoft Excel format.**

Table ST2. VCD summary, Hole BA4A. **This table is available in Microsoft Excel format.**

Table ST3. Vein log, Hole BA4A. **This table is available in Microsoft Excel format.**

Table ST4. Vein intensity, Hole BA4A. **This table is available in Microsoft Excel format.**

Table ST5. Vein occurrence/crosscutting relationships, Hole BA4A. **This table is available in Microsoft Excel format.**

Table ST6. MSCL-W data, Hole BA4A. **This table is available in Microsoft Excel format.**

Table ST7. MSCL-C data, Hole BA4A. **This table is available in Microsoft Excel format.**